

Numerical simulation of unsteady flow in hydraulic turbomachines

Citation for published version (APA):

Kleine, de, D. (2009). *Numerical simulation of unsteady flow in hydraulic turbomachines*. [Phd Thesis 1 (Research TU/e / Graduation TU/e), Mechanical Engineering]. Technische Universiteit Eindhoven.
<https://doi.org/10.6100/IR644236>

DOI:

[10.6100/IR644236](https://doi.org/10.6100/IR644236)

Document status and date:

Published: 01/01/2009

Document Version:

Publisher's PDF, also known as Version of Record (includes final page, issue and volume numbers)

Please check the document version of this publication:

- A submitted manuscript is the version of the article upon submission and before peer-review. There can be important differences between the submitted version and the official published version of record. People interested in the research are advised to contact the author for the final version of the publication, or visit the DOI to the publisher's website.
- The final author version and the galley proof are versions of the publication after peer review.
- The final published version features the final layout of the paper including the volume, issue and page numbers.

[Link to publication](#)

General rights

Copyright and moral rights for the publications made accessible in the public portal are retained by the authors and/or other copyright owners and it is a condition of accessing publications that users recognise and abide by the legal requirements associated with these rights.

- Users may download and print one copy of any publication from the public portal for the purpose of private study or research.
- You may not further distribute the material or use it for any profit-making activity or commercial gain
- You may freely distribute the URL identifying the publication in the public portal.

If the publication is distributed under the terms of Article 25fa of the Dutch Copyright Act, indicated by the "Taverne" license above, please follow below link for the End User Agreement:

www.tue.nl/taverne

Take down policy

If you believe that this document breaches copyright please contact us at:

openaccess@tue.nl

providing details and we will investigate your claim.

Numerical simulation of unsteady flow in hydraulic turbomachines

PROEFSCHRIFT

ter verkrijging van de graad van doctor aan de
Technische Universiteit Eindhoven, op gezag van de
rector magnificus, prof.dr.ir. C.J. van Duijn, voor een
commissie aangewezen door het College voor
Promoties in het openbaar te verdedigen
op woensdag 7 oktober 2009 om 16.00 uur

door

David de Kleine

geboren te Gaasterland

Dit proefschrift is goedgekeurd door de promotor:

prof.dr.ir. J.J.H. Brouwers

Copromotoren:

dr. B.P.M. van Esch

en

dr. J.G.M. Kuerten

Copyright © 2009 by D. de Kleine

All rights reserved. No part of this publication may be reproduced, stored in a retrieval system, or transmitted, in any form, or by any means, electronic, mechanical, photocopying, recording, or otherwise, without the prior permission of the author.

This research is supported by the Dutch Technology Foundation STW, applied science division of NWO and the Technology Program of the Ministry of Economic Affairs.

Cover: ir. D.F. Woudagemaal, by J. Draijer.

Cover design: Oranje Vormgevers Eindhoven (www.oranjevormgevers.nl).

Printed by the Eindhoven University Press.

A catalogue record is available from the Eindhoven University of Technology Library.

ISBN: 978-90-386-1946-0

Contents

Summary	7
1 Introduction	9
1.1 Centrifugal pumps	10
1.2 Numerical methods	12
1.3 Collocated grid	13
1.4 Staggered grid	15
1.5 Aim and outline	16
2 DeFT	19
2.1 Grid	20
2.2 RANS equations	22
2.2.1 Stationary frame of reference	22
2.2.2 Rotating frame of reference	24
2.3 Boundary conditions	25
2.4 Staggered discretization	26
2.5 Solution procedure	30
2.6 Multi block exchange of primitive variables	32
3 Verification	35
3.1 Unsteady channel flow	35
3.2 Accuracy on a rough grid	39
3.3 Turbulence model in the rotating frame	41
3.4 Coriolis and centrifugal forces	43
3.5 Sliding interface	45
4 Validation	49
4.1 Measurements	49
4.2 Numerical model	51
4.3 Results and comparison with measurements	54
4.3.1 Flow field	54
4.3.2 Blade surface pressure	55
4.3.3 Lift and drag forces	57
4.3.4 Axial and tangential forces	60

4.3.5	Pressure and shear stress forces	66
4.4	Summary	70
5	Unsteady flow in a pump	71
5.1	Centrifugal pump and measurements	71
5.2	Numerical model	73
5.3	Flow field	75
5.4	Comparison	83
5.5	Conclusions	87
6	Conclusions and discussion	89
6.1	Conclusions	89
6.1.1	DeFT	89
6.1.2	Verification	90
6.1.3	Validation	91
6.1.4	Unsteady flow in a pump	91
6.2	Discussion	91
	Bibliography	93
A	Blade surface coordinates	97
	Dankwoord	99
	Curriculum vitae	101

Summary

Numerical simulation of unsteady flow in hydraulic turbomachines

Turbines and pumps dealing with incompressible flow are examples of hydraulic turbomachines. In most cases the flow is highly turbulent and time-dependent, caused by the rotation of the impeller in a stationary casing. The geometry, with doubly curved surfaces, adds even more to the complexity. It all leads to a flow which is difficult to model. Yet, to optimize turbomachines it is necessary to analyze the flow in detail. Flow simulations using Computational Fluid Dynamics (CFD) can be a very helpful tool. The software solves the discretized partial differential equations for mass and momentum conservation on a grid that covers the flow domain. Two basic discretization schemes can be distinguished: collocated and staggered. When a collocated scheme is used, the solution suffers from odd-even decoupling. In practice this is suppressed with artificial measures which either decrease the accuracy of the simulation or increase the calculation time for an unsteady incompressible flow. Using a staggered scheme, accurate discretization is more difficult, but odd-even decoupling is avoided.

In this thesis a CFD code is developed which is based on a staggered, block-structured grid scheme. It is suited for the calculation of time-dependent fluid motion in turbomachines. The CFD code, named DEFT, is originally developed by the group of Wesseling at Delft University of Technology. The first extension in the current work was an interpolation procedure implemented to handle non-matching grids for more flexibility in grid generation. Furthermore, a sliding interface to connect the rotating grid in the impeller and the stationary grid was developed. Coriolis and centrifugal forces for calculations in the rotating frame of reference, were implemented in two ways: using a conservative formulation and using source terms. An adaptation of the pressure equation proved necessary to reduce calculation time for computations involving a sliding interface. Although the conceptual ideas behind these extensions are applicable in 3D, they have been implemented in 2D and verified with the simulation of a number of relatively simple flows.

DeFT was validated with the simulation of the flow through a cascade of blades which is a model of an axial-flow pump. The blade surface pressure and the total force on the blade are calculated. There is good agreement between values calculated with DeFT, Fluent, values from experiments, and other CFD calculations obtained

from literature.

The flow through a centrifugal pump with a vaned diffuser is simulated using the staggered discretization in DeFT and the collocated discretization in Fluent. The calculated time-averaged pressure and velocity along the pitch of a rotor channel show good correspondence. The agreement with results from experiments and other CFD calculations obtained from literature is more qualitative. The calculation time needed by DeFT and Fluent is approximately equal, despite the use of a large number of blocks in DeFT and its lack of a convergence enhancing multi-grid method which is used by Fluent.

Chapter 1

Introduction

A turbomachine is used to transfer energy from a rotor to a fluid or vice versa. In the special case of a hydraulic turbomachine the working fluid is incompressible. Many machines can be classified as hydraulic turbomachines. Examples are cooling fans in engines, turbines in hydraulic power plants and pumps for tap water supply. Other machines with a rotor working on an incompressible fluid are for example stirrers in the food processing industry, rotary flow meters in the oil industry and rotating particle collectors for filtering applications. The demands on the performance of these machines can be very high. For a large turbine, for example, a slight increase in efficiency yields much energy. Therefore it makes sense to improve its efficiency as much as possible. The flow in turbomachines plays a central role in its performance. The flow is very complex, because it is highly turbulent and the geometry is complicated and partly rotating. It has to be analyzed in detail in order to make design optimizations. Numerical flow simulation is often used to achieve this. Many models based on approximate physical laws can be used to simulate flows with a computer.

Most turbomachinery manufacturers use commercially available flow simulation software, like STAR-CD, CFX and FLUENT. In all cases the numerical models are based on so-called collocated-grid schemes, which are suited for compressible flows and steady incompressible flows. In the case of hydraulic turbomachines the flow is incompressible and unsteady. This means that the numerical models in commercially available software codes are in principle unsuited for this application. There are a few work-arounds for this problem which are incorporated into commercial codes. The drawback, however, is that such methods are less accurate and less convenient for unsteady incompressible flows.

The best method for calculating unsteady, incompressible flows is based on a so-called staggered-grid scheme. The aim of this research is to develop a code with such a scheme and to apply it to flows in centrifugal pumps. The performance of the code is compared with that of a commercial code.

The first section of this chapter is about the centrifugal pump. Section 2 treats the possible numerical methods for flow simulation. The next section explains the odd-even decoupling problem on a collocated grid. In section 4 the staggered grid is introduced. Finally, in section 5, the aim of this research and the outline of the rest of the thesis is given.

1.1 Centrifugal pumps

In Fig. 1.1 a schematic drawing of a centrifugal pump is shown. The fluid enters the

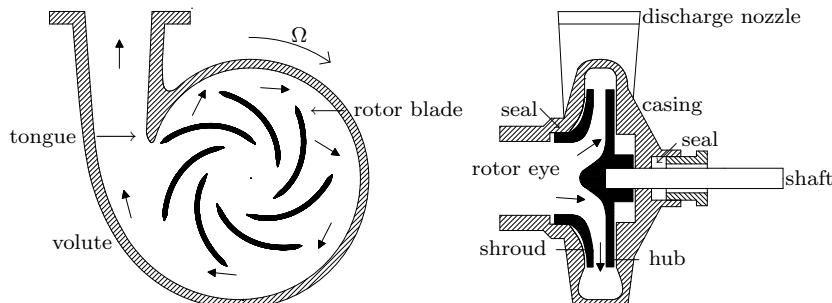


Figure 1.1. Schematic drawing of a centrifugal pump.

pump in axial direction into the eye of the rotor. It is subsequently accelerated into a circular motion by the rotor blades and guided through the volute to the discharge nozzle where the fluid leaves the pump. The inlet of the pump and the volute are part of the pump casing. The rotor is mounted on the shaft which is driven at angular velocity Ω by an engine. Seals are fitted on the rotor and casing to restrict fluid under high pressure from leaking back to the rotor inlet or out of the pump casing. The rotor blades are always curved backwards, see Fig. 1.1. They may be of single or double curvature. The blades are fitted to the hub of the rotor. The rotor may be equipped with a shroud, or constructed as an open impeller. Starting from the tongue of the volute, the through-flow area gradually increases towards the discharge nozzle to account for the increasing amount of fluid. The ideal shape of the volute depends on the flow rate at which the pump operates.

A pump increases the total pressure of a fluid by transferring mechanical power from the rotating shaft to the fluid. The velocity of the shaft is applied to the fluid through the rotor blades. This ensures the increase of angular momentum of the fluid in two ways: the angular velocity of the fluid is increased and the fluid is transported to a larger radius. Both of these principles lead to an increase in total pressure. The kinetic energy of the fluid is partly converted into static pressure. This occurs mainly in the discharge nozzle, but also in the volute. The added total pressure is used to overcome flow resistance, for example friction in pipes for tap water supply or the gravitational force in case of a polder pumping station.

Important quantities concerning the process of energy transfer in a pump are the flow rate Q , the increase of total pressure Δp_t and the shaft power P_{sh} . Using these, the hydraulic efficiency of the pump η_h is defined as

$$\eta_h = \frac{Q \Delta p_t}{P_{sh}}. \quad (1.1)$$

The added total pressure of the pump is

$$\Delta p_t = (p_2 + \frac{1}{2} \rho v_2^2 + \rho g z_2) - (p_1 + \frac{1}{2} \rho v_1^2 + \rho g z_1), \quad (1.2)$$

where ρ is the fluid density, g is the gravitational acceleration, p the static pressure, v the velocity and z the height. The subscripts denote positions 1 and 2, at the entrance and discharge of the pump respectively. The efficiency is a measure for the losses that occur during the energy transfer. Losses are due to mechanical friction in the bearings and seals of the pump or due to dissipation in the fluid. These viscous losses can be split in disc friction, leakage flow losses and hydraulic losses. Disc friction results from the shear forces between the external surface of the rotor and the ambient fluid. These losses depend on shaft speed, but hardly on flow rate. The leakage flow is the reverse flow through the seals between the rotor and the casing. All other viscous losses in the pump are gathered in hydraulic losses. The head H is often used to express the increase in total pressure by the pump

$$H = \frac{\Delta p_t}{g\rho}. \quad (1.3)$$

The performance of a pump is presented in the form of characteristic curves. These curves give the dependence of head, efficiency and shaft power on flow rate for a specific pump, shaft speed and fluid properties. An example of these curves is shown in Fig. 1.2. The flow rate for which the efficiency attains its maximum value is called

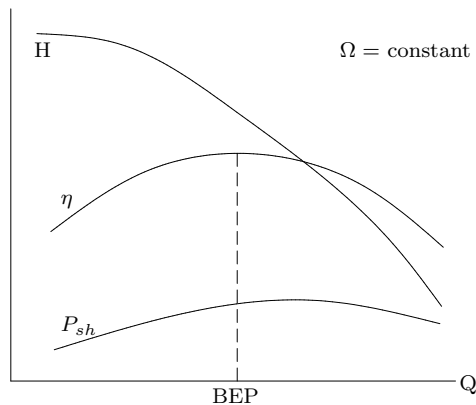


Figure 1.2. Schematic drawing of the characteristic curves of a centrifugal pump. Head, efficiency and shaft power as functions of flow rate, for constant shaft speed.

the Best Efficiency Point (BEP). The influence of the fluid properties, shaft speed and the geometry of a pump on the characteristic curves is very complicated. The flow inside the pump plays a central role in this relation.

Although pumps are already used and improved for a long time, there is still a desire to further optimize their design. The efficiency of a pump operating in its BEP can be quite high, but improving it even further can save much energy. Sometimes pumps need to operate for a range of flow rates instead of at one flow rate. Here it is important to design a pump with a good efficiency for this range of conditions instead of an excellent efficiency for only one flow rate.

Another important condition for a good design is avoiding cavitation. When the pressure in a pump is lower than the vapor pressure, vapor bubbles arise. These

bubbles collapse again when they migrate to positions where the pressure is above the vapor pressure. If this happens close to the pump blades or casing, severe erosion can occur. This process, called cavitation, also decreases the efficiency of the pump.

The design of new pumps is based on a combination of empirical knowledge of comparable pumps, experimental results and Computational Fluid Dynamics (CFD) simulations. Empirical knowledge of other pumps can only be used when the new design is close to an old design. The advantage of this method is that it is inexpensive and fast to use. Experimental results are generally very expensive and time consuming and sometimes very difficult to obtain, but they can be very accurate. CFD results are also expensive and time consuming to obtain, but far less than experimental results, while the accuracy can be very good. Besides that, it is relatively easy to change the design and calculate the results. However, the most important advantage of CFD results is the fact that they are very detailed. The flow quantities like pressure and velocity are known in the whole calculation domain and for all times calculated. This is necessary to understand the complex flow in pumps and to be able to improve their design. The role of CFD in the design process is increasing over time. The development of computationally inexpensive and accurate numerical methods and the continuous growth of computer resources in terms of speed and storage take account for this.

1.2 Numerical methods

The flow in pumps can be considered incompressible as long as the velocity of the fluid is small compared to the speed of sound in the fluid. The equations that govern incompressible, adiabatic fluid motion are partial differential equations that describe the conservation of mass (continuity) and momentum (Navier-Stokes). These equations are discretized on the grid that represents the geometry of the flow-domain inside the pump. This results in a large number of coupled algebraic equations. Subsequently, the boundary conditions are applied to the equations. For example, the flow rate through the pump is imposed by prescribing the velocity at the inlet of the domain. The motion of the rotor is prescribed by a constant angular velocity at the rotor blades. Solving the matrix equations yields the pressure and velocity in the domain for all time steps. From this, the delivered head of the pump and the torque on the rotor can be calculated. The pressure distribution also reveals where cavitation inception occurs.

Solving the governing equations yields the main problem in CFD, which is that very small scales influence larger scales. The importance of this effect is reflected by the Reynolds number

$$Re = \frac{\rho LU}{\mu}, \quad (1.4)$$

where L is a characteristic length of the flow domain, U is a characteristic velocity of the flow and μ is the fluid dynamic viscosity. For larger Re , smaller scales appear in the flow. When a Direct Numerical Simulation (DNS) is performed, all scales are solved. This results in a very fine grid and consequently a large number of coupled equations. Up to this moment DNS is only possible for flows in simple geometries

at Re -numbers typically below 10^4 . For many pumps the flow is characterized by $Re > 10^5$. Computers are by far not powerful enough to solve such flows using DNS. That is why several modified flow equations are applied instead. These take less time and memory to solve, but are less accurate as well.

Using the Reynolds Averaged Navier-Stokes (RANS) equations it is feasible to calculate the flow through a pump. Here the influence of the turbulent fluctuations on the main flow is modeled by a turbulence model. Such a model is based on approximations. In the Euler equations, the Navier-Stokes equations are approximated by omitting the viscous terms, which can be small in the main flow, but are not small in boundary layers. Flows in pumps are also solved using potential flow theory, which assumes an inviscid and irrotational flow field. Combinations of these methods are possible as well. Sometimes the viscous forces are only solved in the boundary layers, while in the rest of the domain only the inviscid equations are solved. General introductions in computational methods for fluid dynamics can be found in [23], [13], and [19].

One of the other choices that have to be made, is between a transient, a stationary or one of the quasi-stationary simulation options available in CFD software. A stationary simulation can be sufficiently accurate when the acceleration term is small. In pumps this is the case when operating close to the design point (BEP). However, further away from the BEP, time-dependent effects due to rotor-stator interaction, rotor-tongue interaction, stall and cavitation increase. Non-uniform inflow conditions will also result in a time-dependent flow. Under these conditions a transient simulation is necessary in order to accurately model the flow.

There are also several options for discretization schemes, turbulence models and matrix solvers. All of these choices influence the accuracy of the solution, the calculation time and the robustness of the calculation process. Because in CFD many approximations are used, each having its own advantages in certain cases, research into these methods is still ongoing. One of the fundamental issues concerning discretization schemes is the manner in which variables are stored in discrete nodal points; collocated or staggered. In the remainder of this chapter both methods are described.

1.3 Collocated grid

In most finite volume based CFD software, the discretization of the partial differential equations is on a collocated grid, where the dependent variables are all positioned in the same nodes, e.g. in the cell centers (Fig. 1.3). When the gradient of, for example, the pressure is discretized, the pressure is interpolated from the cell centers to the edge of the control volume. If a central discretization scheme is used on a uniform grid, the gradient is written as

$$\left. \frac{\partial p}{\partial x} \right|_i = \left(\frac{p_{i+1} + p_i}{2} - \frac{p_i + p_{i-1}}{2} \right) \frac{1}{\Delta x} = \frac{p_{i+1} - p_{i-1}}{2\Delta x}, \quad (1.5)$$

where the subscript i refers to the cell number in the x -direction and Δx is the size of the cell in the x -direction. As a result, the value of the pressure in the point where it

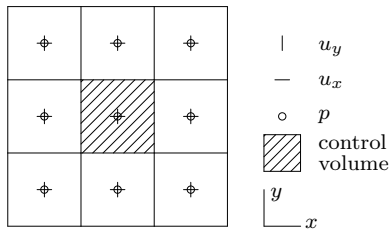


Figure 1.3. Collocated grid, with cartesian velocity in x -direction u_x , cartesian velocity in y -direction u_y and pressure p .

is discretized drops out. Therefore, the gradient in odd-numbered nodes only uses information from even-numbered nodes, and vice versa. This odd-even decoupling does not have to be a problem if it is suppressed by other terms of the partial differential equations that do have an odd-even coupling. However, when these are weak or not present at all, an unphysical checkerboard pattern of the variable appears. This is shown in Fig. 1.4 for a one-dimensional pressure field. In reality often nearly uniform

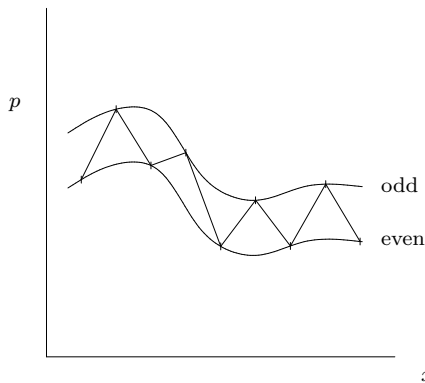


Figure 1.4. Odd-even decoupling resulting in a checkerboard pattern for the pressure.

grids are used for a smooth transition between areas with a high and a low cell density. On such a grid p_i is not canceled in Eq. (1.5), but the odd-even coupling remains weak. The most severe case of odd-even decoupling arises for the pressure in the incompressible Navier-Stokes equations, since the pressure is only present in gradient form. The velocity in the continuity equation is decoupled as well, but coupled (in some cases, weakly, [31]) via the momentum equations. To calculate incompressible flow on a collocated grid, measures have to be taken in order to prevent odd-even decoupling. This is done either through one-sided discretization, flux splitting, Pressure Weighted Interpolation (PWI), or the artificial compressibility method. These methods are summarized in [31] and outlined here.

One-sided instead of central discretization can be used to avoid odd-even decoupling. A forward discretization for the velocity derivative and a backward discretization for the pressure gradient (or vice versa) are used to establish the necessary coupling between odd and even positions. This was applied in [15] and a proof of

convergence was given in [11]. This method is however first-order accurate and dissipative.

Flux splitting applied to the Navier-Stokes equations in [8], [9] and [10] is based on a more sophisticated combination of one-sided forward and backward discretizations. This method also prevents odd-even decoupling, but is dissipative as well.

The Pressure Weighted Interpolation (PWI) method was introduced in [24]. Currently this method is also called the momentum interpolation method. The core of the solution to suppress odd-even decoupling is the addition of a small pressure term to the continuity equation. The term is smaller than the discretization error of the original mass conservation equation and consists of pressures from odd and even positions thus establishing the coupling. In the originally proposed PWI method, the calculation results depend on certain relaxation factors, but a version without this drawback was proposed in [21]. When strong body forces are present, the PWI method has to be adapted to work properly, see [16]. For flows with a high swirl number or a curved domain, the PWI method can be adapted as well.

The artificial compressibility method is in principle only suited to obtain steady solutions. Using an artificial equation of state, the time derivative of the pressure is added to the continuity equation ([5]). The pressure in the even points is now coupled to the velocity in the odd points. Because the odd and even velocities are coupled through the momentum equations, the odd and even pressures are coupled as well. The solution proceeds in time until it becomes steady, driving the added artificial compressibility term to zero. For accurate unsteady simulations the procedure has to be changed. Pseudo time is introduced and for every physical time step the added artificial term is driven to zero by iterating in pseudo time. This is sometimes called dual time stepping. The artificial compressibility method and the PWI method are compared in [25]. It turned out that the PWI method needs less computer memory and results in better accuracy and mass conservation.

The adaptations needed to suppress decoupling are believed to result in calculations which are either less accurate or more time-consuming, especially for time-dependent flows. An alternative method based on a staggered-grid approach does not suffer from odd-even decoupling. It is introduced in the next section.

1.4 Staggered grid

Instead of a collocated grid, it is possible to use a staggered grid where different variables are positioned at different locations in a cell, see Fig. 1.5. The velocities are positioned at the centers of the faces of a cell and the pressure and other scalars like turbulence quantities are positioned in the cell centers. The control volumes for the continuity and momentum equations with the discretization stencils are given in Fig. 1.6. The main advantage of the discretization on the staggered grid is that first spatial derivatives of the velocity in the continuity equation and the pressure are calculated using information from adjacent nodes (in case of a second-order central scheme), thus preventing odd-even decoupling [22]. For these derivatives, the variable is conveniently positioned on the edge of the control volume. Interpolation, which can cause cancelation of the central variable, is not necessary. Due to this advantage a

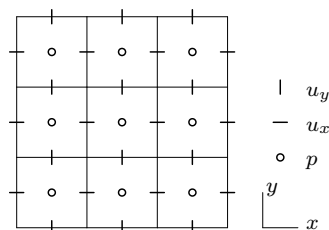


Figure 1.5. Staggered grid, with cartesian velocity in x-direction u_x , cartesian velocity in y-direction u_y and pressure p .

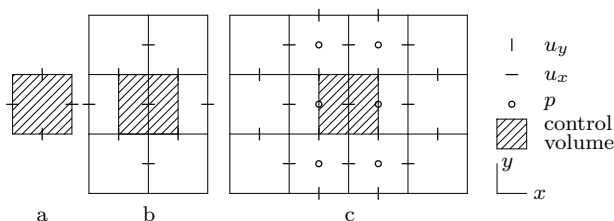


Figure 1.6. Control volume and discretization stencil for (a) the continuity equation, (b) the convection and (c) combined pressure and viscous terms of the momentum equation respectively.

staggered grid is in principle favorable for computing incompressible flow. No artificial terms are needed in the solution procedure.

1.5 Aim and outline

In general, collocated grids are preferred to staggered grids, because they are easier for discretization of the equations, especially if the grid is non-uniform. However, for incompressible flow on a uniform grid, staggered discretization is favorable [33]. On a non-uniform grid, like in a pump, staggered discretization, as originally introduced by Harlow and Welch [17] is very inaccurate. Wesseling [33], however, proposed a staggered discretization that proved to be accurate on non-smooth grids, which makes it useful for a much wider range of applications. Using this discretization, the RANS equations were implemented in the block structured CFD package DeFT [1], developed at Delft University of Technology.

The aim of this thesis is to continue the development of DeFT in order to make it applicable to pumps. Because DeFT uses a boundary-fitted grid and the rotor moves with respect to the casing, a sliding interface between the rotating and stationary grid is implemented. In the rotating frame of reference the Coriolis and centrifugal forces appear in the Navier-Stokes equations. These body forces are implemented in conservative form. Finally, to be more flexible in grid generation in the complex geometry of the pump, DeFT is adapted to handle non-matching grids. After this, the performance of DeFT is compared with that of the commercial package Fluent for the simulation of the flow in a centrifugal pump. The performance of the solvers is based on the accuracy of the calculation results and the time and memory needed for the calculation of the flow. The time-dependent velocity and pressure fields are compared

with the results from experiments and CFD calculations available in literature.

Although this thesis focuses on the calculation of the flow in a centrifugal pump it is just as well applicable to other machines like turbines, fans or stirring devices, as long as the flow in the apparatus can be modeled as incompressible.

The next chapter treats the most important features of DeFT. In chapter 3, relatively simple flows are simulated to verify the correct implementation of DeFT. The accuracy of staggered and collocated discretizations is compared for a flow on a very non-uniform grid. A time-dependent channel flow is simulated to compare the performance of DeFT and Fluent. Chapter 4 concerns the validation of DeFT, simulating a stationary flow through a cascade of blades. The results of DeFT and Fluent are compared with the results of experiments and CFD simulations from literature. Simulations of the time-dependent flow through a centrifugal pump are described in chapter 5. Finally, the conclusions and recommendations of this thesis are given in chapter 6.

Chapter 2

DeFT

DeFT was developed in the group of Prof. Wesseling at Delft University of Technology. The main focus was on solving the incompressible RANS equations. It was part of the project for the development of the Information System for flow simulation based on the Navier-Stokes equations (ISNaS). In [3] the domain decomposition procedure for the laminar equations is described. The extension to turbulent flows is treated in [35], where different $k - \epsilon$ and the $k - \omega$ turbulence models are used. Several discretization methods are implemented. Simulations can be done on a collocated grid or a staggered grid. For staggered grids one can choose the classical discretization or the WesBeek discretization developed by Wesseling and Van Beek [28]. The classical discretization is accurate on smooth grids only, while the WesBeek discretization is accurate on non-smooth grids as well. However, the WesBeek discretization stencil is larger. DeFT was also used to test a number of iterative solvers for large sparse linear asymmetric matrix equations: the standard Conjugate Gradient Squared (CGS) method, the Generalized Minimal RESidual (GMRES) method, the GMRES Recursive (GMRESR) method, the Generalized Conjugate Residual (CGR) method and the Conjugate Gradient STABilized (CG-STAB) method. These solvers are suitable for DeFT because the grid is block-structured. GMRESR is robust and efficient in terms of memory and CPU time. Therefore, it is used for the calculations in this thesis. In [14] the efficiency of several parallel solution strategies is compared.

The goal of this chapter is to explain how DeFT performs a flow simulation. In this thesis DeFT is used to solve the two-dimensional, time-dependent RANS equations for an incompressible, Newtonian fluid on a non-uniform, boundary-fitted grid. Turbulence is modeled with the standard $k - \epsilon$ model. All calculations are done on a single processor. Cavitation is not modeled. In the first section, the grid and some restrictions concerning block coupling are treated. Subsequently, the governing equations are given in both the stationary and rotating frame of reference. The conservative formulation of the Coriolis and centrifugal forces is treated as well. The following sections are about the boundary conditions and the staggered discretization. In the section on the solution procedure, the main steps in the structure of the solver are explained. Finally the multi-block exchange of the primitive variables is clarified, where the focus is on the implementation of the non-matching blocks and the sliding interface.

2.1 Grid

In DeFT, the grid in the flow-domain is boundary-fitted and block structured. The cells have four edges which are straight lines. Each block can be regarded topologically as a rectangle with directions 1 and 2 along the block faces, see Fig. 2.1. Around each

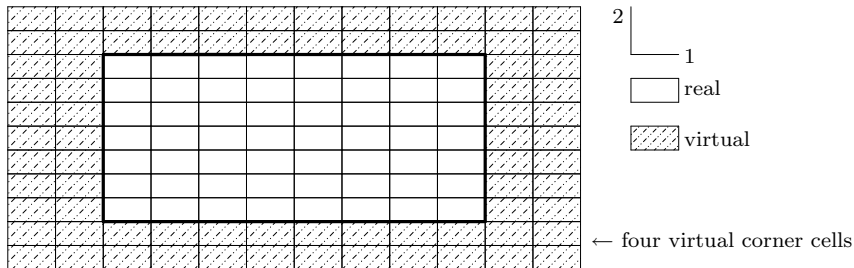


Figure 2.1. A block with real and virtual cells.

block two rows of virtual cells are used. In each corner of a block, there are four virtual corners cells. When there is no neighboring block, the virtual cells are extrapolations from the inner grid cells to the outside of the domain. The advantage of using virtual cells is that the discretization stencil which is used in the inner part of the block, can also be used close to the block face, where part of the stencil is located in the virtual cells. The virtual cells are used to prescribe boundary conditions if the corresponding block face is at the edge of the flow domain.

When a face of a block is connected to another block, its virtual cells overlap the real cells of the neighboring block. They are used to transfer information between the blocks. When the grid at the interface between two blocks matches, the virtual cells are copies of the real cells in the first two rows of the neighboring block. In this way, flow variables can be copied from the real cells to the virtual cells without interpolation. This, however, restricts the way in which blocks can be coupled, see Fig. 2.2. The C-type grid of block 3 connects to blocks 1 and 2 with only one face.

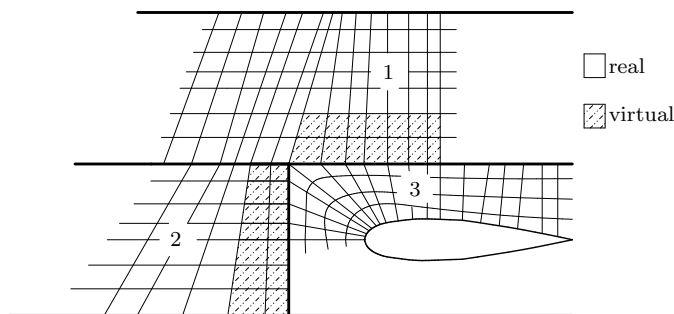


Figure 2.2. A block connection that splits the virtual cells.

The virtual cells along this face are cross hatched in blocks 1 and 2. These two virtual

rows of cells are, however, discontinuous at the point where blocks 1, 2 and 3 meet. This is not allowed, since the discretization scheme assumes neighboring cells in the stencil to be adjacent in the grid. A solution to this problem is to divide blocks 1 and 3 into two blocks at the discontinuity, see Fig. 2.3. Another restrictive consequence of

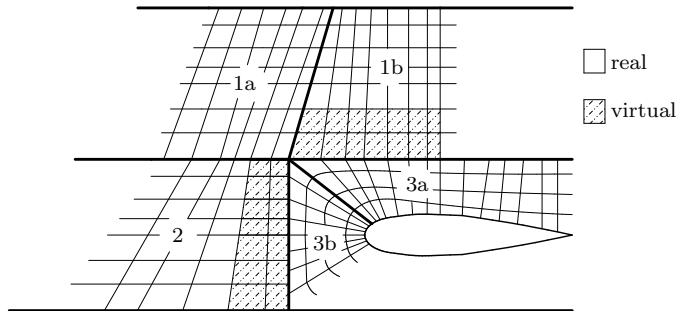


Figure 2.3. More blocks to avoid discontinuous virtual rows.

the use of copies of cells for the virtual grid emerges when three blocks meet at one point in the interior of the flow domain, see Fig. 2.4. The virtual cells of block 2 are

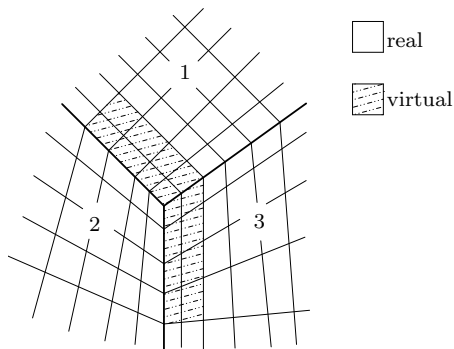


Figure 2.4. Where three blocks meet in an internal point, there is no space for the four corner cells.

located in blocks 1 and 3. At the interface between blocks 1 and 3, these rows meet, leaving no space for the four corner cells. This block coupling is therefore not allowed (unless a special discretization is adopted).

When the grids of two neighboring blocks do not match, the coordinates of the virtual cells are chosen such that interpolation of the flow variables is only necessary in the direction parallel to the block face, see Fig. 2.5. The shape of the virtual cells resembles the shape of the overlapping real cells as much as possible. In the direction normal to the mutual block face, the size of the cells is equal. In the parallel direction, the length of the virtual cell is determined by linear interpolation between the real cells. The lower face of block 1 is divided into two subfaces that are connected to blocks 2 and 3. Subfaces always contain a whole number of cells. Referring to Fig.

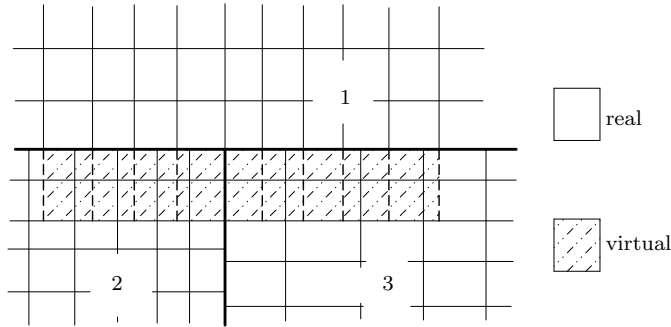


Figure 2.5. Virtual cells along a non-matching block interface.

2.5, all the block interfaces are non-matching, except for the two rows of blocks 2 and 3 that overlap with the virtual cells of block 1. These rows are not allowed to be non-matching, because it would make the virtual rows of block 1 discontinuous.

2.2 RANS equations

2.2.1 Stationary frame of reference

The equation for conservation of mass for an incompressible flow is, in index notation,

$$\frac{\partial u_i}{\partial x_i} = 0, \quad (2.1)$$

where u_i and x_i are the cartesian velocity component and coordinate in direction i respectively. When an index appears more than once in a term, summation over all values of the index is applied. The conservation of momentum of an incompressible Newtonian fluid equals

$$\frac{\partial u_i}{\partial t} + \frac{\partial}{\partial x_j} \left[u_i u_j + \delta_{ij} \frac{p}{\rho} - \frac{\mu}{\rho} \frac{\partial u_i}{\partial x_j} \right] = 0, \quad (2.2)$$

where t is the time, p the pressure, ρ the density and μ the dynamic viscosity of the fluid. For the turbulent flows that are treated in this thesis, the smallest scales of the flow are too small to solve. Therefore, the governing equations are time-averaged over a period T , which is long compared to the time-scale of the turbulent fluctuations, but short compared to the time scale of the global time-dependent behavior of the flow. The Reynolds Averaged Navier-Stokes (RANS) equations are derived by splitting each velocity component in a time-averaged part, \bar{u}_i , and a fluctuating part, u'_i and likewise for the pressure

$$u_i = \bar{u}_i + u'_i, \quad p = \bar{p} + p'. \quad (2.3)$$

This is substituted in the continuity and Navier-Stokes equations and averaged over time. In all linear terms in velocity and pressure, the velocity and pressure is replaced

by its average value, because the average of the fluctuating part is zero. The non-linear terms, however, also produce products of fluctuating terms, which are not zero when averaged over time. This yields extra terms in the averaged momentum equation

$$\frac{\partial \bar{u}_i}{\partial t} + \frac{\partial}{\partial x_j} \left[\bar{u}_i \bar{u}_j + \overline{u_i' u_j'} + \delta_{ij} \frac{\bar{p}}{\rho} - \frac{\mu}{\rho} \frac{\partial \bar{u}_i}{\partial x_j} \right] = 0. \quad (2.4)$$

They are modeled as Reynolds stresses τ_{ij} , by equating

$$\tau_{ij} = -\rho \overline{u_i' u_j'} = \mu_t \frac{\partial \bar{u}_i}{\partial x_j}, \quad (2.5)$$

where μ_t is the turbulent viscosity, which depends on the flow and not on the fluid. Combining the turbulent and fluid viscosity in the effective viscosity $\mu_{eff} = \mu_t + \mu$, the RANS equations can be written as

$$\frac{\partial u_i}{\partial t} + \frac{\partial}{\partial x_j} \left[u_i u_j + \delta_{ij} \frac{p}{\rho} - \frac{\mu_{eff}}{\rho} \frac{\partial u_i}{\partial x_j} \right] = 0, \quad (2.6)$$

where for convenience u and p now denote time-averaged quantities. These equations are equal to the original Navier-Stokes equations again, except for the added turbulent viscosity. This new unknown has to be calculated with new equations that relate the turbulent velocity fluctuations to the average velocity and pressure. This so-called turbulence modeling is based on approximations. In the standard $k - \epsilon$ turbulence model, two extra partial differential equations are solved to calculate μ_t : one for the turbulent kinetic energy per unit mass,

$$k = \frac{1}{2} \overline{u_i' u_i'}, \quad (2.7)$$

and one for the dissipation rate of turbulent kinetic energy per unit mass,

$$\epsilon = \frac{\mu}{\rho} \overline{\frac{\partial u_i'}{\partial x_j} \frac{\partial u_i'}{\partial x_j}}. \quad (2.8)$$

The turbulent viscosity is calculated from k and ϵ using

$$\mu_t = \rho C_\mu \frac{k^2}{\epsilon}, \quad (2.9)$$

where C_μ is a closure coefficient. A closure coefficient is a constant that represents products of fluctuations that can not be expressed in the variables that are calculated: u_i , p , k or ϵ . These terms are therefore not calculated, but approximated by a constant. The exact partial differential equation for k is derived from the following moment of the Navier-Stokes equations

$$\overline{u_i' N(u_i)} = 0, \quad (2.10)$$

where $N(u_i)$ is the Navier-Stokes operator

$$N(u_i) = \frac{\partial u_i}{\partial t} + \frac{\partial}{\partial x_j} \left[u_i u_j + \delta_{ij} \frac{p}{\rho} - \frac{\mu}{\rho} \frac{\partial u_i}{\partial x_j} \right] = 0. \quad (2.11)$$

The modeled equation for k is

$$\rho \frac{\partial k}{\partial t} + \rho u_j \frac{\partial k}{\partial x_j} = \tau_{ij} \frac{\partial u_i}{\partial x_j} - \rho \epsilon + \frac{\partial}{\partial x_j} \left[\left(\mu + \frac{\mu_t}{\sigma_k} \right) \frac{\partial k}{\partial x_j} \right], \quad (2.12)$$

where σ_k is a closure coefficient. The exact equation for ϵ is derived from the moment

$$2 \frac{\mu}{\rho} \frac{\partial u_i}{\partial x_j} \frac{\partial N(u_i)}{\partial x_j} = 0. \quad (2.13)$$

The modeled equation for ϵ is

$$\rho \frac{\partial \epsilon}{\partial t} + \rho u_j \frac{\partial \epsilon}{\partial x_j} = C_{\epsilon 1} \frac{\epsilon}{k} \tau_{ij} \frac{\partial u_i}{\partial x_j} - C_{\epsilon 2} \rho \frac{\epsilon^2}{k} + \frac{\partial}{\partial x_j} \left[\left(\mu + \frac{\mu_t}{\sigma_\epsilon} \right) \frac{\partial \epsilon}{\partial x_j} \right], \quad (2.14)$$

where $C_{\epsilon 1}$, $C_{\epsilon 2}$ and σ_ϵ are closure coefficients. For the standard $k - \epsilon$ turbulence model, the closure coefficients are

$$C_\mu = 0.09, \quad C_{\epsilon 1} = 1.44, \quad C_{\epsilon 2} = 1.92, \quad \sigma_k = 1.0, \quad \sigma_\epsilon = 1.3. \quad (2.15)$$

These turbulence equations and more information on turbulence modeling in CFD can be found in [34].

The turbulence quantities ϵ and k should, for physical reasons, always be positive. In case they become negative during the solution procedure, their values are clipped to zero. This proved necessary to ensure stability during the initial part of the simulation of the centrifugal pump in chapter 5.

2.2.2 Rotating frame of reference

Part of the domain in a pump rotates with constant angular velocity Ω of the rotor. Because the grid is boundary-fitted, the governing equations need to be solved in the rotating frame of reference. The continuity equation does not change when it is transformed from the stationary to the rotating frame of reference. However, when the momentum equations are transformed to the rotating frame, apparent forces emerge, called the Coriolis \mathbf{F}_{cor} and centrifugal \mathbf{F}_{cen} forces

$$\mathbf{F}_{cor} = (-2w_2\Omega, 2w_1\Omega), \quad \mathbf{F}_{cen} = (-x_1\Omega^2, -x_2\Omega^2), \quad (2.16)$$

where w is the fluid velocity in the rotating frame, which can be written as $w = u - s$, with $s = (-\Omega x_2, \Omega x_1)$, the rotor velocity. These body forces can be written as source terms in the right hand side of the equations. However, contrary to Eq. (2.2), this formulation is not conservative. A conservative formulation is preferred because then momentum fluxes exactly cancel at the interface between two neighboring control volumes. Fortunately, Beddhu [2] showed that these forces can be written in conservative form as well

$$\begin{aligned} F_{cor,i} + F_{cen,i} &= (s_j + 2w_j) \frac{\partial s_i}{\partial x_j} \\ &= \frac{\partial}{\partial x_j} [2s_i w_j + s_i s_j] - 2s_i \frac{\partial w_j}{\partial x_j} \\ &= \frac{\partial}{\partial x_j} [2s_i w_j + s_i s_j], \end{aligned} \quad (2.17)$$

where use is made of the flow being incompressible. The Navier-Stokes equations in the rotating frame can be written as

$$\frac{\partial w_i}{\partial t} + \frac{\partial}{\partial x_j} \left[w_i w_j + 2s_i w_j + s_i s_j + \delta_{ij} \frac{p}{\rho} - \frac{\mu}{\rho} \frac{\partial w_i}{\partial x_j} \right] = 0. \quad (2.18)$$

The requirement of incompressible flow, however, can give some problems. When the continuity equation is not solved very accurately, the term with the divergence of the fluid velocity in Eq. (2.17) can be relatively large if $2s_i$ is large. The same holds for the first term within the square brackets of Eq. (2.18) if w_i is large

$$\frac{\partial(w_i w_j)}{\partial x_j} = w_j \frac{\partial w_i}{\partial x_j} + w_i \frac{\partial w_j}{\partial x_j}. \quad (2.19)$$

When non-matching grids are used, interpolation of the flow variables at the non-matching interface is necessary. Interpolation errors can lead to reduced accuracy for the solution of the continuity equation, causing the conservative formulation to fail. An example illustrating the use of the conservative and the source term formulation for matching and non-matching grids is given in section 3.4.

The $k - \epsilon$ turbulence equations in the rotating frame can be derived by adding the components of the Coriolis and centrifugal force Eq. (2.16) to the Navier-Stokes operator Eq. (2.11) and using the moments Eq. (2.10) and Eq. (2.8) to calculate their contribution. Because the centrifugal force does not depend on the fluid velocity or pressure, its contribution does not contain products of fluctuations and is therefore equal to zero. The Coriolis force depends on the velocity. However, the resulting products of velocity fluctuations cancel in both the equation for k and for ϵ . This is why the original equations can be used in the rotating frame of reference without adaptations.

2.3 Boundary conditions

Several boundary conditions can be applied to the RANS equations in DeFT. The no-slip condition is applied at walls where the velocity is zero. At the inflow boundary of the domain, a velocity profile is prescribed. At the outflow, the normal and tangential stress components

$$\sigma_{nn} = -p + 2\mu \frac{\partial u_n}{\partial x_n}, \quad \sigma_{nt} = \mu \left[\frac{\partial u_n}{\partial x_t} + \frac{\partial u_t}{\partial x_n} \right] \quad (2.20)$$

are given the value zero. The subscripts n and t refer to the direction normal and tangential to the domain boundary respectively. Another boundary condition for the Navier-Stokes equations is free-slip. In this case, the normal velocity and the tangential stress are set to zero. In case of turbulent flow, wall functions can be used to model the boundary layer. The normal velocity is set to zero, but instead of the tangential velocity, the wall shear stress τ_w is prescribed. The appropriate value is determined by

$$\tau_w = \frac{\rho C_\mu^{1/4} \sqrt{k_p} u_p}{u^*}, \quad (2.21)$$

where p refers to the point located at the center of a computational cell along the surface, u_p and k_p are the velocity and the kinetic turbulence energy in point p respectively and u^* is a non-dimensional velocity. This velocity is a function of the dimensionless wall distance

$$y^* = \frac{\rho C_\mu^{1/4} \sqrt{k_p} y_p}{\mu}, \quad (2.22)$$

where y_p is the normal distance from point p to the blade. The relation between u^* and y^* is linear

$$u^* = y^* \quad (2.23)$$

close to the blade when $y^* < 11.225$ and logarithmic

$$u^* = \frac{1}{\kappa} \ln E y^*, \quad (2.24)$$

where $\kappa = 0.41$ and $E = 9.8$, when $y^* > 11.225$.

For the turbulence equations, k and ϵ are prescribed at the inflow boundary of the domain. At the outflow, the normal gradient of k and ϵ are equal to zero. When wall functions are used, the wall normal gradient of k is set to zero. The value for ϵ in the first grid point next to the wall is calculated from

$$\epsilon = \frac{C_\mu^{3/4} k^{3/2}}{\kappa y}, \quad (2.25)$$

where $C_\mu = 0.09$ and the Von Karman constant $\kappa = 0.41$.

For all the equations periodic boundary conditions can be used.

2.4 Staggered discretization

The finite volume staggered WesBeek discretization used in DeFT is similar to the original Marker And Cell (MAC) discretization introduced by Harlow and Welch [17] when used on a uniform grid. The MAC discretization is, however, not accurate on non-uniform grids. Therefore, it is not useful for the complex geometry in turbomachines. The WesBeek discretization given in [33] for the incompressible Navier-Stokes equations, is accurate on non-smooth grids as well. The control volumes for the continuity and momentum equations and their discretization stencils are given in Fig. 2.6. The velocity is represented by the volume flux across a cell edge, which is the integral over the cell edge of the velocity component normal to the cell edge. $V^{(1)}$ and $V^{(2)}$ are the volume fluxes in directions 1 and 2, respectively. The total stencil for one momentum equation contains 21 velocity and 6 pressure points. The mass conservation is discretized using just four velocity points and without interpolation. The contribution of each pressure and velocity variable to the discrete derivatives can be found in [33]. Accurate discretization on non-uniform grids is achieved by taking into account the geometrical properties of the grid. Therefore, the volume flux is defined as a function of the covariant base vectors in such a way that it is continuous

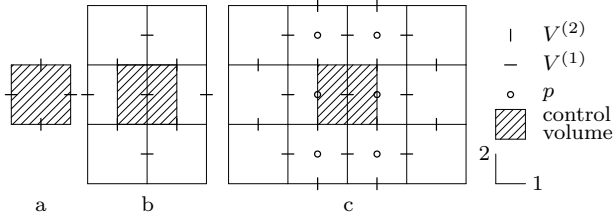


Figure 2.6. Control volume and discretization stencil for (a) the continuity equation, (b) the convection and (c) combined pressure and viscous terms of the momentum equation.

across cell faces. The covariant base vectors $\underline{a}_{(\alpha)}$ are defined by

$$\underline{a}_{(\alpha)} = \frac{\partial \underline{x}}{\partial \xi_{\alpha}}, \quad (2.26)$$

where \underline{x} and $\underline{\xi}$ are the coordinates in physical and computational space respectively. A grid cell in both of these spaces is shown in Fig. 2.7. In computational space each

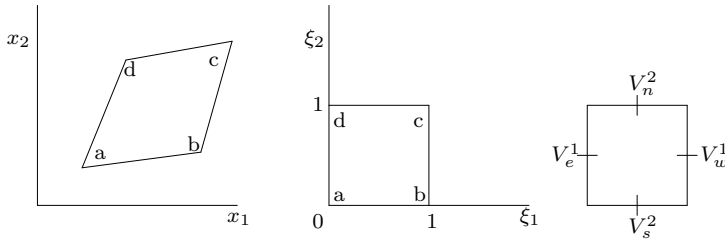


Figure 2.7. A grid cell in physical space, computational space and with its volume fluxes at the faces. The subscripts e, w, s, n denote east, west, south and north respectively.

cell is a square with the length of its sides equal to 1. The bilinear mapping from computational to physical coordinates is given by

$$\underline{x} = \underline{c}_1 + \underline{c}_2 \xi_1 + \underline{c}_3 \xi_2 + \underline{c}_4 \xi_1 \xi_2, \quad (2.27)$$

where \underline{c}_i are constants within each cell given by the coordinates of the corners of the cell

$$\underline{c}_1 = \underline{x}_a, \quad \underline{c}_2 = \underline{x}_b - \underline{x}_a, \quad \underline{c}_3 = \underline{x}_d - \underline{x}_a, \quad \underline{c}_4 = \underline{x}_a + \underline{x}_c - \underline{x}_b - \underline{x}_d. \quad (2.28)$$

The volume flux $V^{(\alpha)}$ is defined by

$$V^{(1)} = \underline{u} \otimes \underline{a}_{(2)}, \quad V^{(2)} = -\underline{u} \otimes \underline{a}_{(1)}, \quad (2.29)$$

where the operator \otimes is defined as

$$\underline{x} \otimes \underline{y} = x_1 y_2 - x_2 y_1. \quad (2.30)$$

Using Eq. (2.26)-Eq. (2.28) this can be rewritten as

$$V^{(1)} = \underline{u} \otimes (\underline{x}_d - \underline{x}_a + (\underline{x}_a + \underline{x}_c - \underline{x}_b - \underline{x}_d)\xi_1), \quad (2.31)$$

$$V^{(2)} = -\underline{u} \otimes (\underline{x}_b - \underline{x}_a + (\underline{x}_a + \underline{x}_c - \underline{x}_b - \underline{x}_d)\xi_2). \quad (2.32)$$

At the cell faces where the volume fluxes are located (see Fig. 2.7) this becomes

$$V_e^{(1)} = \underline{u} \otimes (\underline{x}_d - \underline{x}_a), \quad V_w^1 = \underline{u} \otimes (\underline{x}_c - \underline{x}_b), \quad (2.33)$$

$$V_s^{(2)} = -\underline{u} \otimes (\underline{x}_b - \underline{x}_a), \quad V_n^2 = -\underline{u} \otimes (\underline{x}_c - \underline{x}_d). \quad (2.34)$$

These expressions show that the volume flux only depends on the cell face where it is positioned on. This is necessary to get a continuous volume flux across cell faces.

In [32] the 3D staggered WesBeek discretization is given. For the definition of the volume flux a similar procedure can be followed as in 2D. A physical and computational cell are given in Fig. 2.8.

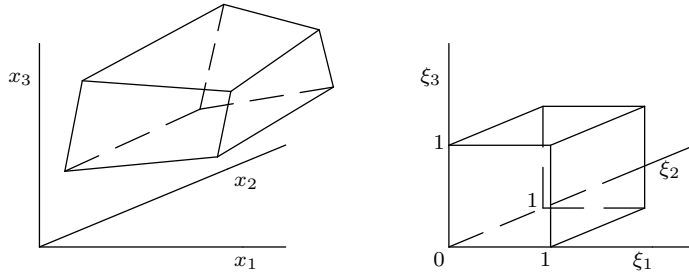


Figure 2.8. A grid cell in physical space and in computational space.

The bilinear mapping is

$$\underline{x} = \underline{c}_1 + \underline{c}_2\xi_1 + \underline{c}_3\xi_2 + \underline{c}_4\xi_3 + \underline{c}_5\xi_1\xi_2 + \underline{c}_6\xi_1\xi_3 + \underline{c}_7\xi_2\xi_3 + \underline{c}_8\xi_1\xi_2\xi_3, \quad (2.35)$$

where \underline{c}_i are constants within each cell. They are functions of the coordinates of the corners of the cell. The volume flux $V^{(\alpha)}$ is positioned at the middle of the cell face, where $\xi_\alpha = 0$ or $\xi_\alpha = 1$, $\xi_\beta = 0.5$, and $\xi_\gamma = 0.5$ and it is defined by

$$V^{(\alpha)} = a_{(\beta)} \times a_{(\gamma)} \cdot \underline{u}, \quad (2.36)$$

where α , β , and γ are cyclic. The covariant base vectors $\underline{a}_{(\beta)}$ and $\underline{a}_{(\gamma)}$ are drawn in Fig. 2.9. Each covariant base vector is the average of two opposite edges of the cell face. The length of the cross product of these base vectors is used to approximate the area of the cell face, since in general the cell face is curved. The volume flux again only depends on the geometry of the cell face where it is positioned on. This is necessary to get a continuous volume flux across cell faces.

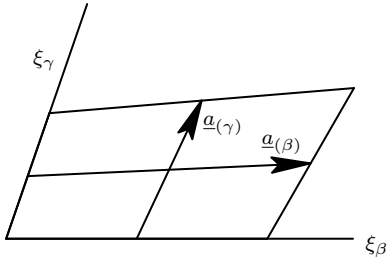


Figure 2.9. The covariant base vectors used to define the volume flux.

Going back to 2D, according to [33] in several publications the velocity is represented by $U^\alpha = \underline{u} \cdot \underline{a}^{(\alpha)}$, where $\underline{a}^{(\alpha)}$ are the contravariant base vectors that are defined as

$$\underline{a}^{(\alpha)} = \frac{\partial \xi_\alpha}{\partial \underline{x}}. \quad (2.37)$$

$U^{(\alpha)}$ can be written in terms of $V^{(\alpha)}$ as

$$U^{(\alpha)} = \frac{V^{(\alpha)}}{\sqrt{g}}, \quad (2.38)$$

where

$$\sqrt{g} = \frac{\partial \underline{x}}{\partial \xi_1} \otimes \frac{\partial \underline{x}}{\partial \xi_2} \quad (2.39)$$

is the Jacobian of the mapping. For the mapping of Eq. (2.27) it can be rewritten as

$$\sqrt{g} = \underline{c}_2 \otimes \underline{c}_3 + (\underline{c}_2 \otimes \underline{c}_4)\xi_1 + (\underline{c}_4 \otimes \underline{c}_3)\xi_2, \quad (2.40)$$

which is discontinuous across cell faces for general grids. This is the reason for bad accuracy when $U^{(\alpha)}$ is used. However, on a grid where for each cell its opposite faces are parallel ($\underline{c}_4 = 0$) and the cell surface $\underline{c}_2 \otimes \underline{c}_3$ is constant, the Jacobian \sqrt{g} is constant. So, on a skewed uniform grid $U^{(\alpha)}$ is continuous across cell faces.

Furthermore, using the WesBeek discretization, for a constant flow velocity u , the interpolation of the volume flux V to points between its grid nodes is such that when u is recomputed from the interpolated fluxes, the exact velocity is recovered. Another criterion is that irrespective of the grid, the discretization error must be zero for a flow with a constant velocity and a constant pressure gradient. Finally, the discretization avoids the use of Christoffel symbols by preceding the transformation of the equations to invariant form by the finite volume integration, removing the second derivative of the bilinear mapping.

The convection term can be discretized by a central or a first-order upwind scheme. The higher order upwind schemes that are implemented in DeFT are not accurate on non-uniform grids. The pressure and viscous terms are discretized with central schemes. For the temporal discretization the first-order Euler scheme is implemented, using a constant time step.

2.5 Solution procedure

Because the RANS equations for time-dependent incompressible flow are coupled, they should be solved as one system of equations. However, since the pressure is only present in the momentum equations and the continuity equation does not contain k and ϵ , the resulting global matrix of the system of linearized equations is ill-conditioned. To avoid this, the equations are solved sequentially, which reduces the size of the system of equations as well. Therefore, the pressure-correction method is used to solve the continuity and momentum equations. After that, the turbulence equations are solved. The discrete momentum equations are written as a system of linear equations

$$M \frac{u^{n+1} - u^n}{\Delta t} + B(u^n)u^{n+1} + Gp^{n+1} = F^{n+1} - A(u^n). \quad (2.41)$$

where M is the diagonal mass matrix, u is the velocity vector, n is the old time level on which the converged solution is known, $n + 1$ is the new time level on which the solution has to be calculated, Δt is the time step and B is the matrix with convective and viscous terms. B depends on the velocity at the old time level, because the convective term is linearized in the velocity at the new time level. G is the gradient matrix, p is the pressure vector, F is the vector with boundary conditions at the new time level and the vector A represents the part of the linearized convective term that depends on the velocity at the old time level only. This equation is solved for an intermediate velocity u^* using the pressure at the old time level.

$$M \frac{u^* - u^n}{\Delta t} + B(u^n)u^* + Gp^n = F^{n+1} - A(u^n). \quad (2.42)$$

u^* can be regarded as a prediction of the velocity u^{n+1} . When Eq. (2.42) is subtracted from Eq. (2.41) and the difference between the convection terms $B(u^n)(u^{n+1} - u^*)$ is neglected, the velocity correction equation arises

$$M \frac{u^{n+1} - u^*}{\Delta t} + G(p^{n+1} - p^n) = 0. \quad (2.43)$$

The pressure correction equation is subsequently derived by taking the divergence of Eq. (2.43) and using $Du^{n+1} = 0$ for incompressible flow, yielding

$$M \frac{-Du^*}{\Delta t} + DG\Delta p = 0, \quad (2.44)$$

where D is the divergence matrix and

$$\Delta p = p^{n+1} - p^n, \quad (2.45)$$

the pressure difference between two time levels.

The solution algorithm for the RANS equations is shown in Fig. 2.10. First, the known solution at the old time level n is used as the first iterate in the iteration loop. Then, the equations are solved sequentially, where the most recently calculated

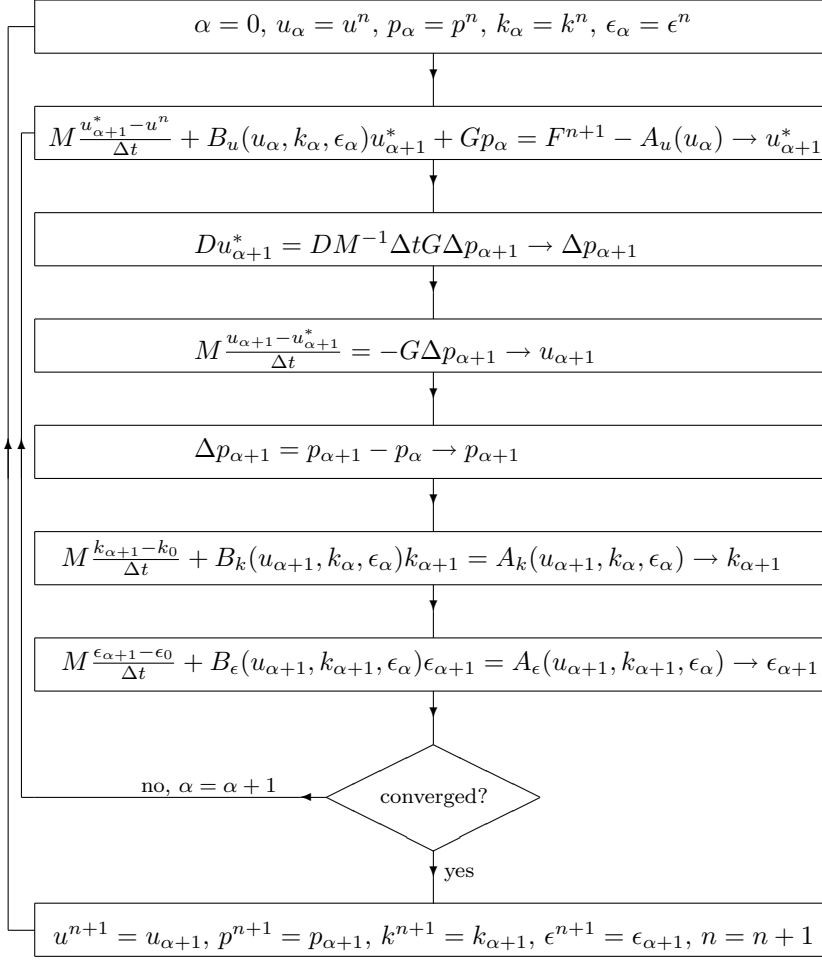


Figure 2.10. The solution algorithm, with the time step loop (outer) and the iteration loop (inner). For u , u^* , p , Δp , k and ϵ the superscript n denotes the time level and the subscript α the iteration level.

values of the unknowns are used to construct matrix B and vector A . After that, the iteration loop starts again and continues until convergence of the non-linear coupled equations is reached. A convergence criterion for the iteration loop in Fig. 2.10 is not implemented; instead, a fixed number of iterations is performed. Finally, the outer loop, representing the time stepping, continues to the next time level.

In the core of the solver, matrix equation $Ax = b$ is solved using the iterative GMRESR method. This method is proposed in [29] and tested using the Navier-Stokes equations in [30]. In the matrix equation all discrete velocity, pressure, k or ϵ unknowns of all blocks are present. The convergence criterion for the iterative matrix

solver depends on the residual vector of the global matrix equation $Ax = b$, which is defined as $r = b - Ax$. The relative convergence criterion used in DeFT is based on the initial residual $r_0 = b - Ax_0$ with the initial iterate x_0 . Iteration x_k is considered a converged solution of the equation if $\epsilon_c \|r_0\|_2 > \|r_k\|_2$, where ϵ_c is specified by the user. The default value for ϵ_c is 10^{-4} for the pressure equation and 10^{-3} for the other RANS equations.

In order to perform the matrix vector multiplications in the GMRESR algorithm, the global matrix and vector are extended with the virtual part. For example, the matrix equation for three blocks is

$$\begin{bmatrix} A_{1r} & A_{1v} & \emptyset & \emptyset & \emptyset & \emptyset \\ \emptyset & \emptyset & A_{2r} & A_{2v} & \emptyset & \emptyset \\ \emptyset & \emptyset & \emptyset & \emptyset & A_{3r} & A_{3v} \end{bmatrix} \begin{pmatrix} x_{1r} \\ x_{1v} \\ x_{2r} \\ x_{2v} \\ x_{3r} \\ x_{3v} \end{pmatrix} = \begin{pmatrix} b_{1r} \\ b_{2r} \\ b_{3r} \end{pmatrix}, \quad (2.46)$$

where A_{1r} , A_{1v} , x_{1r} and x_{1v} are the real and virtual part of the matrix and vector for block 1 respectively. Because the virtual part is included in the matrix equation, there are more unknowns than equations. However, for a matrix vector multiplication this is not a problem. The virtual values of x are interpolated from the real values of x from a neighboring block, before the multiplication is carried out. In this way, the global multiplication is done at block level. The extension from matching to non-matching blocks does not affect the structure of the global matrix. Updating the virtual variables only changes from copying to interpolating from the neighboring block.

After an equation is solved, the virtual cells are updated with the new solution. When the velocity prediction is calculated, the velocity which is calculated at the multi block boundary, is averaged with its corresponding velocity at the neighboring block. It is necessary to have a unique value of this velocity to achieve convergence of the pressure equation. Also within the iterative matrix solver, there is information exchange between blocks. The residual and error in the solution are communicated across block boundaries.

The solver in DeFT is designed for time-dependent flows. There is no solver where the acceleration term of the Navier-Stokes equations is omitted. When a stationary flow is simulated, the solution is carried on in time until the flow is stationary.

2.6 Multi block exchange of primitive variables

In case the computational domain is divided into multiple blocks, the double row of virtual cells around each block plays an important role in the block coupling. The virtual cells of a block overlap the first two rows of the real grid of the neighboring block. Matching grids can be used in simple geometries. But for complex geometries, matching grids can be difficult to construct and often result in very skewed and stretched cells. To improve the grid quality, it is necessary to allow non-matching grids.

Non-matching grid

For non-matching grids, the virtual cells along the multi block boundary, do not match the real cells of the neighboring block, as already shown in Fig. 2.5. Therefore the variables can not be copied from one block to another, but interpolation in the direction parallel to the block boundary is needed. The resulting interpolation errors are a drawback of non-matching grids. The interpolation of variables from the real part of the grid to the overlapping virtual part is shown in Fig. 2.11. The unknown

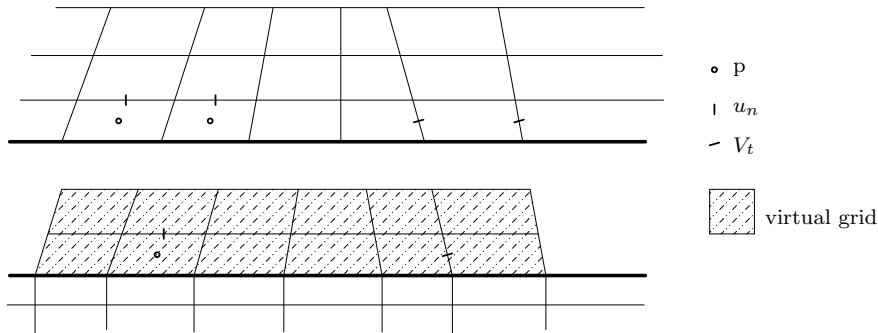


Figure 2.11. Interpolation of the pressure p , normal velocity u_n and tangential volume flux V_t from the nearest neighbors on the real grid to the virtual grid.

values in the virtual grid are linearly interpolated between the two nearest neighbors from the overlapping real grid. The volume flux normal to the block face is not interpolated directly. Because the velocity is continuous across the block face, the volume flux is discontinuous if the length of the cells in the direction parallel to the block boundary is different in both blocks. This is why the normal velocity is interpolated instead.

Sliding interface

To couple the moving grid of the rotor to the stationary grid of the casing, a sliding interface is necessary. The sliding interface must be able to handle non-matching grids. The connections between cells from the rotating and the stationary part change at the start of every time step in Fig. 2.10. Because the shape of the virtual grid depends on the shape of the overlapping real grid, the geometry of the virtual grid changes every time step as well.

The flow in the blocks of the rotating part of the domain is calculated in the rotating frame of reference. Therefore, variables have to be transformed from the moving to the stationary reference frame. The rotor velocity has to be added to the relative velocity to get the absolute velocity. The pressure, k and ϵ do not have to be transformed across the sliding interface.

The transformation of the pressure difference Δp between two time levels from the moving to the stationary reference frame is not straightforward. Across the sliding interface this variable is discontinuous during the first iteration of the loop over the equations, because it becomes a pressure difference in space as well. In Fig. 2.12 two

radial lines across the sliding interface are shown. The angle between the lines equals

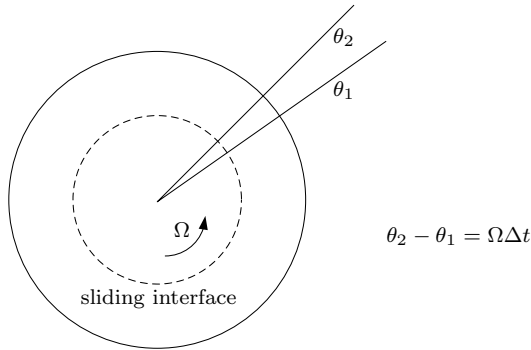


Figure 2.12. Radial lines across the sliding interface at θ_1 and θ_2 .

the rotation of the inner part of the domain in one time-step. The lower curve in Fig. 2.13 represents the pressure at time level n on the radial line θ_2 . When the variables

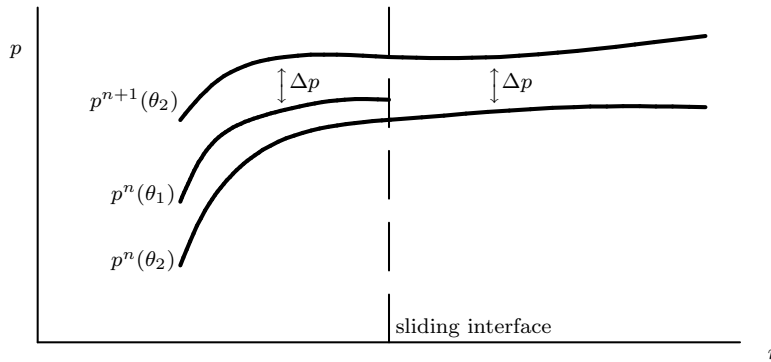


Figure 2.13. Pressure levels at the radial line θ_2 , as a function of the radial coordinate.

are calculated at the next time level $n + 1$, the domain within the sliding interface is rotated, before the iteration loop over the equations starts. In the rotated part of the domain, the pressure distribution at the line θ_2 changes from $p^n(\theta_2)$ to $p^n(\theta_1)$, which makes the pressure at this line discontinuous across the sliding interface. The pressure at the new time level $p^{n+1}(\theta_2)$ is continuous across the sliding interface, but the pressure difference $\Delta p = p^{n+1}(\theta_2) - p^n(\theta_2)$ is discontinuous. In section 3.5, where the sliding interface is tested, it turns out that the pressure equation can be solved for Δp when the sliding interface is used. However, several pressure-correction iterations are needed to eliminate the discontinuity.

To avoid this problem, the pressure equation Eq. (2.44) is rewritten as

$$DM^{-1}\Delta t G p_{\alpha+1} = Du_{\alpha+1}^* + DM^{-1}\Delta t G p_{\alpha}. \quad (2.47)$$

By putting the known pressure from the current iteration level in the right hand side and solving directly for the pressure at the new iteration level, a discontinuity in the variable that is solved is avoided. This method is verified in section 3.5 as well.

Chapter 3

Verification

In this chapter a number of relatively simple flow simulations are presented. The goal is to verify the correct implementation of DeFT as well as to verify the statements from theory concerning accuracy and calculation time. In section 3.1, a time-dependent channel flow is simulated by DeFT and Fluent. The calculation time and the accuracy of the calculated solution are compared. In section 3.2 the staggered discretizations (both classical and WesBeek) and a collocated discretization are compared for a flow on a rough grid. Calculations in a rotating frame of reference are the subject of section 3.4, for laminar flow, and section 3.3, for turbulent flow. Finally, in section 3.5, the correct implementation of the sliding interface is verified.

3.1 Unsteady channel flow

The potential difference in performance between collocated and staggered-grid methods is illustrated for a simple laminar, but unsteady, channel flow. The block topology of the grid and the number of grid cells were selected to reflect the case of an actual pump simulation in 2D. In Fig. 3.1 the geometry of the channel is given, as well as the dimensions of the uniform grid that consists of 10 blocks of 100 times 100 cells. The

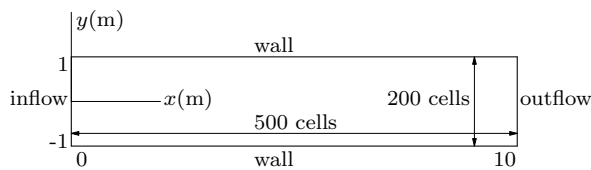


Figure 3.1. The size of the channel and the boundary conditions of the flow.

walls are modeled by the noslip condition. At the outflow boundary, Fluent imposes zero pressure, where DeFT prescribes a parallel outflow, which means zero tangential velocity and zero normal stress. The time-dependent velocity prescribed at the inlet

boundary is

$$u_x = \Re(u_s(1 - (\frac{2y}{b})^2) + 2u_d(\cosh(\omega y) - \cosh(\frac{\omega b}{2})) \exp(\nu\omega^2 t - a)), \quad (3.1)$$

$$u_y = 0, \quad (3.2)$$

where

$$\begin{aligned} u_s &= 10 \text{ ms}^{-1}, & u_d &= 0.5 \text{ ms}^{-1}, \\ b &= 2 \text{ m}, & \nu &= 0.01 \text{ m}^2\text{s}^{-1}, \\ a &= 20, & \omega &= 20(1 + i) \text{ m}^{-1}, \end{aligned}$$

with $\Re(x)$ denoting the real part of x , i the imaginary unit, ν the fluid kinematic viscosity and b the width of the channel. The inlet velocity profile is plotted in Fig. 3.2 for three different points in time. The dynamic part of the velocity with maximum

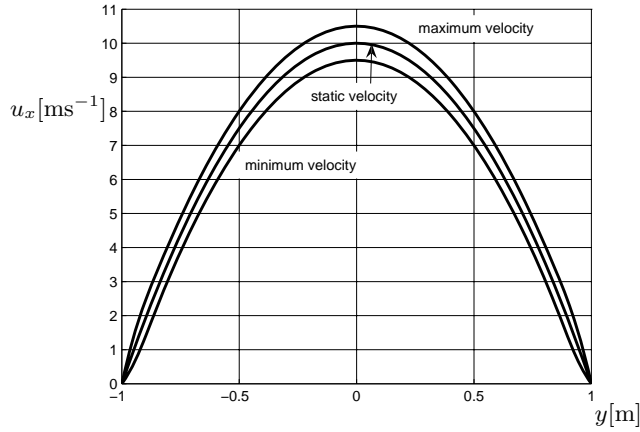


Figure 3.2. The maximum, minimum and static inlet velocity profile.

amplitude u_d in the center of the channel is added to the static part of the velocity with its maximum value u_s . The Reynolds number based on the average velocity at the center of the channel u_s and the channel width b is 2000. Both Fluent and DeFT are used to simulate this flow, starting from an initial condition of zero pressure and velocity. For temporal discretization the first-order Euler scheme is used with a time step of 0.0025 s. The convective terms are discretized with a central scheme in DeFT and the QUICK scheme in Fluent.

To quantify the accuracy of the numerical calculations, the results are compared with the analytical solution of the time-dependent channel flow. The flow is derived by setting $u_y = 0$. From the momentum equation in y -direction it now follows that $\frac{\partial p}{\partial y} = 0$ and from the continuity equation it follows that $\frac{\partial u_x}{\partial x} = 0$. The momentum equation in the x -direction yields

$$\frac{\partial u_x}{\partial t} + \frac{\partial p}{\partial x} = \nu \frac{\partial^2 u_x}{\partial y^2}. \quad (3.3)$$

The analytical solution of this equation for the velocity is given by Eq. (3.1), which does not depend on x and Eq. (3.2). The pressure is given by

$$p = \Re(\nu\rho(L-x)\left(\frac{8u_s}{b^2} - 2\omega^2 u_d \cosh\left(\frac{\omega b}{2}\right) \exp(\nu\omega^2 t - a)\right)), \quad (3.4)$$

where the fluid density $\rho = 1 \text{ kgm}^{-3}$ and the length of the channel equals $L = 10 \text{ m}$. The pressure at the inlet of the channel is shown as a function of time in Fig. 3.3. For both the velocity and the pressure, the static part is proportional to u_s and

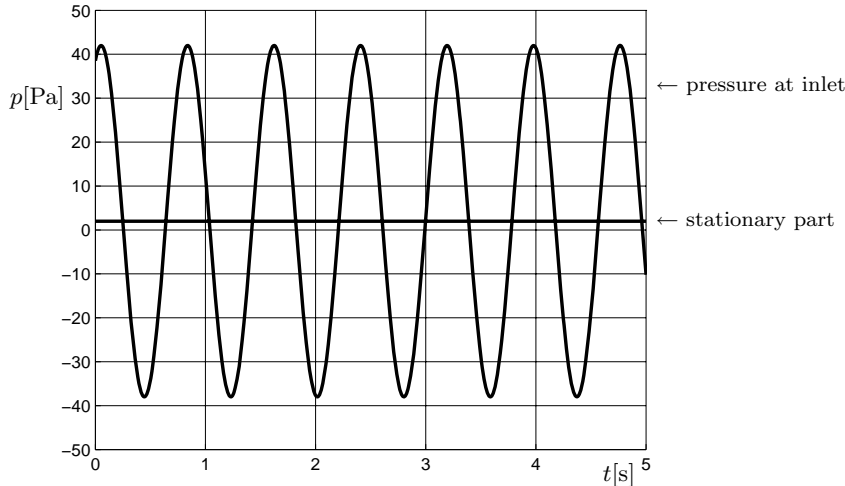


Figure 3.3. The pressure at the inlet as a function of time. The stationary part of the pressure is given separately.

the amplitude of the dynamic part is proportional to u_d . Note that while the the amplitude of the velocity u_d is only 5% of the the static velocity u_s , the dynamic part of the pressure is 20 times larger than the static part of the pressure in Fig. 3.3.

To compare the accuracy of the simulations, the calculated average pressure at the channel inlet is monitored. In Fig. 3.4 (DeFT) and Fig. 3.5 (Fluent) the error ϵ_p is plotted as a function of time. The error is normalized by the amplitude of the analytical pressure fluctuation at the inflow boundary, which is 40 Pa. The error-curves for DeFT and Fluent are almost equal, except for small oscillations that are present in the Fluent result. Because the numerical initial solution does not correspond to the exact solution, the error in the inlet pressure is large during the first 2.5 s. The error in the pressure is oscillating because the pressure in the numerical calculation shows a phase lag with respect to the analytical solution. When the inlet pressure is at its maximum, for example at $t \approx 4 \text{ s}$, its derivative with respect to time is zero. Here, the phase lag has only a small influence and ϵ_p is close to zero. When the derivative of the inlet pressure with respect to time is large, for example at $t \approx 5 \text{ s}$, the phase lag causes ϵ_p to be large as well.

Different settings for the convergence criteria and the number of pressure-correction iterations were evaluated. For the residual of the pressure equation, the minimum

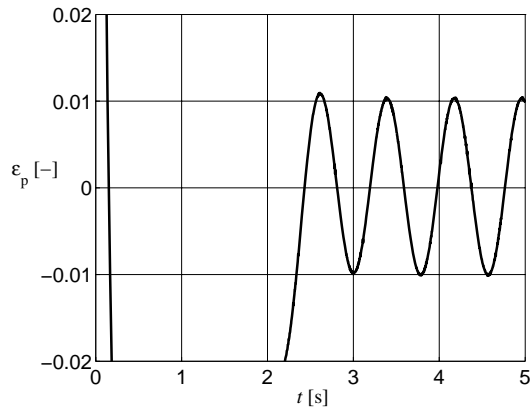


Figure 3.4. Normalized error ϵ_p in average inlet pressure for the calculation with DeFT.

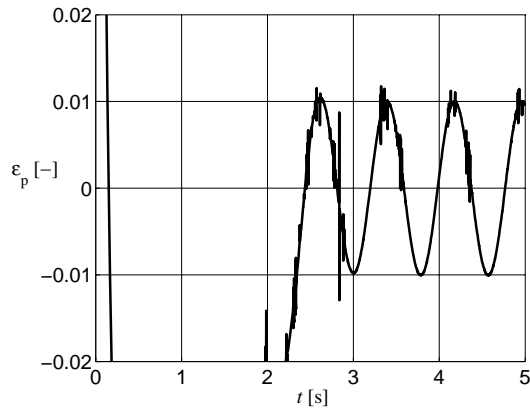


Figure 3.5. Normalized error ϵ_p in average inlet pressure for the calculation with Fluent.

value that Fluent could attain was between 10^{-4} and 10^{-5} . When the convergence criterion for this equation was set to its default value of 10^{-3} , the amplitude of the error ϵ_p was approximately 1. The different settings were selected such that ϵ_p reduced to within 0.01 in the shortest possible calculation time. Fluent took about 13.5 hours with 40 pressure-correction iterations per time-step, while DeFT only needed 1 pressure-correction iteration per time-step and 4 hours calculation time. Both simulations were on 1 core of a dual core Intel Xeon 5130 2GHz processor. Despite the fact that Fluent, unlike DeFT, treats the whole domain as one grid and uses a multi-grid method to accelerate the calculation, the performance of DeFT is superior for this flow simulation.

3.2 Accuracy on a rough grid

Wesseling showed in [33] that the WesBeek discretization is accurate on a non-smooth grid for the example of a Poiseuille flow. For this flow the convection is zero and the pressure gradient is constant. In this section a different two-dimensional flow is used to show the accuracy on a rough and a smooth grid and on a grid that is uniform in polar coordinates. The flow simulations are performed using the classical and WesBeek staggered discretization using DeFT and a collocated discretization using Fluent. The problem represents the flow through a vaneless diffuser with constant height. The domain and the grid are shown in Fig. 3.6. The domain is given by

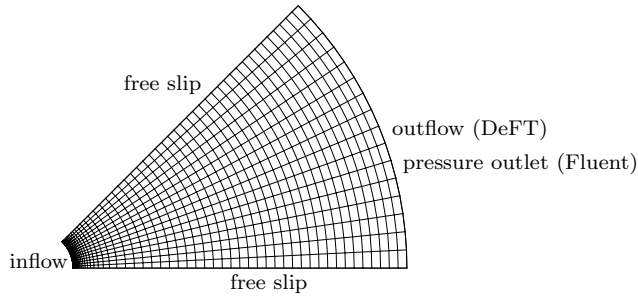


Figure 3.6. Flow domain, boundary conditions and the smooth non-uniform grid.

$$0.05 \leq r \leq 0.5, \quad 0 \leq \theta \leq \frac{\pi}{4}, \quad (3.5)$$

with r the radial coordinate in m. In radial and tangential direction 64 and 16 cells are used respectively. The radial cell length is increasing with the radius, because the velocity and the pressure gradient are decreasing with r . A locally deformed grid for the same domain is plotted in Fig. 3.7. Besides these two grids, an equidistant

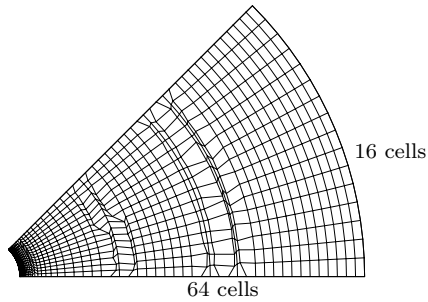


Figure 3.7. Rough non-uniform grid.

grid in polar coordinates is used as well, with 512 cells in radial direction and 16 cells in tangential direction. The boundary condition types are given in Fig. 3.6 as well. The inflow velocity is 1 ms^{-1} in radial direction. The fluid density $\rho = 1 \text{ kgm}^{-3}$ and its dynamic viscosity $\mu = 0.001 \text{ kgm}^{-1}\text{s}^{-1}$. The Reynolds number based on the inlet velocity and the length of the domain in radial direction is 450. The flow is given

analytically by

$$v = 0, \quad u = \frac{u_o r_o}{r}, \quad p = \frac{1}{2} \rho (u_o^2 - u^2) - 2\mu \frac{u_o}{r_o}, \quad (3.6)$$

where v is the velocity in tangential direction, u the radial velocity, and $u_o = 0.1 \text{ ms}^{-1}$, where the subscript o denotes the outflow edge of the domain.

For the rough grid, the resulting pressure distribution for the collocated, WesBeek staggered and the classical staggered discretization are given in Fig. 3.8, Fig. 3.9 and Fig. 3.10 respectively. Except for the results of the classical staggered discretization,

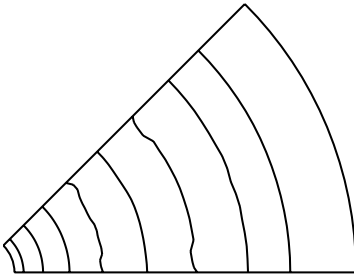


Figure 3.8. Pressure contours for the collocated discretization on the rough grid.

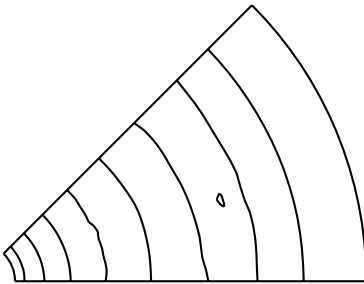


Figure 3.9. Pressure contours for the WesBeek discretization on the rough grid.

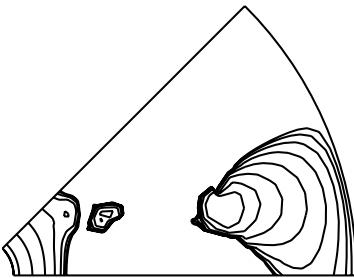


Figure 3.10. Pressure contours for the classical staggered discretization on the rough grid.

the pressure contours are close to lines at constant radius. On the smooth and the equidistant grid the pressure contours are even more rotational symmetric, also using the classical staggered discretization. The analytical pressure difference across the diffuser is 0.495 Pa. The numerical results for this parameter are given in Tab. 3.1. For

	equidistant	smooth	rough
collocated	0.488	0.494	0.492
WesBeek staggered	0.494	0.495	0.498
classical staggered	0.494	0.500	0.444

Table 3.1. Pressure difference [Pa] across the diffuser for different grids and discretizations. The theoretical value is 0.495 Pa.

the collocated method the error on the equidistant grid is larger than on the smooth and even the rough grid. Because odd-even decoupling is worst on uniform grids (section 1.3), this larger error can be the result of the artificial odd-even coupling that is associated with collocated grids. The classical staggered discretization is designed for equidistant grids only. On the smooth non-uniform grid and especially on the rough grid the error in the pressure difference is large. On the rough grid, the WesBeek staggered and the collocated discretization have equal accuracy. The overall accuracy of the WesBeek staggered discretization is better than the accuracy of the classical staggered and the collocated discretization.

3.3 Turbulence model in the rotating frame

In this section the correct implementation of the $k - \epsilon$ turbulence model is verified by solving a turbulent flow in the stationary and the rotational frame of reference. When the shape of the domain is circular, the boundaries of the domain coincide with the boundaries of the rotated domain. This is convenient for prescribing the boundary conditions at the correct location in both frames, since in DeFT the shape of the domain is not allowed to change during a simulation. In this section the flow is periodic in the direction of the rotation, which provides the opportunity to solve only one period of the domain.

The streamlines, block topology and boundary conditions of the flow in the stationary frame of reference are shown in Fig. 3.11. To the left of the inflow boundary

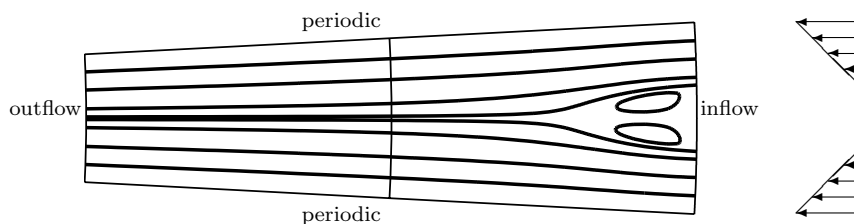


Figure 3.11. The block topology, boundary conditions and streamlines of the flow in the stationary frame of reference.

where a zero velocity is prescribed, there is an area of reverse flow. The upper and lower boundaries are lines that are 6 degrees apart and the left and right boundaries are parts of circles with their centers at the intersection of the two lines. The angle between the radial lines is 6 degrees. The radius of the outflow boundary equals 1 m, while the inflow boundary is at 1.5 m. In tangential direction the equidistant grid consists of 360 cells. In radial direction there are 60 cells, while the grid is refined towards the inflow boundary.

The density equals 1 kgm^{-3} and the dynamic viscosity is $10^{-4} \text{ kgm}^{-1}\text{s}^{-1}$. The maximum of the radial inflow velocity profile given in Fig. 3.11 is 1 ms^{-1} . The velocity profile has a linear part from 0 to 1. When a step function is used instead, the grid in the inflow region needs to be much finer. This is avoided to reduce the calculation time. The Reynolds number based on the maximum inflow velocity and the length of the domain in radial direction is 5000. At the outlet zero stress is prescribed. For the turbulence equations $k = 10^{-2} \text{ m}^2 \text{ s}^{-2}$ and $\epsilon = 10^{-4} \text{ m}^2 \text{ s}^{-3}$ are prescribed at the inflow boundary. At the outflow the normal gradients of both k and ϵ are set to zero. For the convective terms of the momentum and turbulence equations the first-order upwind scheme is used. Temporal discretization is done with the first-order Euler scheme using a time-step of 10^{-3} s .

In the rotating frame of reference, both blocks rotate with an angular velocity $\Omega \approx 0.29 \text{ rads}^{-1}$ such that the rotation during one time-step corresponds with the length of one cell in tangential direction. This is convenient for prescribing the inflow velocity profile, because it rotates along the inflow boundary with $-\Omega$. In the rotating frame of reference the flow is periodic in time, with a period of 360 time-steps. The Coriolis and centrifugal forces are modeled using the source-term formulation. The streamlines in the rotating domain are given in Fig. 3.12. In Fig. 3.13 pressure contours of the solutions in the stationary and rotating frame are plotted. These results

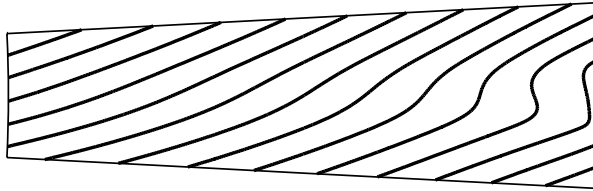


Figure 3.12. The streamlines of the jet flow in the rotating frame of reference.

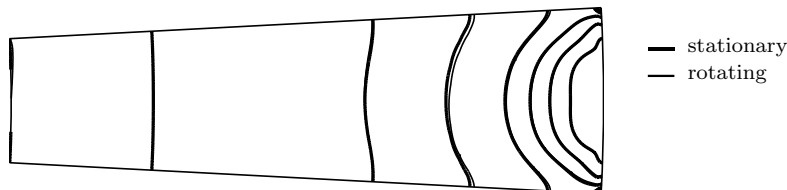


Figure 3.13. Pressure contours of the solutions in the rotating and stationary frame of reference.

agree very well, which suggests that the turbulence model is implemented correctly. However, the viscous terms in the momentum equations can be very small, such that the turbulence model has no significant influence on the pressure. Therefore the simulation in the stationary frame of reference is repeated with the turbulent kinetic energy at the right boundary decreased to $0.7 \cdot 10^{-2} \text{m}^2 \text{s}^{-2}$. The pressure contours are shown in Fig. 3.14. Because the isobars are clearly different in the inflow part of

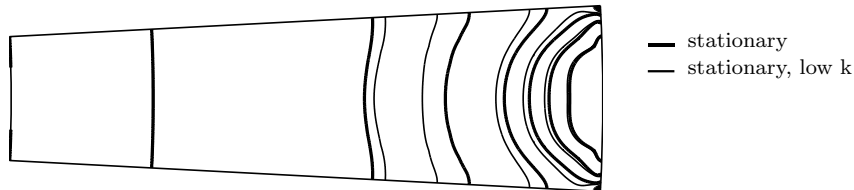


Figure 3.14. Pressure contours with smaller turbulent kinetic energy at the right boundary.

the domain, the turbulent viscosity has a significant influence on the pressure in that region. From Fig. 3.13 it can now be concluded that the turbulence model gives the same results in the stationary and the rotating frame of reference.

3.4 Coriolis and centrifugal forces

In section 2.2.2, the treatment of centrifugal and Coriolis forces in conservative formulation was introduced. It served as an alternative to the implementation of these apparent forces as source terms in case the Navier-Stokes equations are to be solved in a rotating coordinate system. A comparison between the two methods is addressed in this section. A stationary laminar and axi-symmetric flow is calculated on a domain consisting of four blocks, as given in Fig. 3.15. At the inflow boundary the radius is 1

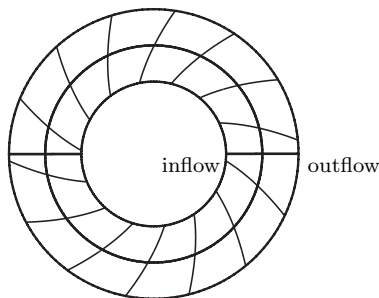


Figure 3.15. Block-structure and streamlines of the axi-symmetric flow in the steady frame of reference.

m, a normal velocity of 1ms^{-1} and a tangential velocity of 0.5ms^{-1} in the stationary frame of reference are prescribed. At the outflow boundary the radius is 2 m and an

outflow boundary condition is imposed. The fluid density is equal to 1 kgm^{-3} and the dynamic viscosity is $0.01 \text{ kgm}^{-1}\text{s}^{-1}$. The Reynolds number based on the normal inlet velocity and the distance between the inlet and outlet boundary is equal to 100. The streamlines of the flow in the stationary frame of reference are given in Fig. 3.15 as well.

The flow is simulated on four uniform grids: a coarse and a fine grid, both matching and non-matching. Each block of the coarse matching grid has 20 cells in radial direction and 80 cells in circumferential direction. The non-matching grid has 21 cells in radial direction in the 2 lowest blocks of Fig. 3.15. For the non-matching grid, the rotating blocks are shifted half a cell in the circumferential direction in order to make the grid along the sliding interface non-matching as well, see Fig. 3.16. The fine grids have twice the number of cells of the coarse grids in each direction. A part of the coarse non-matching grid is shown in Fig. 3.16.

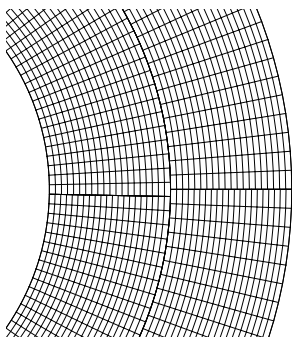


Figure 3.16. Part of the coarse non-matching grid.

For each grid three different simulations are done: a calculation in the steady frame of reference for the entire domain (1), and two simulations in which part of the domain rotates, using source terms (2) and the conservative formulation (3) to account for the apparent forces. For the two latter simulations, the two inner blocks rotate at a speed of 0.5 rads^{-1} where the connection to the outer blocks is through a sliding interface. Each time step the grid rotates over one cell. The central discretization scheme is used for the convective terms, while the Euler scheme is used for the time discretization.

The error in the pressure of the numerical solution ϵ_p is calculated using the L2-norm

$$\epsilon_p = \sqrt{\frac{1}{n} \sum_{i=1}^n (p_{a,i} - p_i)^2}, \quad (3.7)$$

where p_i is the numerically calculated pressure, p_a is the analytical pressure, and n is the total number of cells. The error is given in Tab. 3.2 for the different cases. Both on the fine and the coarse grid the error hardly depends on the case. The reduction of the error by a factor of 4 when going from the coarse to the fine grid is consistent with the second order accuracy of the spatial discretization. There is no preference

reference frame	stationary		partly rotating			
apparent forces			conservative formulation		source term formulation	
interfaces	matching	non-matching	matching	non-matching	matching	non-matching
ϵ_p , coarse	$6.5 \cdot 10^{-5}$	$6.9 \cdot 10^{-5}$	$7.0 \cdot 10^{-5}$	$7.4 \cdot 10^{-5}$	$6.4 \cdot 10^{-5}$	$6.6 \cdot 10^{-5}$
ϵ_p , fine	$1.6 \cdot 10^{-5}$	$1.7 \cdot 10^{-5}$	$1.7 \cdot 10^{-5}$	$1.8 \cdot 10^{-5}$	$1.7 \cdot 10^{-5}$	$1.6 \cdot 10^{-5}$
$\frac{\epsilon_p, \text{coarse}}{\epsilon_p, \text{fine}}$	4.0	4.1	4.1	4.2	3.9	4.0

Table 3.2. Pressure error ϵ_p using a coarse or a fine, a matching or a non-matching, and a stationary or a partly rotating grid with sliding interface and conservative or source term formulation of the Coriolis and centrifugal forces.

for the conservative or the source term formulation. The interpolation along the non-matching block faces only gives a small increase in the error and does not decrease the order of accuracy.

3.5 Sliding interface

In this section the implementation of the sliding interface is tested by simulating a laminar flow around a cylinder. The domain, block topology and the boundary conditions are given in Fig. 3.17. On the left side the inflow velocity is 1 ms^{-1} in

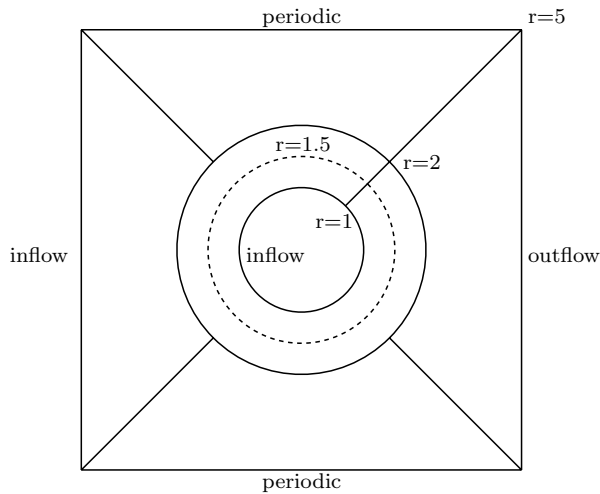


Figure 3.17. Block topology and boundary conditions of the domain around the cylinder.

horizontal direction. On the cylinder, a normal velocity of 0.5 ms^{-1} is prescribed. This avoids flow separation with vortices and thus the need for a fine grid to resolve vortices. Because of the periodic boundary conditions at the upper and lower edge,

this domain can be seen as part of a cascade of cylinders. The grid of the upper left part of the domain is shown in Fig. 3.18. The ring-shaped blocks have 16 times

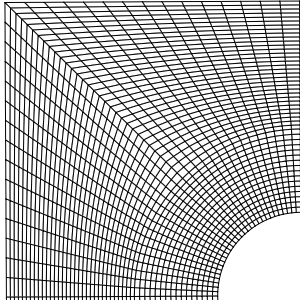


Figure 3.18. Part of the grid around the cylinder. In this plot the number of cells is reduced by a factor 2 in each direction.

240 cells, while the other blocks consist of 60 times 64 cells. The grid is matching everywhere, also when the sliding interface between the two inner blocks is used. The fluid density and dynamic viscosity are 1 kgm^{-3} and $0.1 \text{ kgm}^{-1}\text{s}^{-1}$ respectively. The Reynolds number based on the diameter of the cylinder and the inflow velocity of 1 ms^{-1} is 20. When the sliding interface is used, the inner block rotates with an angular velocity of 0.5 rads^{-1} . Together with the condition of one cell rotation per time-step along the sliding interface, this determines the time step at approximately 0.052 s. The central scheme is used for discretization of the convective terms. The conservative implementation of the Coriolis and centrifugal forces is used.

The streamlines of the flow are shown in Fig. 3.19. The pressure contours resulting

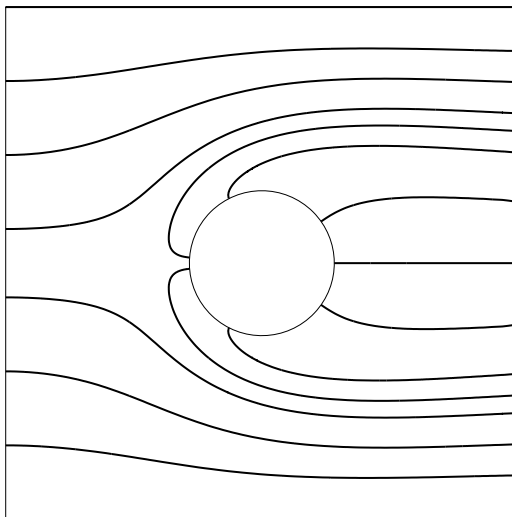


Figure 3.19. The streamlines of the flow through the cascade of cylinders.

from the simulation in the stationary frame and the simulation with the inner block in the rotating frame are given in Fig. 3.20. The result of the simulation with the sliding

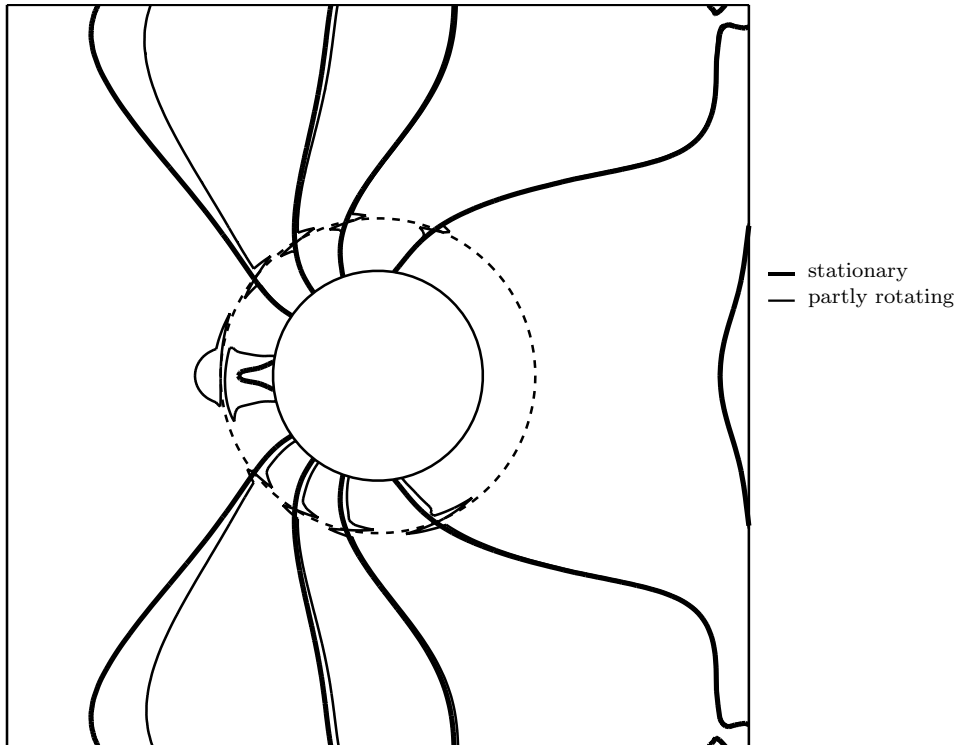


Figure 3.20. Isobars of the flow along a cylinder, calculated using one pressure-correction iteration, for both a stationary and a partly rotating domain and solving the pressure equation for Δp .

interface shows a discontinuity at the sliding interface, because the pressure equation was solved for Δp and only one pressure-correction iteration was used. When this number is increased, the pressure discontinuity decreases, as can be seen in Fig. 3.21, where three pressure-correction iterations were used. In Fig. 3.22 the pressure on the vertical line from the center of the cylinder to the lower side of the flow domain is plotted. The pressure discontinuity at the sliding interface ($r = 1.5$ m) decreases if more pressure-correction iterations are done. However, the simulation with sliding interface was also done for the case where the pressure equation is solved for p^{n+1} instead of Δp . With only a single pressure-correction iteration, the resulting pressure contours are indistinguishable from those of the simulation in the stationary frame of reference. That is why it is preferred to solve the pressure equation for p^{n+1} when a sliding interface is used.

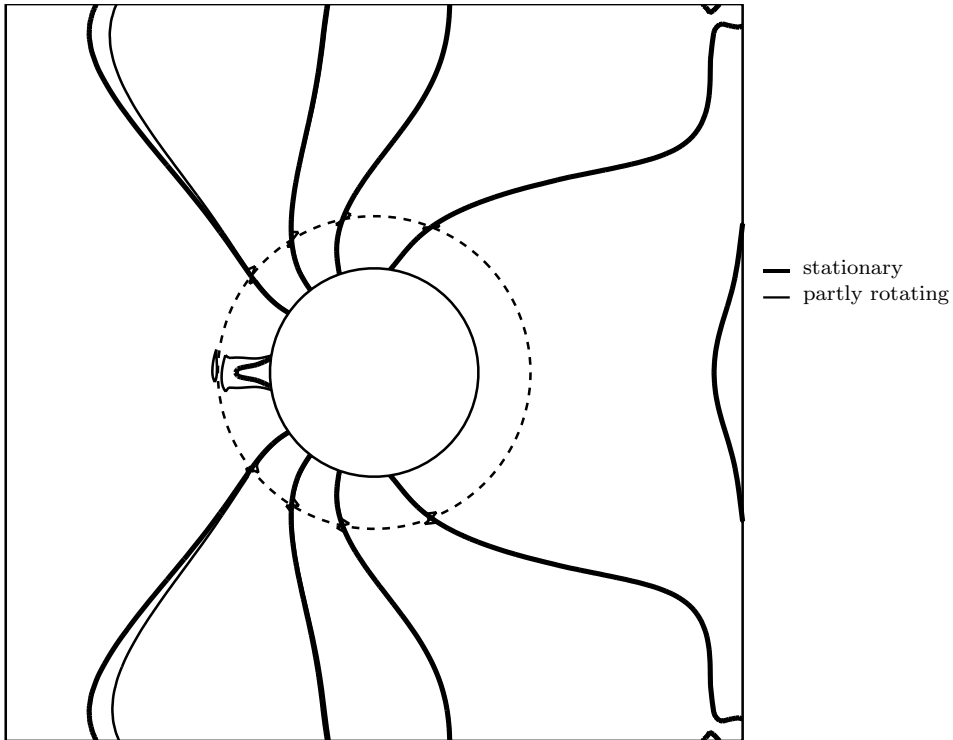


Figure 3.21. Isobars of the flow along a cylinder, calculated using three pressure-correction iterations, for both a stationary and a partly rotating domain and solving the pressure equation for Δp .

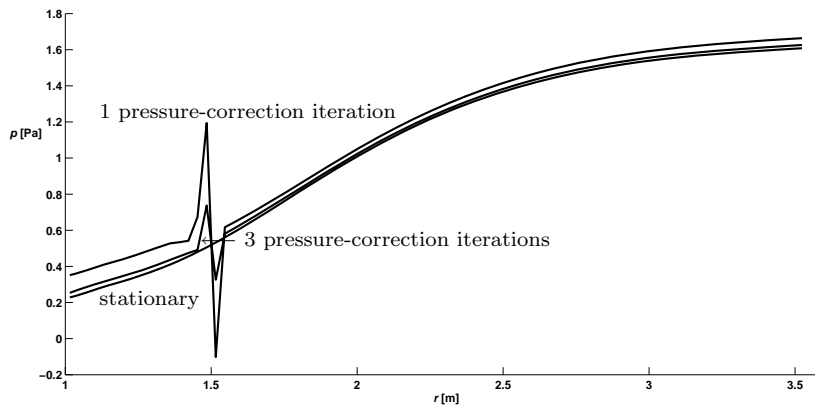


Figure 3.22. The pressure on the vertical line from the center of the cylinder to the lower boundary of the flow domain. The pressure equation is solved for Δp , using 1 or 3 pressure-correction iterations in the partly rotating domain. The solution obtained in the stationary frame is shown as well.

Chapter 4

Validation

As a first step towards calculating a complete turbomachine, the flow through a cascade is calculated. A cascade is an infinite row of blades that can be regarded as a two-dimensional model for an axial turbomachine, see Fig. 4.1. This model assumes that the flow through the turbomachine is in radial equilibrium. For the flow through the cascade, the pressure distribution and the total force on a blade are calculated using DeFT and Fluent. This force is expressed both in terms of lift and drag components and in terms of axial and tangential components. The results are compared with experimental and numerical results obtained from literature. The goal of this comparison is to validate DeFT for this type of flow. In the next sections the measurements, the CFD models in DeFT and Fluent, and the comparison of the results are given.

4.1 Measurements

Measurements of the flow through cascades of NACA 65-series compressor blade sections are described in [12]. The influence of many combinations of inlet angle β_1 , angle of attack α_1 , solidity σ and blade shape on lift coefficient C_l , drag coefficient C_d and pressure distribution coefficient C_p is presented. The geometry of the cascade is shown in Fig. 4.1. It is determined by the stagger angle $\gamma = \beta_1 - \alpha_1$ and the solidity $\sigma = c/s$, where c is the blade chord and s the pitch. A two-dimensional cascade tunnel with 7 blades was used to simulate the infinite blade row. The chord length of the blades was 0.1270 m. The experimental setup is shown in Fig. 4.2. The low-speed tests were within the incompressible speed range. An open air circuit was used, where the air velocity was 29 ms^{-1} and the chord based Reynolds number was 245000. Porous flexible walls and a suction chamber were used to control boundary layer build up and to ensure the flow being uniform and two dimensional.

The pressure coefficient is defined by

$$C_p = \frac{2(p - p_1)}{\rho u_1^2}, \quad (4.1)$$

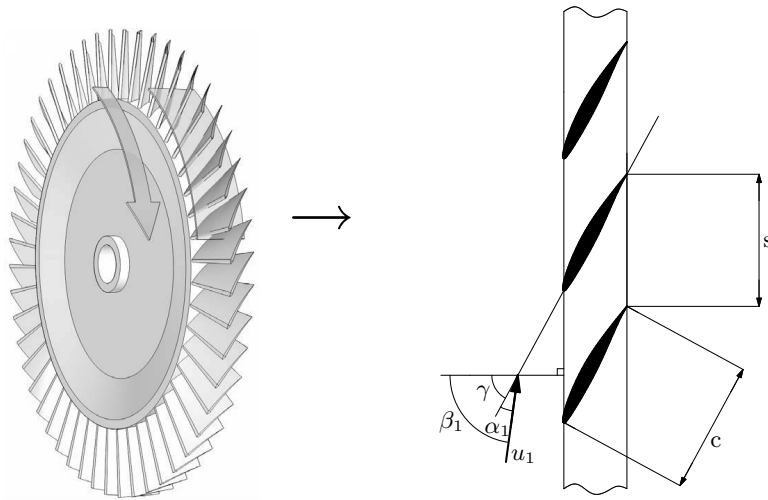


Figure 4.1. Axial impeller and cascade geometry [20].

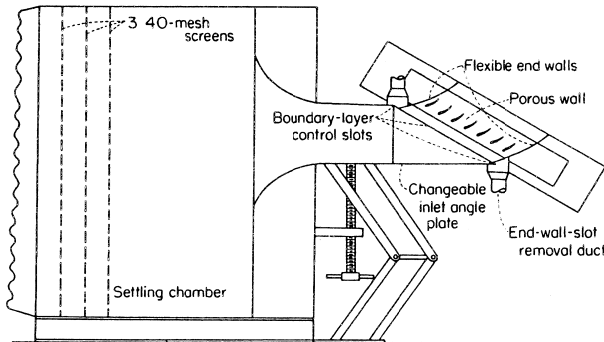


Figure 4.2. Vertical cross section of the experimental setup [12].

where p is the static pressure at the blade surface, p_1 is the static pressure far upstream of the blade, ρ is the fluid density and u_1 is its velocity far upstream. The blade pressure distribution was measured at midspan position of the central airfoil.

The components of the force on the blade perpendicular and parallel to the incoming velocity are the lift force F_l and drag force F_d respectively*. The lift and drag coefficients are defined as

$$C_l = \frac{2F_l}{\rho u_1^2 cb}, \quad C_d = \frac{2F_d}{\rho u_1^2 cb}, \quad (4.2)$$

*It is important to notice that in [12] the direction of the lift and drag force is not based on α_1 , but on the mean velocity angle $\alpha_m = (\alpha_1 + \alpha_2)/2$, where α_2 is the angle of the flow far downstream of the blade. In this thesis, these forces are converted to lift and drag forces based on the angle of attack. Use is made of the turning angle $\theta = \alpha_2 - \alpha_1$, which is also given in [12].

where b is the span of a blade. The forces on a blade were determined by integration of the pressure and momentum terms across a suitable control volume far from the blade. Therefore the flow discharge angle was measured one to three chords behind the blade in the flow direction at several points at the tunnel center line (midspan). The average value was taken, but the measurement points inside the wake were left out to get less scatter. The velocity far downstream was obtained from these measurements by using a momentum weighted average. This was found necessary to give consistent drag values. The upstream flow angle was measured approximately one chord upstream of the blade row. Flow angles were obtained using a claw-type yaw head and the null method.

Total pressure surveys were made with a non-integrating multitube rake, approximately one chord downstream of the blade trailing edge. Total pressure was measured as well in the settling chamber far upstream of the blade row. Static pressure was measured approximately one chord upstream of the blade row. Pressures were obtained by orifices with pressure leads to manometer boards.

From the many cascade configurations that were tested, the asymmetric compressor blades of the NACA 65-410 type with $\beta_1 = 70^\circ$ and $\sigma = 1$ was selected to use for validation. In the experiment, the stagger angle γ was varied from 69.5° to 53.5° , which caused the angle of attack α_1 to range from 0.5° to 16.5° . This series of measurements can be regarded as a model for an axial pump with variable blade angle at constant flow rate and shaft speed. The coordinates of the blade surface are given in Tab. A.1 of appendix A. The measured results for C_p are given in Fig. 4.10, while C_l and C_d are shown in figures 4.12 and 4.13 respectively. According to [12], the accuracy of the measured angles of attack is 0.5° for angles of attack near 6.5° .

4.2 Numerical model

The flow through the cascade is periodic in the direction of the blade row. Because of this, the flow around only one blade has to be modeled. A typical computational domain is given in Fig. 4.3, showing the topology of the 2D block-structured grid and the number of elements at each block face.

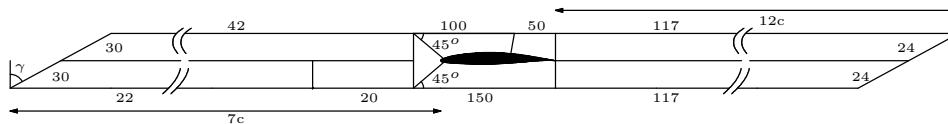


Figure 4.3. The block structure of the cascade, with number of elements for each block face.

the same grid is used. However, a separate grid has to be made for each stagger angle. Because DeFT can handle only one type of boundary condition per block face and because the two rows of virtual cells around each block must be continuous (section 2.1), a total number of 9 blocks is necessary. The grid close to the blade is plotted in Fig. 4.4. The total number of cells equals 16776. All internal block boundaries have matching grids. The block topology allows for a C-type grid around the blade, to ensure optimum mesh quality near the blade surface. In the simulations the chord

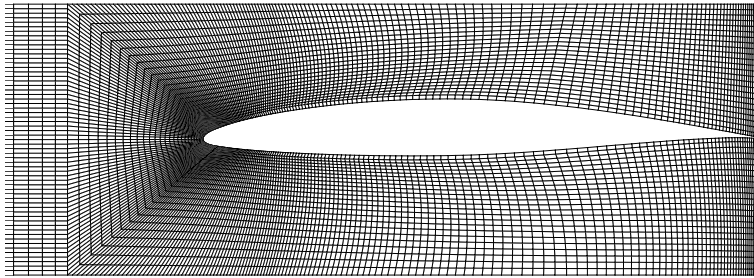


Figure 4.4. Grid close to the blade.

length is 1 m, the density is 1 kgm^{-3} , the upstream velocity is 1 ms^{-1} and the viscosity is $4.08 \cdot 10^{-6} \text{ Pa}\cdot\text{s}$, consistent with the Reynolds number of 245000.

In DeFT, as well as in Fluent, the incompressible Reynolds-Averaged Navier-Stokes (RANS) equations are solved on this domain using the standard $k - \epsilon$ turbulence model to calculate the Reynolds stresses. Log law wall functions are used to model the boundary layer at the blade. At the blade surface, a shear stress determined from this law and a zero normal velocity are prescribed. The value for y^* ranges between 15 and 55, with a relatively small part below 30 close to the leading and trailing edges. For the case of $\alpha_1 = 6.5^\circ$, y^* is shown in Fig. 4.5. The Fluent user

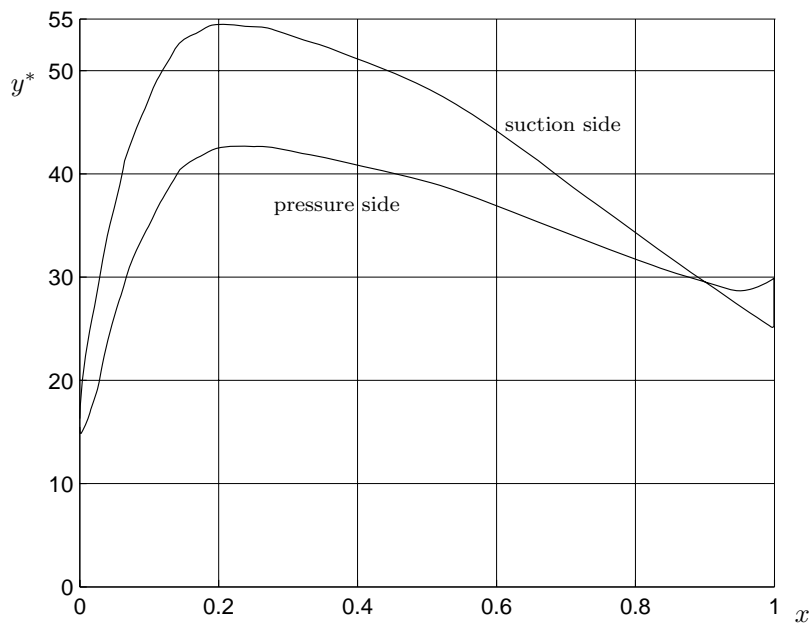


Figure 4.5. Distribution of y^* versus distance x from the leading edge along the blade chord, for $\alpha_1 = 6.5^\circ$ (DeFT).

guide recommends y^* to be between 30 and 300 for the wall functions to be valid.

At the inlet, the velocity is prescribed and k and ϵ are given values of $0 \text{ m}^2\text{s}^{-2}$ and $10^{-6} \text{ m}^2\text{s}^{-3}$ respectively. At the lower and upper boundaries of the domain a periodic boundary condition is prescribed. The grid at these boundaries is non-matching. At the outflow boundary on the right side of the domain, zero stress is prescribed in DeFT. For the turbulent quantities in DeFT and all flow variables in Fluent the gradient normal to the outflow boundary is set to zero. The initial conditions are equal to the boundary conditions at inflow. The initial pressure is equal to zero.

DeFT has an unsteady flow solver. Stationary flow solutions have to be found by calculating the flow in time until the flow becomes stationary. The time derivative of the velocity is discretized using the implicit first order Euler scheme. The time step equals 0.01 s when the first order upwind scheme is used for the discretization of the convective terms in the momentum equations. When the central differencing scheme is used for these terms, a time step of 0.001 s is used. For the first part of the calculations in DeFT, the upwind scheme was used. When a steady solution was obtained, the spatial discretization was changed to the central scheme to continue the calculation. For the turbulence equations a first-order upwind scheme is used. For each of the RANS equations the default value for the convergence criterion parameter ϵ_c was used (section 2.5).

In addition to an unsteady flow solver, Fluent also has a steady flow solver which is used to calculate the cascade flow. The Quadratic Upwind Interpolation for Convective Kinematics (QUICK) scheme is used for the discretization of the convective terms in the momentum equations. The pressure is interpolated to the face of a cell using the second order scheme. The turbulence equations are discretized with a first order upwind scheme. The value of the scaled residual necessary to reach convergence was set equal to 10^{-4} for the continuity equation. For the other equations this value was 10^{-3} . The definitions of the convergence criteria in DeFT and in Fluent are different. Besides that, the equations that are solved are different; in Fluent the stationary and in DeFT the time-dependent RANS equations. Therefore, in both Fluent and DeFT the convergence criteria were determined as to give approximately equal simulation results. All other parameter settings that Fluent 6.2.1.6 provides, have the default value.

In DeFT and in Fluent, calculation of the force on the blade is done by integration of the stresses on the surface. In Fig. 4.6 the local normal-tangential ($n-t$) coordinate system is drawn. The stress components of the fluid on the blade are written as

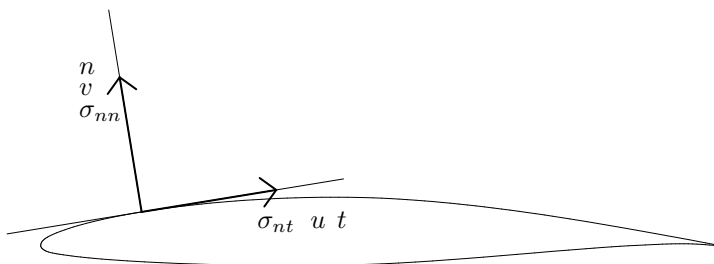


Figure 4.6. Surface stress on the blade.

$$\sigma_{nn} = -p + 2\mu \frac{\partial v}{\partial n}, \quad \sigma_{nt} = \mu \left(\frac{\partial u}{\partial n} + \frac{\partial v}{\partial t} \right), \quad (4.3)$$

where μ is the viscosity of the fluid. In each expression one term is equal to zero. Because the velocity on the surface of the blade is equal to zero, the derivative of the velocity in tangential direction is zero as well. Using this in the incompressible continuity equation

$$\frac{\partial u}{\partial t} + \frac{\partial v}{\partial n} = 0, \quad (4.4)$$

it turns out that

$$\frac{\partial v}{\partial n} = 0. \quad (4.5)$$

Therefore, the wall normal stress is determined by the pressure only. Since wall functions are used to prescribe the velocity profile near the blade, the actual wall shear stress

$$\tau_w = \mu \frac{\partial u}{\partial n} \quad (4.6)$$

is calculated using equations (2.21)-(2.24). It is subsequently integrated together with the pressure to find the total force on the blade.

The simulations in DeFT and Fluent are performed for various angles of attack. The results are presented in the next section.

4.3 Results and comparison with measurements

In this section the simulation results are introduced by a plot of the streamlines, the pressure contours and the turbulent viscosity contours. After this, the pressure distribution on the blade is given for several stagger angles. Finally, the lift and drag forces, the axial and tangential forces and the influence of pressure and shear stress on these forces are presented.

4.3.1 Flow field

Streamlines around the blade are given in Fig. 4.7. The turning of the flow by the

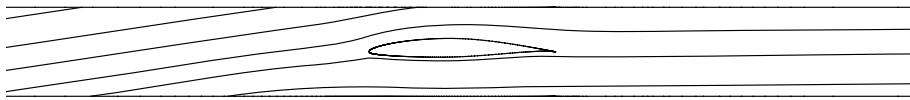


Figure 4.7. Streamlines for $\alpha_1 = 8.5^\circ$ and $\gamma = 61.5^\circ$ (Fluent).

cascade is clearly visible. A contour plot of the pressure is shown in Fig. 4.8. Due to the periodicity of the flow, the pressure distribution along the upper and lower domain edge is equal, but shifted in horizontal direction. A contour plot of the turbulent viscosity is given in Fig. 4.9. At the blade surface, the turbulent viscosity

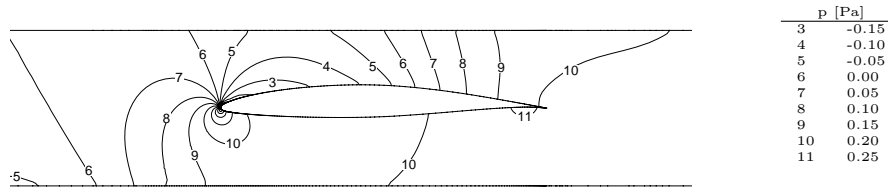


Figure 4.8. Pressure contours for $\alpha_1 = 8.5^\circ$ and $\gamma = 61.5^\circ$ (Fluent).

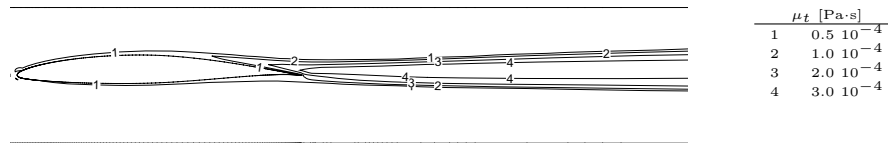


Figure 4.9. Contours of turbulent viscosity μ_t for $\alpha_1 = 8.5^\circ$ and $\gamma = 61.5^\circ$ (Fluent).

is much larger than the fluid viscosity $4.08 \cdot 10^{-6}$ Pa.s. The higher levels of turbulent viscosity are concentrated in the wake of the blade.

4.3.2 Blade surface pressure

The pressure at the blade is given by the distribution of C_p , for 6 angles of attack, in Fig. 4.10. Results from experiments [12] and numerical simulations of [4] are given as well. These numerical results are not available for the angle of attack equal to 6.5° and 16.5° . The CFD package Star-CD was used with a different mesh with 153 cells from leading to trailing edge and 54 cells between two blades. Note that the scale for C_p is not the same for the graphs in Fig. 4.10. For high Reynolds number flows, the largest value of C_p occurs at stagnation points, where $C_p = 1$. The results shown here are consistent with this theoretical maximum.

In the graph for $\alpha_1 = 16.5^\circ$ in Fig. 4.10, the experiments show that the pressure on the suction side of the blade is approximately constant along the rear part of the blade. This is often seen when there is an area of flow separation. In Fig. 4.11 streamlines near the trailing edge are plotted for this case. There is flow separation along 30% of the blade, but apparently it is not modeled accurately enough, because the CFD results do not show the constant pressure region.

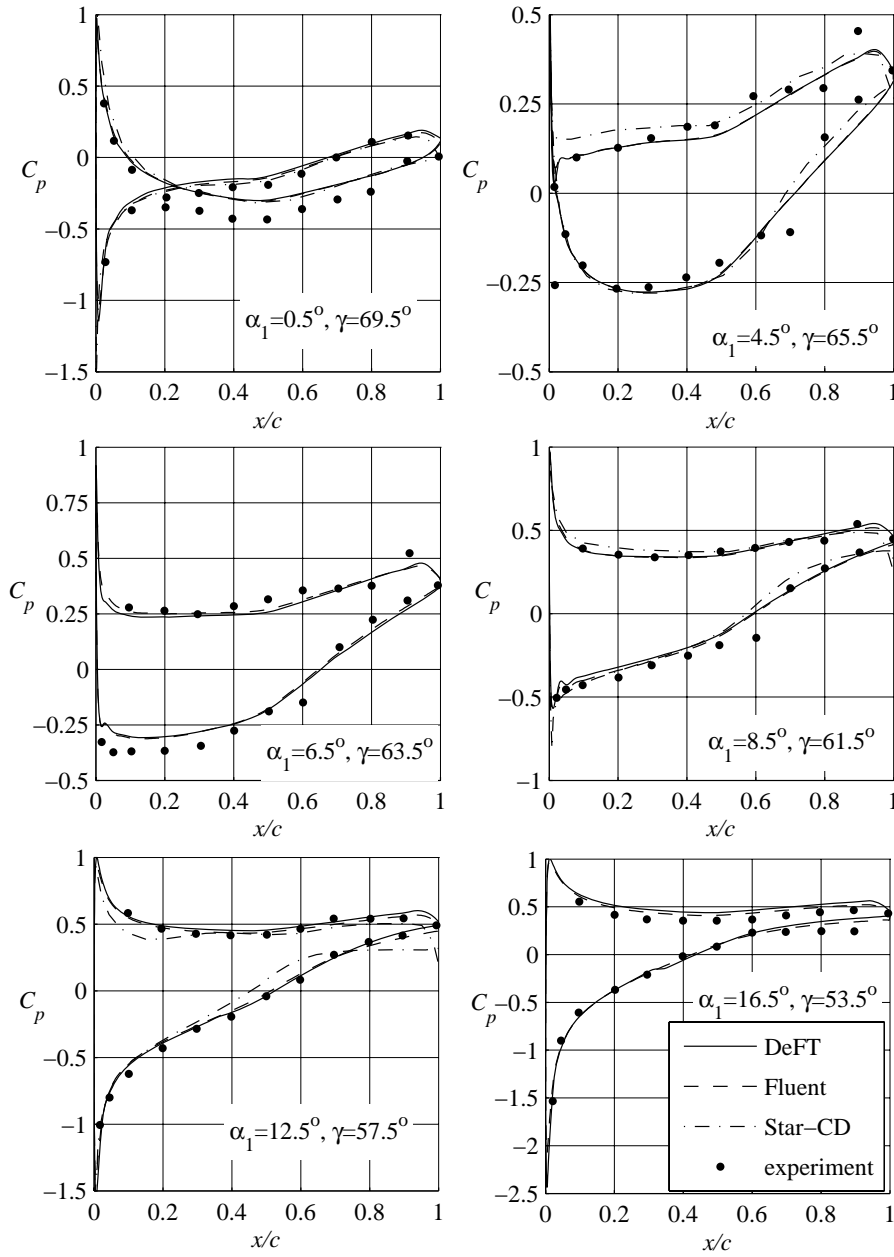


Figure 4.10. Pressure coefficient versus distance x/c from the leading edge along the blade chord, for different angles of attack.

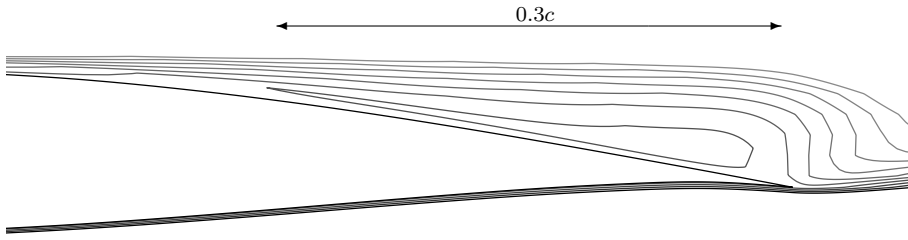


Figure 4.11. Streamlines near the trailing edge for $\alpha_1 = 16.5^\circ$ and $\gamma = 53.5^\circ$ (Fluent).

4.3.3 Lift and drag forces

The lift and drag coefficients are given in Fig. 4.12 and Fig. 4.13. The decreasing

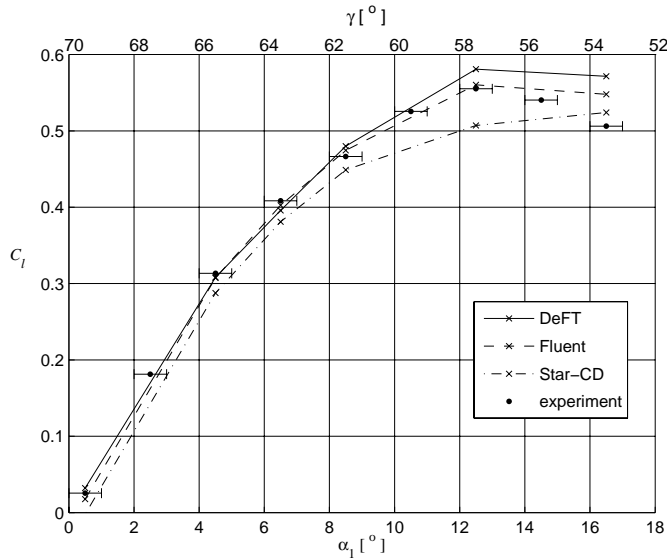


Figure 4.12. Lift coefficient as a function of angle of attack α_1 .

lift at $\alpha_1 = 16.5^\circ$ is predicted by DeFT as well as by Fluent. The horizontal error bars in both the lift and drag represent an uncertainty in α_1 of $\pm 0.5^\circ$. The vertical error bars, shown for the measured drag coefficients, represent the influence of this uncertainty on the drag force. Since the force on the blade is roughly perpendicular to the incoming flow direction for the larger angles of attack, a small uncertainty in α_1 results in a large relative error in the drag force, while the lift force is virtually unaffected. In Fig. 4.14 and Fig. 4.15, the relative error in the lift and drag prediction is shown. The error in the lift is defined as

$$E_{C_l} = \frac{C_l^{exp} - C_l^{cfd}}{C_l^{exp}} \quad (4.7)$$

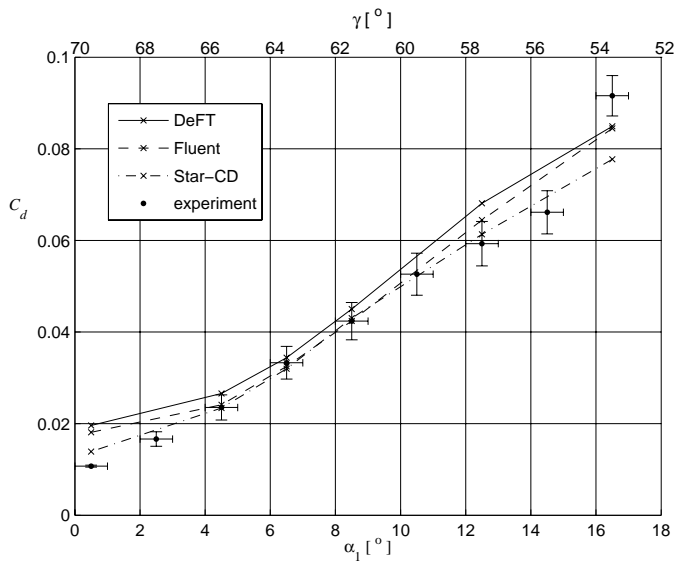


Figure 4.13. Drag coefficient as a function of angle of attack α_1 .

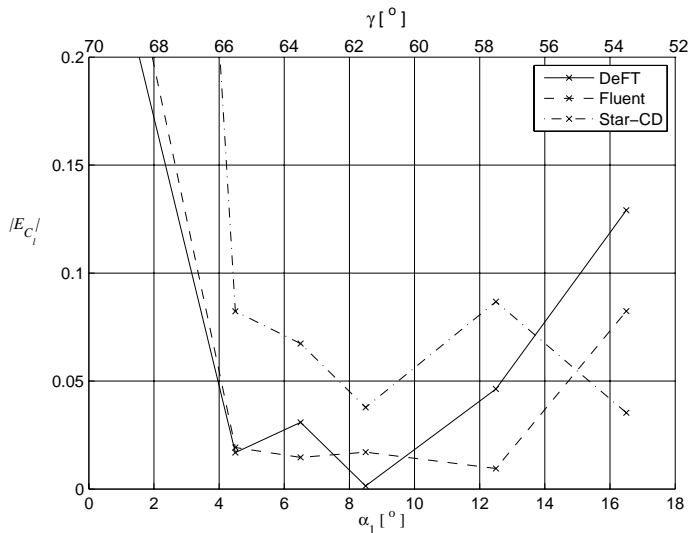


Figure 4.14. Error in lift coefficient as a function of angle of attack α_1 .

The error in the drag is defined analogously. For both the lift and the drag, the errors are large for small and large angles of attack. An important explanation for this is the increased complexity of the flow due to flow separation for the larger angles of attack. For the smaller angles of attack, the relative error in the lift is large, because the lift itself is small. For intermediate angles of attack, the errors in lift and drag are much smaller. In this region the CFD prediction of lift is good, while the prediction

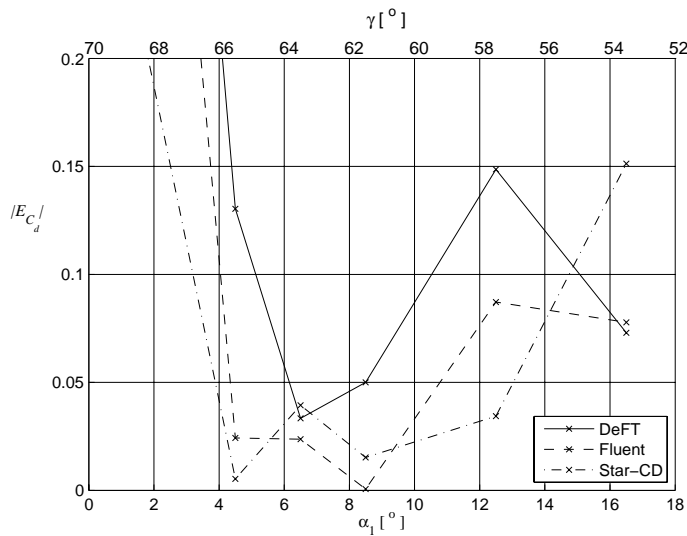


Figure 4.15. Error in drag coefficient as a function of angle of attack α_1 .

of drag is within the uncertainty range of the measurements.

In order to check the influence of the outflow boundary conditions on the solution, the domain was extended from approximately 12 to 21 chord lengths behind the trailing edge. A flow simulation was performed for $\alpha_1 = 8.5^\circ$ using Fluent. The differences in lift and drag coefficient were below 0.5%, which shows that the outflow boundary conditions have little influence on the flow close to the blade and the outflow boundary is sufficiently far away from the blade.

The grid dependency of the solution is also checked for a calculation at $\alpha_1 = 8.5^\circ$. Based on the topology and structure of the original grid, three additional grids were constructed: two coarser and one finer. The results for lift and drag on these grids are shown in Fig. 4.16 and Fig. 4.17 respectively. The average grid size h is determined from

$$h = \sqrt{\frac{A}{n}}, \quad (4.8)$$

where $A = 9.33 \text{ m}^2$ is the total area of the grid and n equals the total number of cells. Results show that grid convergence is reached on the original grid, since for both C_l and C_d the difference in its value on the original and the finest grid is below 1%.

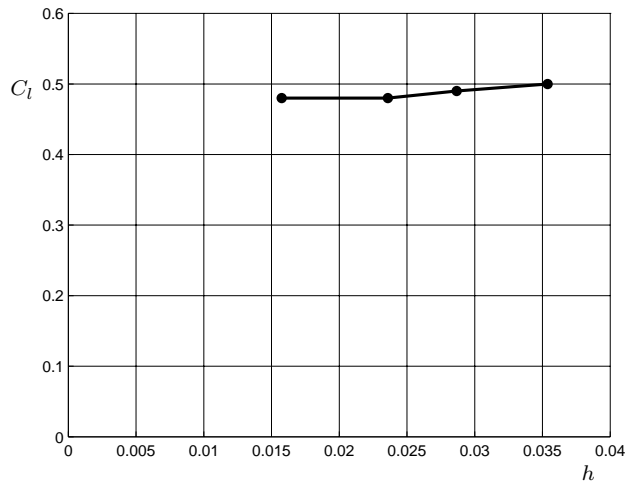


Figure 4.16. Lift coefficient as a function of average cell size h .

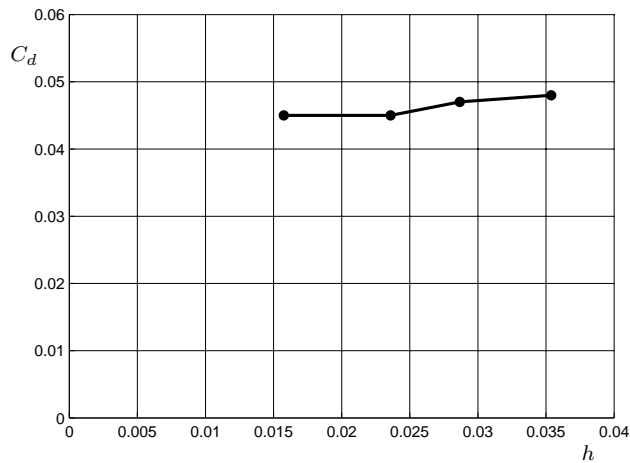


Figure 4.17. Drag coefficient as a function of average cell size h .

4.3.4 Axial and tangential forces

Instead of the lift and drag forces, the total force on the blade can also be decomposed into a tangential force in circumferential direction of the rotor and an axial force. These forces are more relevant for turbomachinery. The corresponding force coefficients can be determined from the lift and drag force by

$$C_t = C_l \cos \beta_1 + C_d \sin \beta_1, \quad C_a = C_l \sin \beta_1 - C_d \cos \beta_1. \quad (4.9)$$

Fig. 4.18 and Fig. 4.19 give C_t and C_a as a function of α_1 . These plots are for

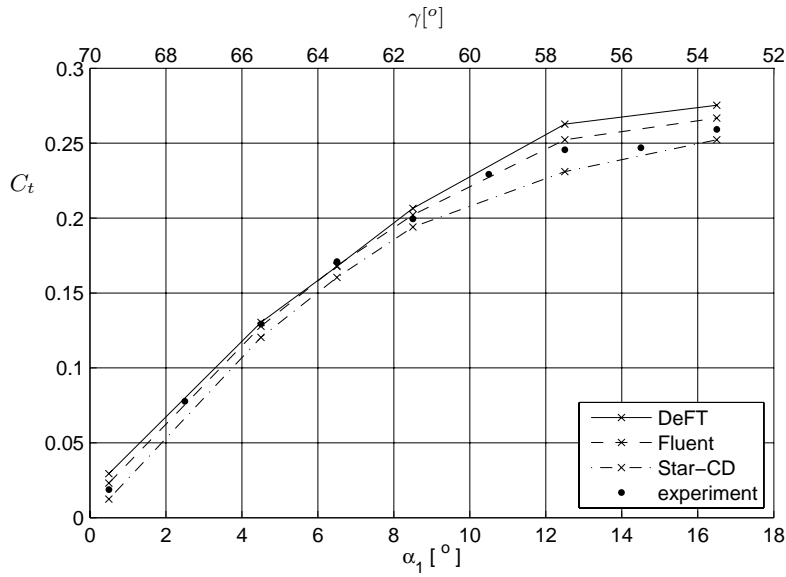


Figure 4.18. Tangential force coefficient as a function of angle of attack α_1 .

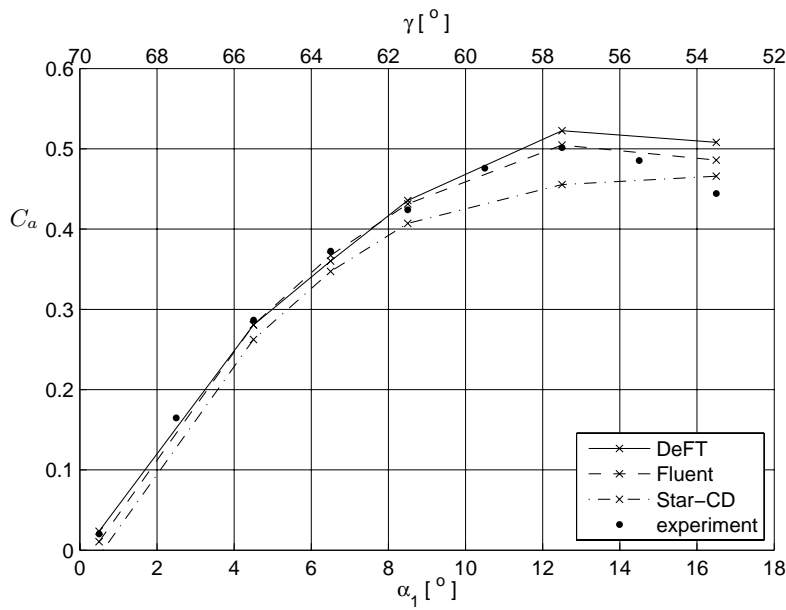


Figure 4.19. Axial force coefficient as a function of angle of attack α_1 .

varying stagger angle γ , but constant inlet angle β_1 . Each value of γ represents a different pump. The relation between inlet angle β_1 and the axial velocity u_a is given in Fig. 4.20 for a blade section at radius r and shaft speed Ω . The relative velocity u_1 is the incoming velocity with respect to the rotating frame of reference. It follows

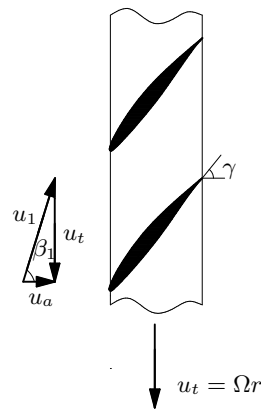


Figure 4.20. Axial component u_a and tangential component u_t of the velocity vector.

that, if β_1 and Ω are constant, also axial velocity - and thus flow rate - is constant. In Fig. 4.21 the axial force coefficient is given as a function of axial velocity for different stagger angles. The previous flow simulations are for different pumps (stagger angle),

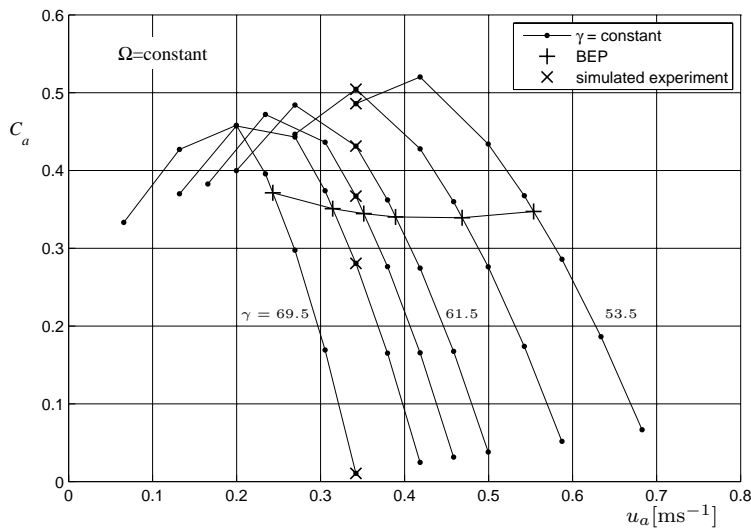


Figure 4.21. The axial force coefficient as a function of axial velocity for different stagger angles.

but all at the same axial velocity. To determine the Best Efficiency Point (BEP) for each of these pumps, additional simulations were performed with Fluent. For each stagger angle, the angle of attack was varied from 0 to 16.5 degrees, where u_t was kept constant for all pumps. The resulting force-velocity curves are given as well in Fig. 4.21. The ratio of axial and tangential forces for these pumps is shown in Fig. 4.22. Since this ratio is a measure of the efficiency of the pump, it is concluded that

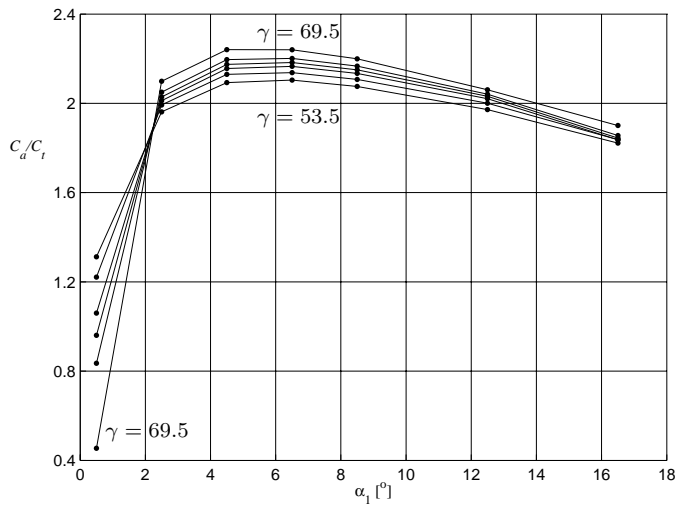


Figure 4.22. The axial to tangential force ratio for stagger angles from 53.5° to 69.5° as a function of angle of attack.

the BEP condition corresponds to an angle of attack α_1 of approximately 6° for all pumps considered. For each curve, the BEP condition is given in Fig. 4.21. The curves of Fig. 4.21 are also plotted in Fig. 4.23, where they are scaled with the values of the axial force and velocity at BEP. Since the inlet angle at BEP can be written

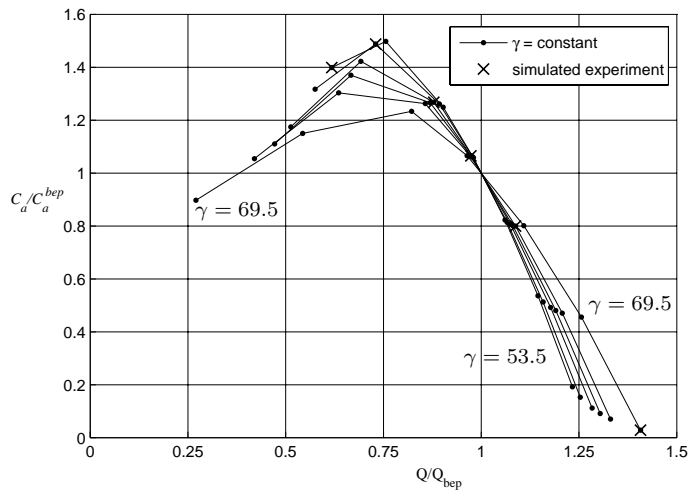


Figure 4.23. The scaled axial force coefficient as a function of the scaled flow rate for different stagger angles.

as $\beta_1^{bep} = \gamma + \alpha_1^{bep}$, the deviation from Q_{bep} for each pump is equal to

$$\frac{Q}{Q_{bep}} = \frac{\tan(\gamma + \alpha_1^{bep})}{\tan(\beta_1)}. \quad (4.10)$$

Note that Fig. 4.23 corresponds to graphs known as head characteristics that are frequently used in turbomachinery applications. With Eq. (4.10) the tangential and axial force coefficients are given as a function of Q/Q_{bep} in Fig. 4.24 and Fig. 4.25 respectively.

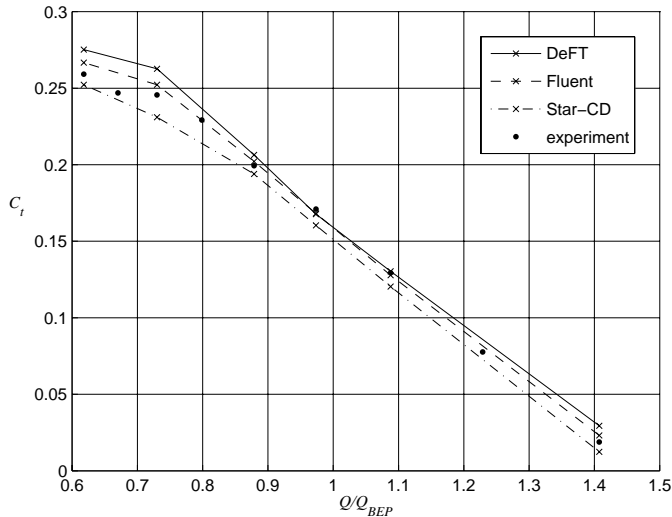


Figure 4.24. Tangential force coefficient versus the deviation from BEP.

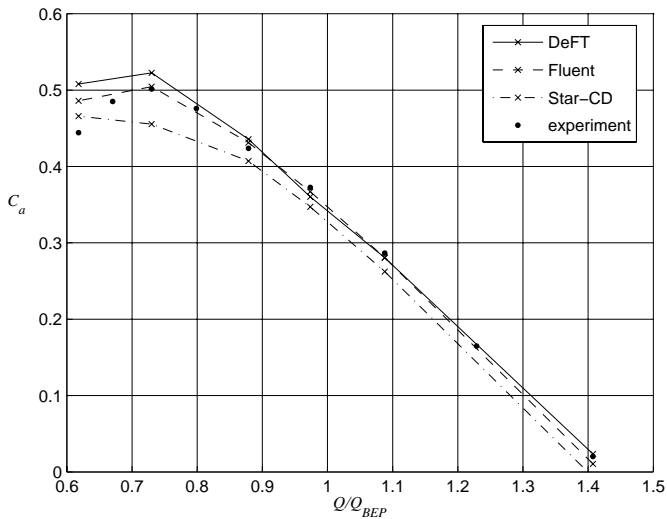


Figure 4.25. Axial force coefficient versus the deviation from BEP.

The relative error in the CFD results for the tangential force is defined as

$$E_{C_t} = \frac{C_t^{exp} - C_t^{cfd}}{C_{t,bep}^{exp}}, \quad (4.11)$$

where the absolute error is normalized by its value at BEP. The error for the axial force coefficient is defined analogously. Both are given as a function of Q/Q_{bep} in Fig. 4.26 and Fig. 4.27. For flow rates between approximately $0.8Q_{bep}$ and (at least)

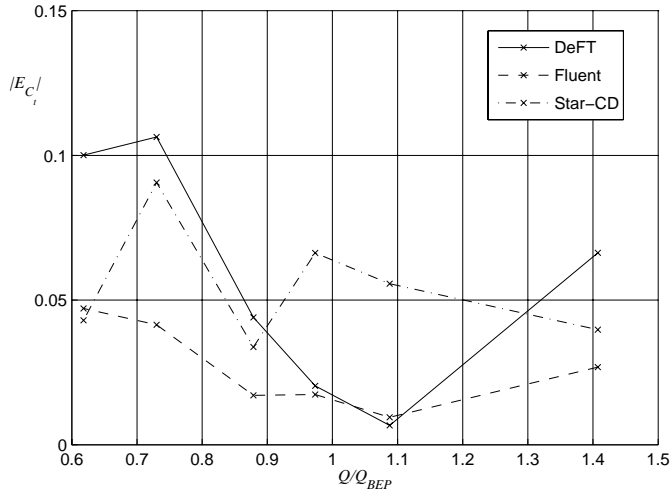


Figure 4.26. Tangential force error versus the deviation from BEP.

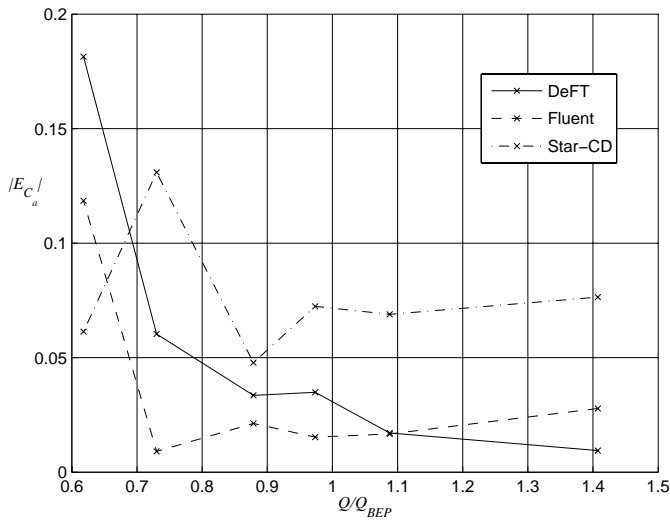


Figure 4.27. Axial force error versus the deviation from BEP.

$1.4Q_{bep}$ the errors are only a few percent. This is why it is expected that CFD can be used to model the flow through a turbomachine when it operates in this range of flow rates. At lower flow rates the error becomes larger, probably due to flow separation and the difficulty of the CFD model to accurately capture this.

4.3.5 Pressure and shear stress forces

The contribution of the shear stress to the lift, drag, axial and tangential forces, is shown in Fig. 4.28. Both the direction and the relative magnitude of the forces

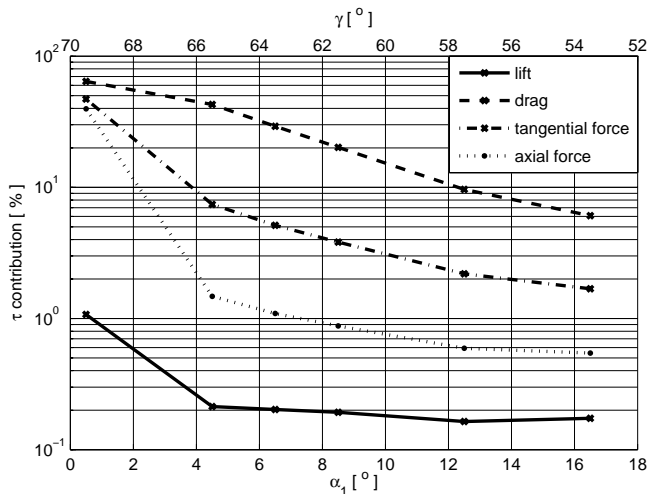


Figure 4.28. Contribution of shear stress to different force components on the blade (Fluent).

due to pressure and shear stress play an important role in the explanation of their influence. They are plotted in Fig. 4.29 and Fig. 4.30. The lift force is dominated by the pressure for all angles of attack, because the force due to pressure is close to perpendicular to the direction of the incoming flow, while the force due to shear stress is almost parallel to the incoming flow. Another reason is that the pressure force is much larger than the force due to shear stress for angles of attack not close to zero. For a small angle of attack, the pressure force is comparable to the shear stress force. The pressure contribution is always dominant, also for drag calculation (except for $\alpha_1 = 0.5^\circ$). The shear stress is not important for the lift force, and for the larger angles of attack its influence on the axial and tangential force is less than 10%. In Fig. 4.31 and Fig. 4.32 the pressure force vector \underline{C}_p and the shear stress force vector \underline{C}_τ are plotted for all considered angles of attack. The total force vector on the blade calculated from the measurement results \underline{C}_{exp} is drawn as well. The forces are scaled to coefficients in the same way as the lift and drag forces. The horizontal axis is parallel to the blade chord. For all cases and certainly for the smaller angles of attack, \underline{C}_τ is nearly parallel to the blade chord. This can also be concluded from Fig. 4.29. Because most of the blade surface is nearly parallel to the chord, this

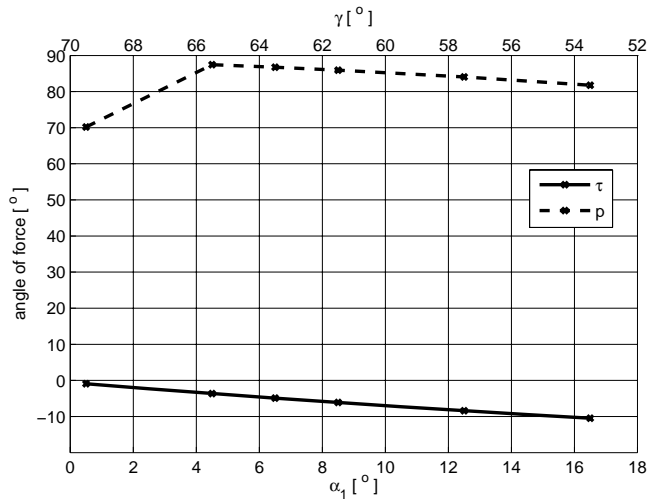


Figure 4.29. The angle, with respect to the direction of the incoming flow, of the forces due to pressure and shear stress (Fluent).

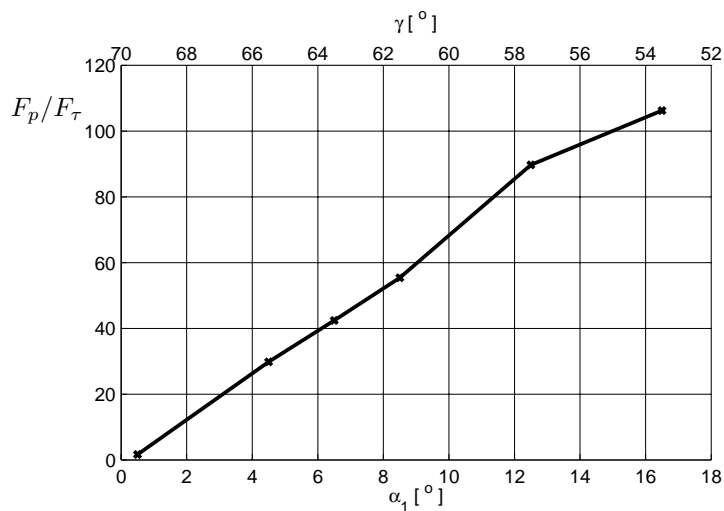


Figure 4.30. The pressure to shear stress force ratio (Fluent).

seems plausible. According to Fig. 4.31 and Fig. 4.32, when the shear stress force can not deviate a lot from the horizontal direction, the error in the total force of the CFD calculations seems to be caused mainly by an error in the length of the pressure force, for all cases except $\alpha_1 = 0.5^\circ$. This statement can not be proven, because the CFD results for pressure and shear stress both have errors which are not quantified. However, for $\alpha_1 = 0.5^\circ$ the total pressure force of the CFD calculations is certainly erroneous according to Fig. 4.10.

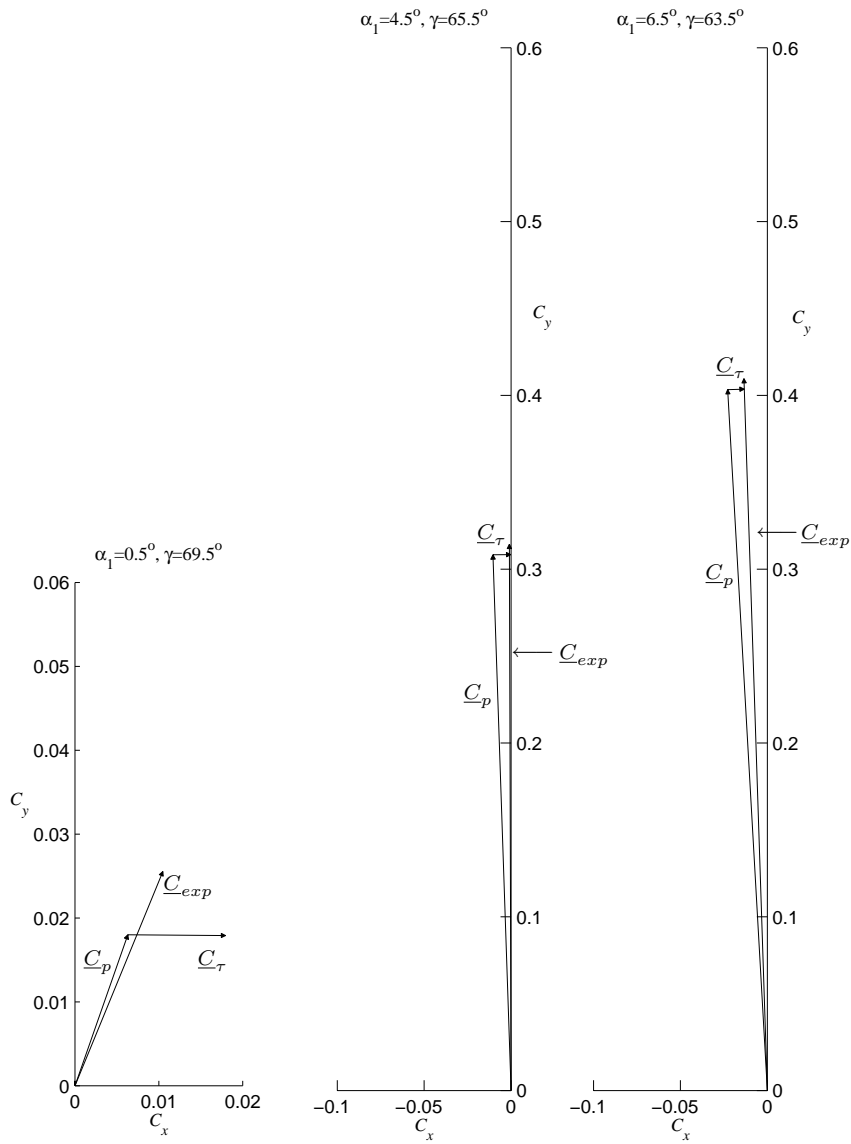


Figure 4.31. The pressure and shear stress force vectors of the Fluent calculation and the total force vector of the experiment.

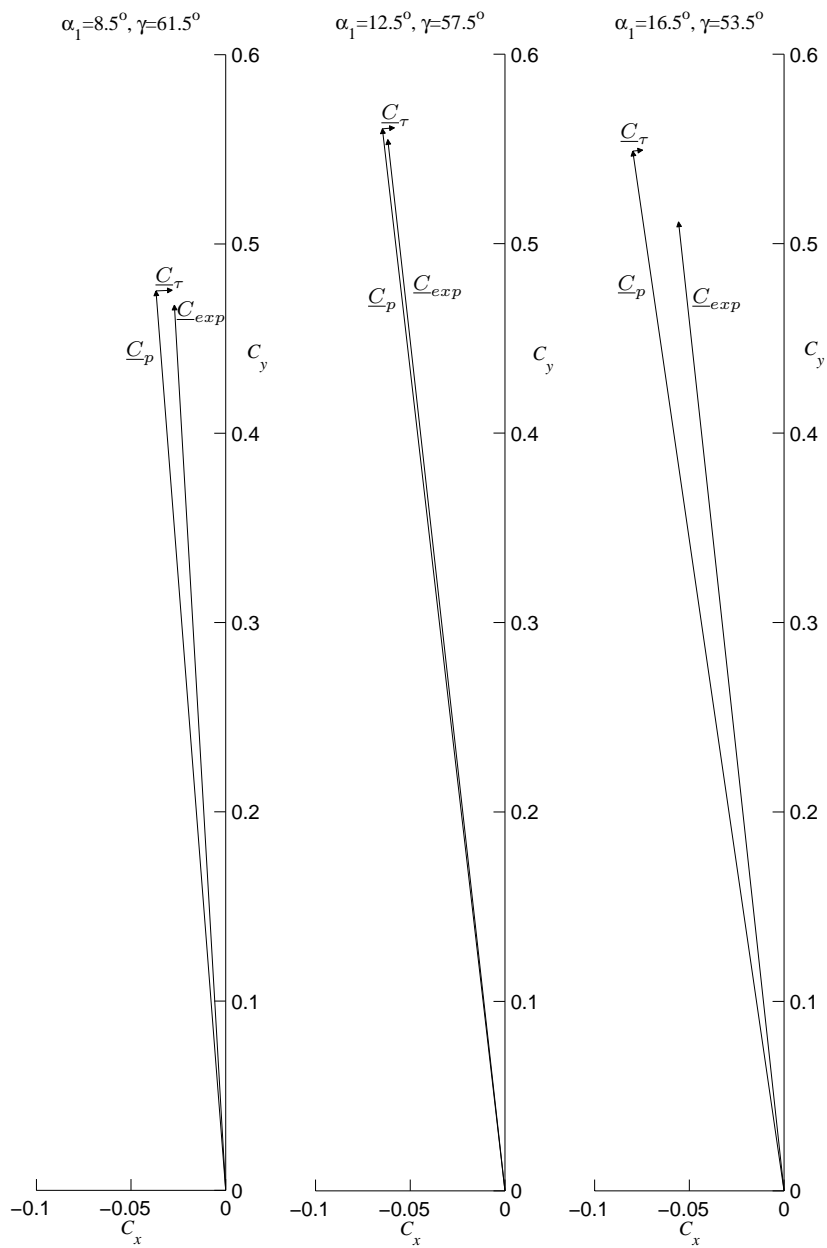


Figure 4.32. The pressure and shear stress force vectors of the Fluent calculation and the total force vector of the experiment.

4.4 Summary

An axial pump is modeled by a cascade of blades. For the inlet angle equal to 70° the turbulent flow through several pumps, each with a different stagger angle, is simulated with DeFT and Fluent. The calculated blade surface pressure is compared with results from experiments and CFD, both available in literature. For most cases there is good agreement between the results. Lift and drag forces are calculated as well. The agreement between results from CFD and experiments is good for an angle of attack between 4° and 10° .

To determine the Best Efficiency Point (BEP) for each pump, additional simulations were done with varying inlet angle. It turned out that for all pumps the BEP corresponds with an angle of attack equal to 6° .

The force on the blade is also decomposed into axial and tangential components, which are a measure for the head and the torque of the pump. These forces are plotted as a function of the deviation of the flow rate from BEP condition. For flow rates from $0.8Q_{bep}$ to $1.4Q_{bep}$ the errors are only a few percent. That is why it is expected that CFD can be used to model the flow through a turbomachine when it operates in this range of flow rates. At lower flow rates the errors are larger, probably due to flow separation.

Chapter 5

Unsteady flow in a pump

One of the goals of this thesis is to show that the flow through a pump can be calculated on a staggered grid. This is done in the current chapter for an unsteady incompressible flow through a two-dimensional centrifugal pump with a vaned diffuser. The flow simulations are performed with DeFT, on a staggered grid, but also using Fluent, on a collocated grid. The calculated time-averaged radial and tangential velocity and pressure along the pitch of a rotor channel are compared with results from experiments and other CFD simulations obtained from literature. The calculation times of DeFT and Fluent are compared as well in order to draw conclusions about the performance of both solvers.

5.1 Centrifugal pump and measurements

The centrifugal pump that is used to validate the simulation results is of radial type, with a vaned diffuser. It was tested experimentally in [27]. The main reason for choosing this case is the present version of DeFT being limited to 2D. In good approximation, the geometry of this pump is two-dimensional as well, except for the inlet region, see Fig. 5.1. Another reason is that results of CFD simulations are available in literature ([7], [18] and [26]). The geometrical data of the pump is given in Tab. 5.1.

	rotor			stator		
number of blades	z	7	-	z	12	-
inlet radius	r_1	120	mm	r_3	222	mm
outlet radius	r_2	210	mm	r_4	332	mm
blade span	b	40	mm	b	40	mm
chord length	c	222	mm	c	294	mm
tip clearance	δ	0.4	mm			

Table 5.1. Geometrical data

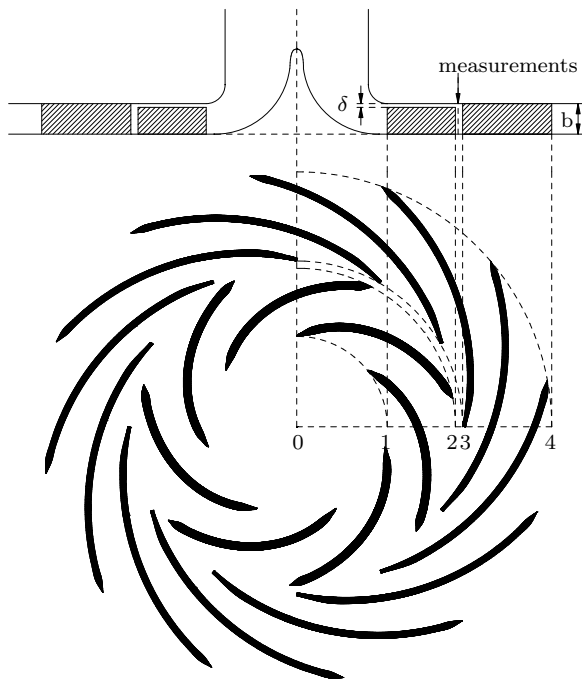


Figure 5.1. Geometry of the pump.

In an open circuit air is fed to the pump via an axial pipe and driven back into the surroundings shortly after it leaves the stator vanes. The operating conditions are given in Tab. 5.2. The gravitational acceleration equals $g = 9.83 \text{ ms}^{-2}$. The total pressure is defined as the sum of the static pressure and the kinetic energy density of the flow

$$p_t = p + \frac{1}{2}\rho u^2. \quad (5.1)$$

A constant-temperature anemometer with single sensor probes was used to measure the unsteady 3D velocity at mid-span at the impeller outlet. A flush mounted miniature fast response pressure transducer was used to measure the unsteady static pressure at the front cover of the unshrouded impeller. Velocity and pressure were measured at different circumferential positions at a constant radius of 214 mm, in the clearance gap between the rotor and stator. For each of the 30 positions across a stator passage 160 measurements were done at a rate of 18.7 kHz covering two rotor channel passages. This was repeated 700 times to be able to ensemble average the measured quantities. Velocity and pressure are also averaged over the 30 stator positions to get the time-averaged flow in a rotor passage. The normalized time-averaged radial velocity, relative tangential velocity and static pressure coefficient are presented in Fig. 5.16.

shaft speed	Ω	2000	rpm
flow coefficient	$\phi = \frac{Q}{\pi r_2^2 U_2}$	0.048	-
flow rate	Q	0.29	m^3s^{-1}
total pressure coefficient	$\psi = 2 \frac{p_{t4} - p_{t0}}{\rho U_2^2}$	0.65	-
head	$H = \frac{p_{t4} - p_{t0}}{\rho g}$	64.0	m
specific speed coefficient	$n_\omega = \frac{\Omega Q^{1/2}}{(gH)^{3/4}}$	0.90	-
Reynolds number	$Re = \frac{\rho c U_2}{\mu}$	$6.5 \cdot 10^5$	-
fluid density	ρ	1.2	kgm^{-3}
fluid viscosity	μ	$1.80 \cdot 10^{-5}$	Pa·s
tip velocity	$U_2 = \Omega r_2$	44	ms^{-1}

Table 5.2. Operating conditions, where the numbers in the subscripts refer to the radial positions shown in Fig. 5.1

5.2 Numerical model

Since DeFT can handle only one type of boundary condition on each block face, a large number of blocks is required for this particular pump. Fig. 5.2 shows part of the 126 blocks. A detail of the mesh is plotted in Fig. 5.3. The number of grid cells

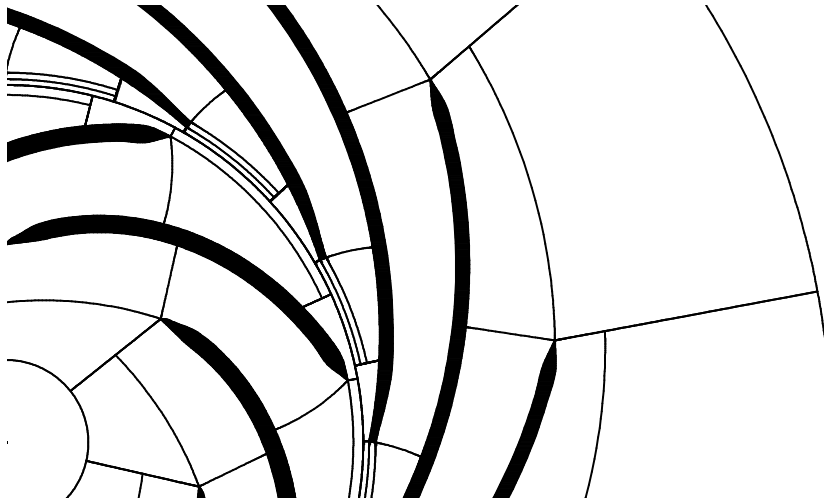


Figure 5.2. Block structure of the pump.

in a rotor and a stator channel are 3920 and 7032 respectively. The total number of cells cumulates to well over 110,000. The inlet and outlet radius of the domain are 50 and 500 mm respectively. The value of y^+ in the centroid of the wall-adjacent cells ranges from 2 to 40. Due to the boundary layers at the hub and the casing, the radial velocity at mid-span is larger than the span-averaged radial velocity. Because

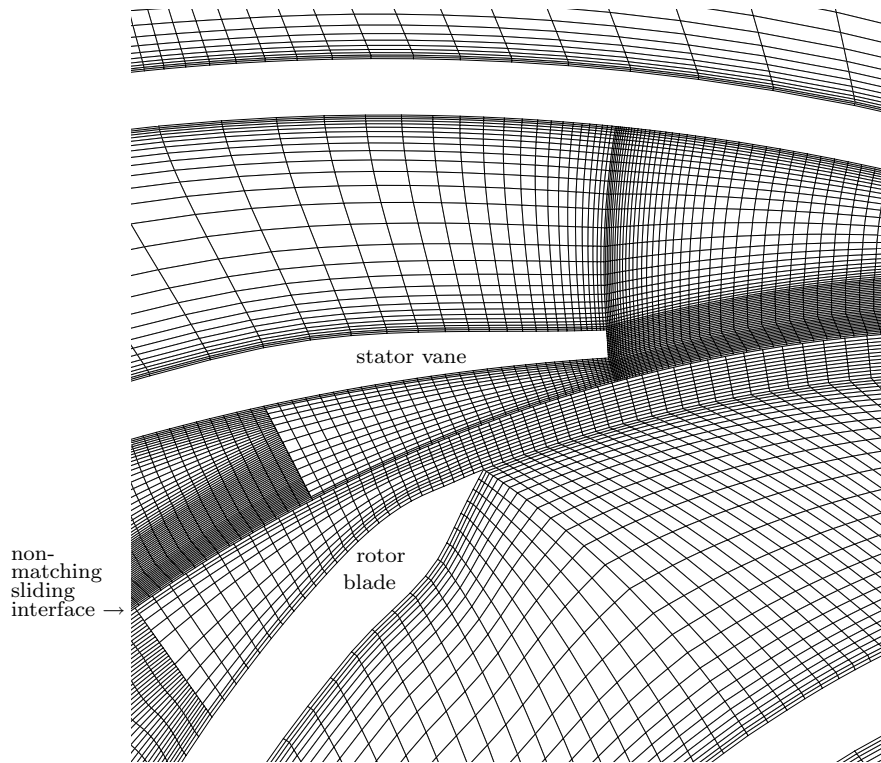


Figure 5.3. Close-up of the mesh near the sliding interface.

this displacement effect of the flow is not modeled in 2D, the flow rate used in the simulations is increased by 14% from 0.29 to $0.33 \text{ m}^3\text{s}^{-1}$. This new flow rate is determined through integration of the measured radial velocity at mid-span in [27]. At the inlet the corresponding radial velocity is prescribed together with $k = 1 \text{ m}^2\text{s}^{-2}$ and $\epsilon = 10 \text{ m}^2\text{s}^{-3}$ which corresponds to a turbulence intensity of 3.8% of the inflow velocity and a length scale of 16 mm. Wall-functions are prescribed at all blade surfaces. At the outlet of the domain a zero stress is prescribed in DeFT. For the turbulent quantities in DeFT and all flow variables in Fluent the gradient normal to the outflow boundary is set to zero. For the velocity and pressure zero initial values are prescribed, while k and ϵ are initialized with their values at the inflow boundary. For temporal discretization the first-order Euler scheme is used with a constant time step of $2 \cdot 10^{-5} \text{ s}$, which results in 1500 time steps per revolution. The residual that has to be reached for convergence is set to 10^{-4} for all equations in Fluent. In DeFT the residual for the pressure equation has to be less than $4.5 \cdot 10^{-4}$ to reach convergence. For the other equations the residual has to drop 4 orders of magnitude to reach convergence. The pressure equation in DeFT is solved for p^{n+1} (section 2.6). The above described simulation model is used in both DeFT and Fluent. There are,

however, some important differences between Fluent and DeFT. Fluent uses a multi-grid method and has an unstructured solver, while DeFT uses a block-structured GMRES solver.

5.3 Flow field

In this section the flow in the pump is presented. For the flow rate of $0.33 \text{ m}^3\text{s}^{-1}$ the contours of the total pressure p_t of the flow through the pump are given at a certain rotor position in Fig. 5.4. Due to the kinetic energy transfer from the rotor to the

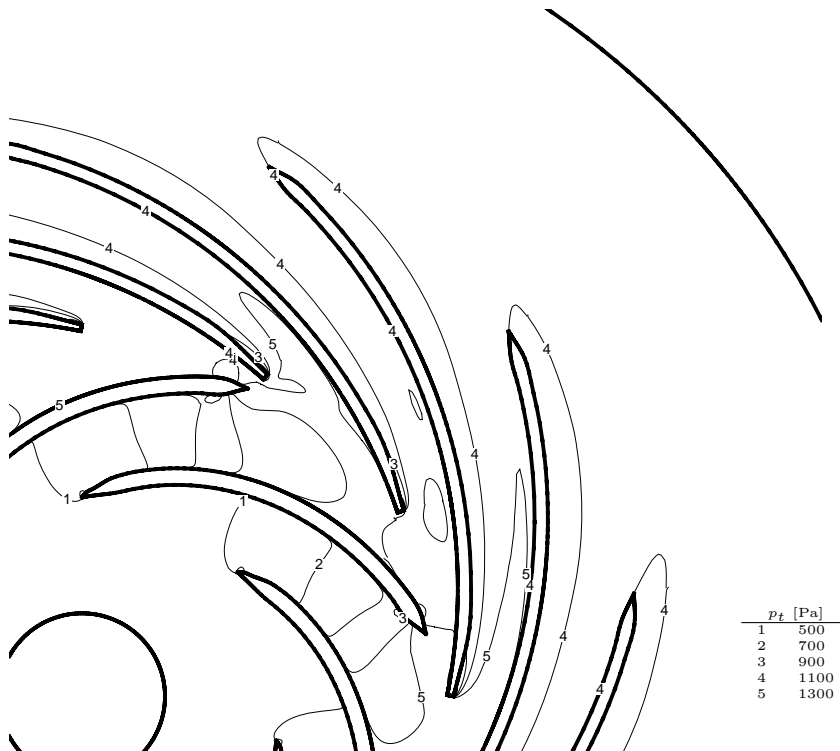


Figure 5.4. Contours of the total pressure p_t of the flow through the pump.

fluid, the total pressure increases from the inflow of the pump towards the outflow region of the rotor. As a result of losses in the flow, the total pressure then decreases slightly in the stator.

In Fig. 5.5 it is shown that the static pressure increases in the stator as well, because of the deceleration of the flow resulting in a conversion of kinetic energy to pressure.

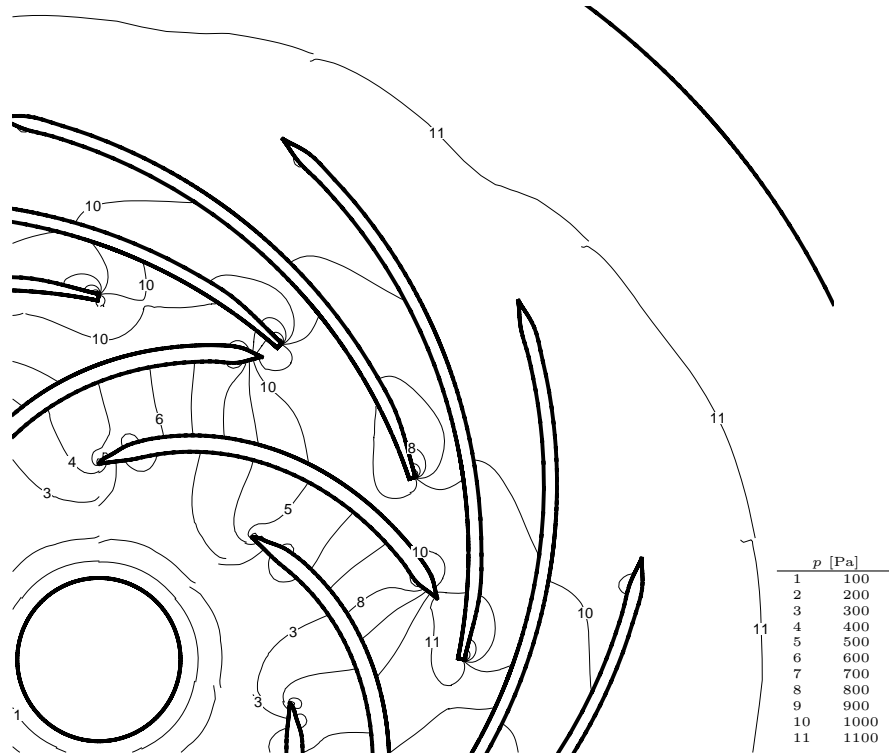


Figure 5.5. Contours of the static pressure p of the flow through the pump.

For the same flow rate and rotor position, the absolute and relative velocity vectors are given in Fig. 5.6 and Fig. 5.7 respectively. The relative velocity vectors smoothly

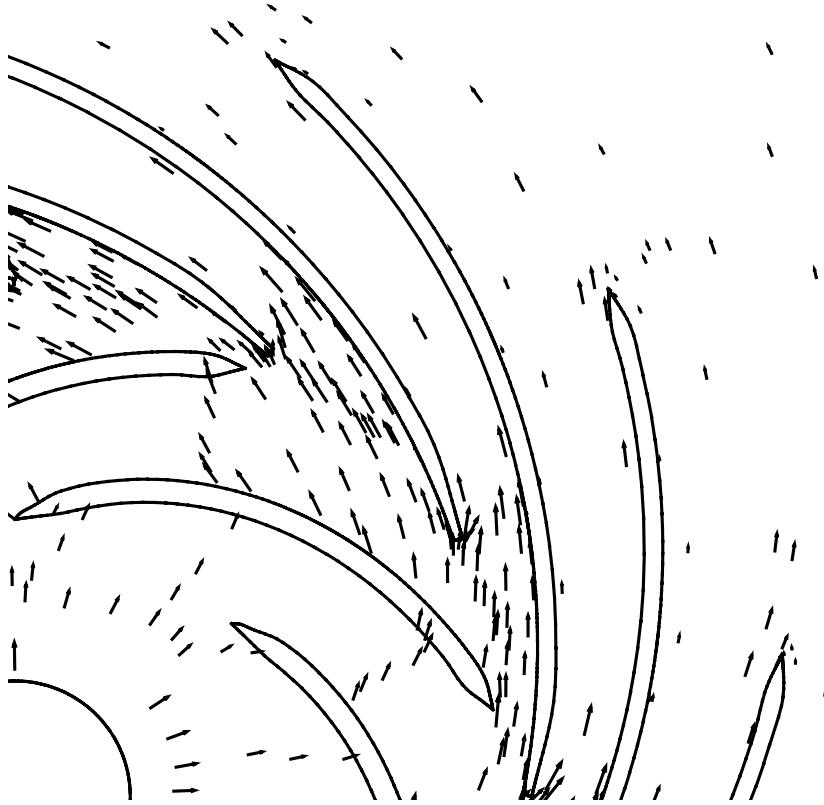


Figure 5.6. The absolute velocity vectors of the flow through the pump.

approach the leading edges of the rotor blades. Instead of smoothly approaching the leading edges of the stator vanes, the absolute flow seems to enter at a small incidence angle. In order to have a more precise view on the direction of the flow that approaches the stator vanes and its relation to the flow rate, simulations at several flow rates were done at constant shaft speed. The flow rate of $0.33 \text{ m}^3\text{s}^{-1}$ is changed in steps of 10% from 50% to 120%. For these cases the head of the pump H , defined in Tab. 5.2, is given as a function of the flow rate in Fig. 5.8.

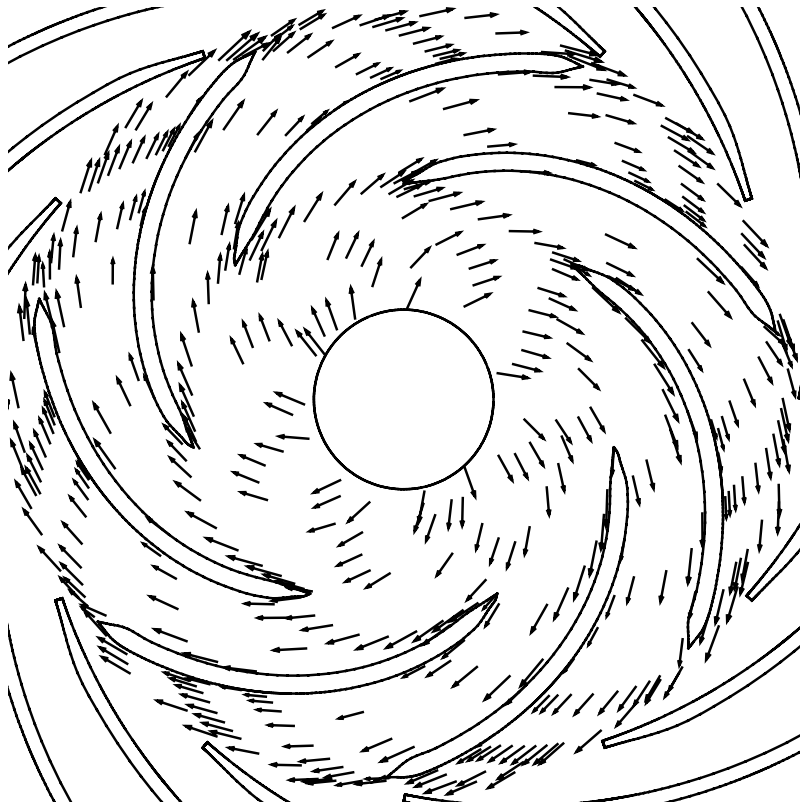


Figure 5.7. The relative velocity vectors of the flow through the rotor.

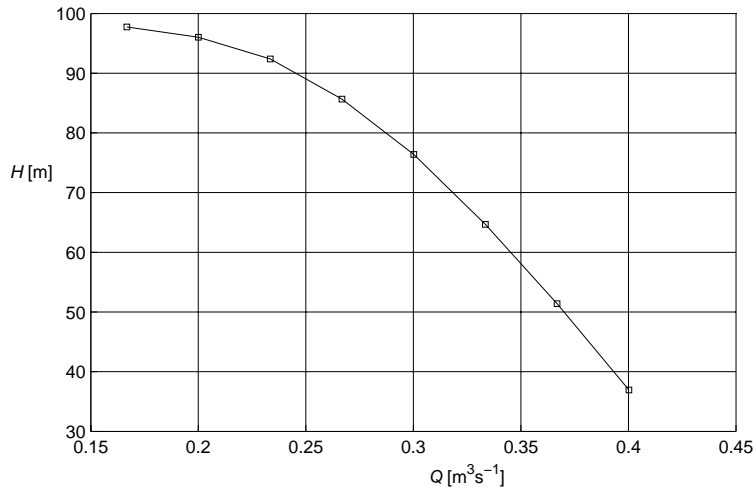


Figure 5.8. The head characteristic of the pump.

To calculate the head, the total pressure p_t is mass-averaged at the outflow and at the inflow surface. The loss of total pressure between the inflow surface of the numerical flow domain and the inlet of the axial pipe of the experimental setup is neglected. Conservation of total pressure is also assumed for the region between the stator outlet and the outflow surface of the numerical domain. To determine the best efficiency point (BEP) of the pump, its efficiency η is calculated by

$$\eta = \frac{Q(p_{t4} - p_{t0})}{\Omega T}, \quad (5.2)$$

where T is the shaft torque. Both the shaft torque and total pressure difference is calculated for one rotor position. Because the number of rotor blades and stator vanes is large, it is assumed that these integrated quantities don't deviate much from the average over all possible rotor positions. The efficiency of the pump is shown as a function of flow rate in Fig. 5.9. The BEP is at a flow rate of approximately 0.27

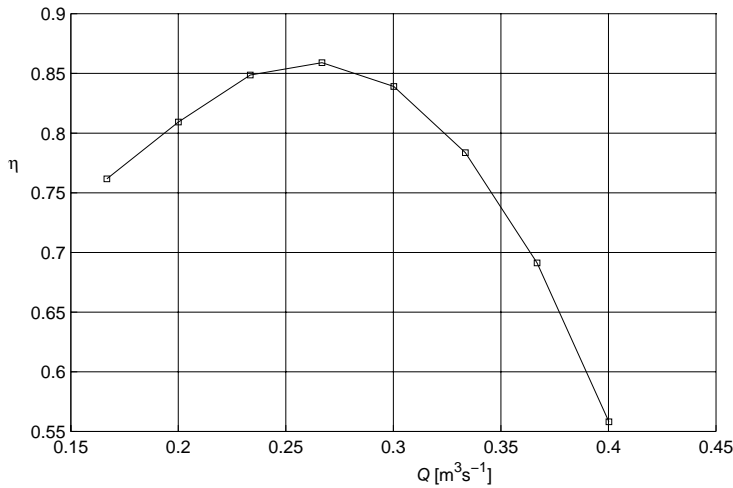


Figure 5.9. The efficiency of the pump versus the flow rate.

m^3s^{-1} , which is close to the flow rate used in the experiments, see Tab. 5.2. This suggests that the pump design is based on a uniform velocity profile between the hub and the casing. The influence of the blockage effect by the boundary layers is not taken into account.

The calculated total pressure coefficient $\psi = 0.657$ at $Q = 0.33 \text{ m}^3\text{s}^{-1}$ is very close to the value calculated from the experiments which is given in [27] and in Tab. 5.2. The streamlines of the flow around the leading edge of a stator vane are shown in Fig. 5.10 for the flow at $Q = 0.75Q_{BEP}$, in Fig. 5.11 for the flow at $Q = Q_{BEP}$ and in Fig. 5.12 for the flow at $Q = 1.25Q_{BEP}$. These streamlines are determined for the flow corresponding to the rotor location shown. The flow approaches the leading edge of the stator vane smoothly at BEP. At the flow rate below Q_{BEP} , the flow direction is more towards the rotor side of the stator vane. At the flow rate above Q_{BEP} , the flow direction is more towards the stator channel above the stator vane.

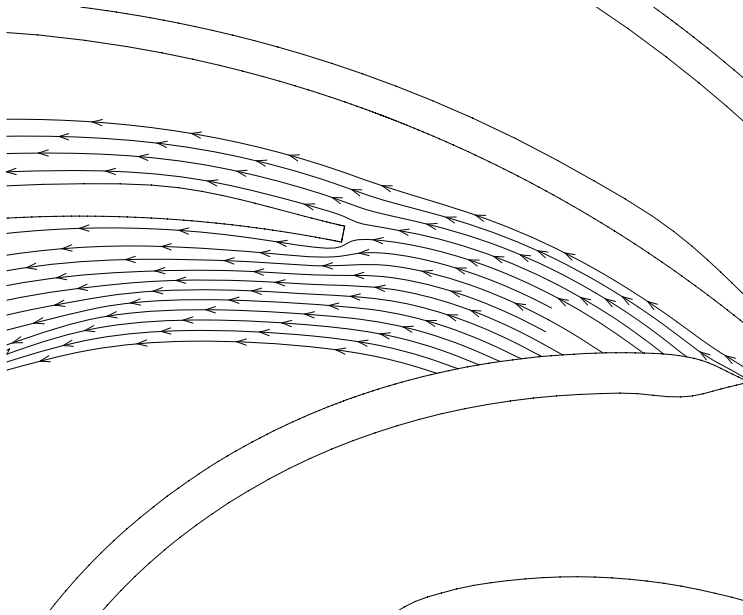


Figure 5.10. Streamtraces for the flow at $Q = 0.75Q_{BEP}$.

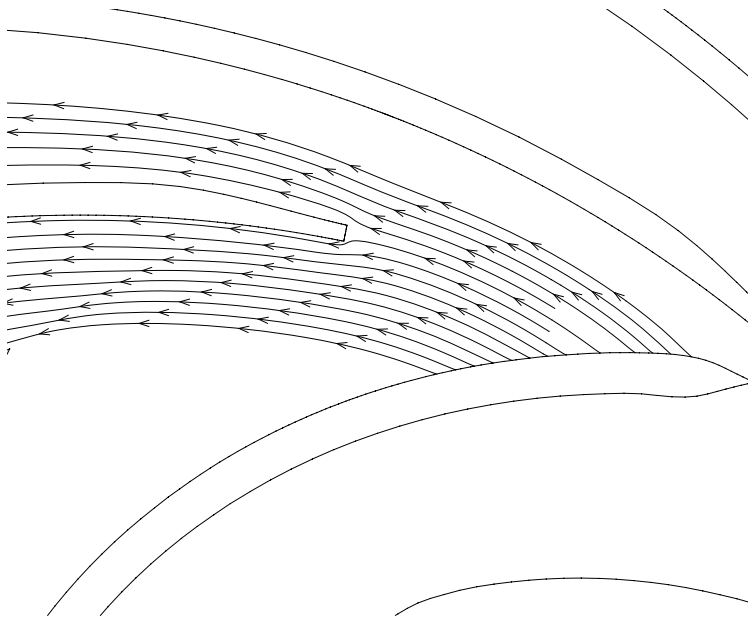


Figure 5.11. Streamtraces for a flow at $Q = Q_{BEP}$.

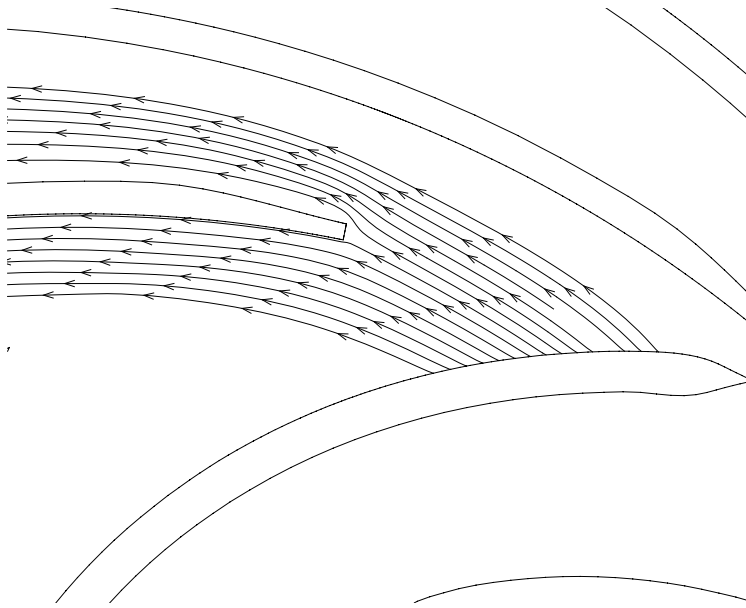


Figure 5.12. Streamtraces for a flow at $Q = 1.25Q_{BEP}$.

The pressure fluctuations in the area between the rotor and the stator play an important role in noise production of a pump. Therefore the static pressure is calculated as a function of time in two points. The location of point A close to the leading edge of a stator vane and point B in the middle of a stator channel is shown in Fig. 5.13.

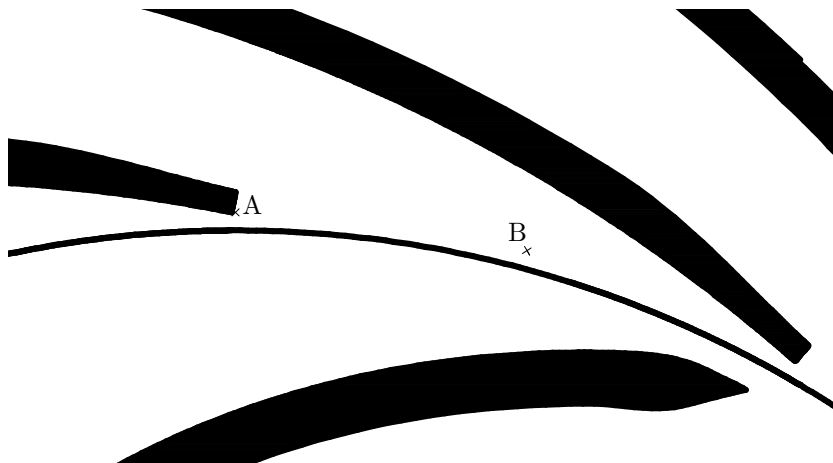


Figure 5.13. The location of the points A and B, both with a radial coordinate of 0.220 m.

In these points the pressure coefficient C_p is calculated by

$$C_p = 2 \frac{p - p_0}{\rho U_2^2}, \quad (5.3)$$

with p_0 the static pressure at the inlet of the axial pipe of the experimental setup. The static pressure difference between the inflow surface of the numerical domain and p_0 equals 328 Pa by assuming constant total pressure. For three flow rates C_p is shown in Fig. 5.14 for point A and in Fig. 5.15 for point B. The pressure level in point A, close to the leading edge of the stator vane is larger than in point B. The pressure fluctuation has a minimum at $Q = Q_{BEP}$ in point A, as expected. However in point B the pressure fluctuation is smaller for a smaller flow rate.

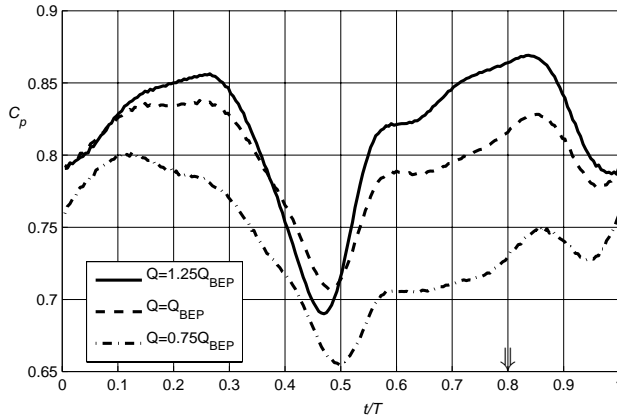


Figure 5.14. The normalized pressure in point A as a function of the dimensionless time, with T the time between two consecutive rotor blade passings. The \Downarrow marks the time at which the tip of the rotor blade passes point A.

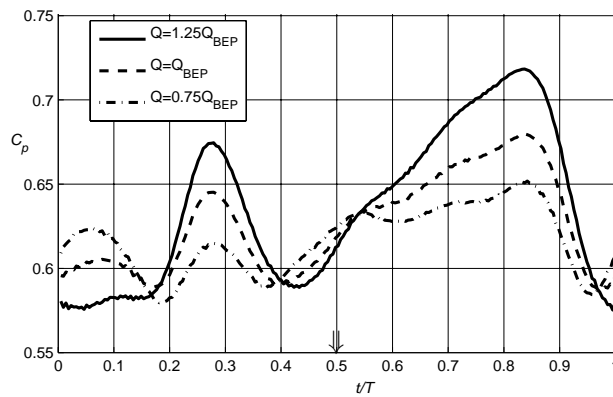


Figure 5.15. The normalized pressure in point B as a function of the dimensionless time, with T the time between two consecutive rotor blade passings. The \Downarrow marks the time at which the tip of the rotor blade passes point B.

5.4 Comparison

Results of calculations using DeFT and Fluent are given in Fig. 5.16. Radial velocity w_r , relative tangential velocity w_θ and static pressure coefficient C_p , time-averaged in the rotating frame of reference, are compared with measured values. The trailing edge of the rotor blade coincides with the zero position along the horizontal axis. As seen from the rotating frame of reference, the stator blades move from left to right. The Fluent calculation was done with 5 different types of pressure interpolation, all giving the same result. The QUICK scheme, used in Fluent for higher order accuracy, results in a solution that becomes unstable after one revolution. For reasons of comparison, the order of the discretization was therefore reduced to first-order upwind, for both Fluent and DeFT. The results obtained with DeFT and Fluent are very similar and the calculation times are approximately equal as well. For 5 rotor revolutions DeFT needed 20 hours, with two pressure-correction iterations per time-step, while Fluent needed 21 hours. The results in Fig. 5.16 are obtained by rotating another stator vane passage, while the pressure and velocity are averaged over time. The flow has become periodic in time, because the results do not change when the calculation is continued further. Both simulations were performed with one core of a dual core Intel Xeon 5130 2GHz processor. The computer memory used by DeFT and Fluent is equal to 181 and 153 MB respectively, both using double precision.

In Fig. 5.17 the curves for the central discretization in DeFT are compared with the experimental results and CFD results from [18] and [26]. In [18] the 3D thin-layer RANS equations are solved, using the artificial compressibility method with dual time stepping combined with a PWI method. The grid consists of 874,000 nodal points and the tip clearance is modeled using one computational cell. The pressure distribution is not given in [18]. In [26] the 2D RANS equations are solved using CFX4.1 using a very coarse grid of 21,048 cells. There is qualitative agreement between measurements and calculations, with a pronounced difference in values of minima and maxima, and phase. The calculated radial velocity is too low for both [18] and [26]. The viscous blockage effect of the boundary layers at the hub and the casing is not modeled in [26] because the flow domain is two-dimensional. In [18] these boundary layers were modeled, but probably with a too low grid resolution. The tangential velocity of [26] is too large, which gives an increased head of the pump. This is consistent with a flow rate that is too small. The pressure phase shift between the numerical and experimental results is larger than the phase shift between the numerical results. In [26] and [6] it is argued that the pressure minimum should be positioned close to the trailing edge of the rotor, due to high relative velocities. A time lag in the pressure measurement therefore seems to be a plausible explanation for the phase shift.

The time-averaged quantities are calculated at a radius of 214 mm. They are recalculated at radii of 213 and 215 mm to see their sensitivity with respect to radius. The results are shown in Fig. 5.18. The sensitivity is strongest close to the blade, where the maximum and minimum values are attained. In the middle of the rotor channel the sensitivity is much smaller.

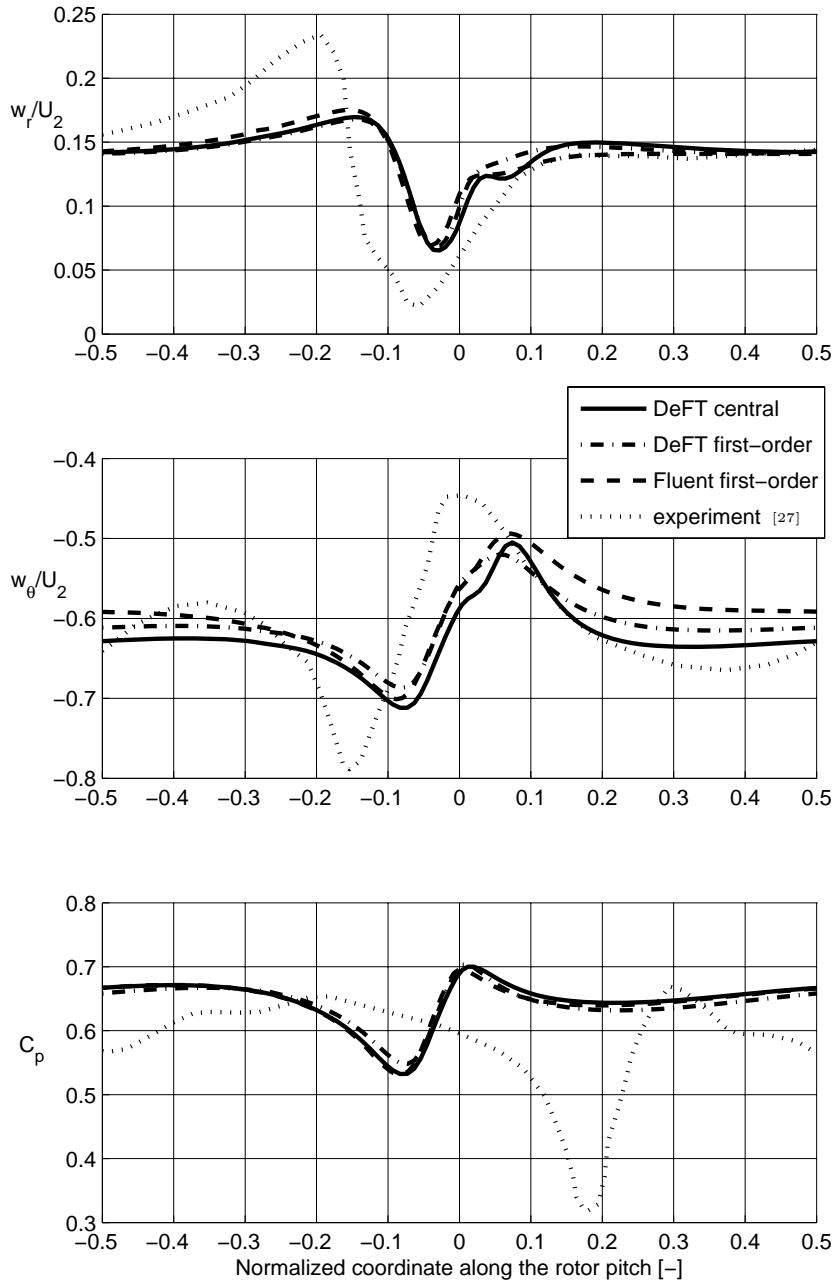


Figure 5.16. Time-averaged radial velocity, relative tangential velocity and pressure coefficient in a rotor channel.

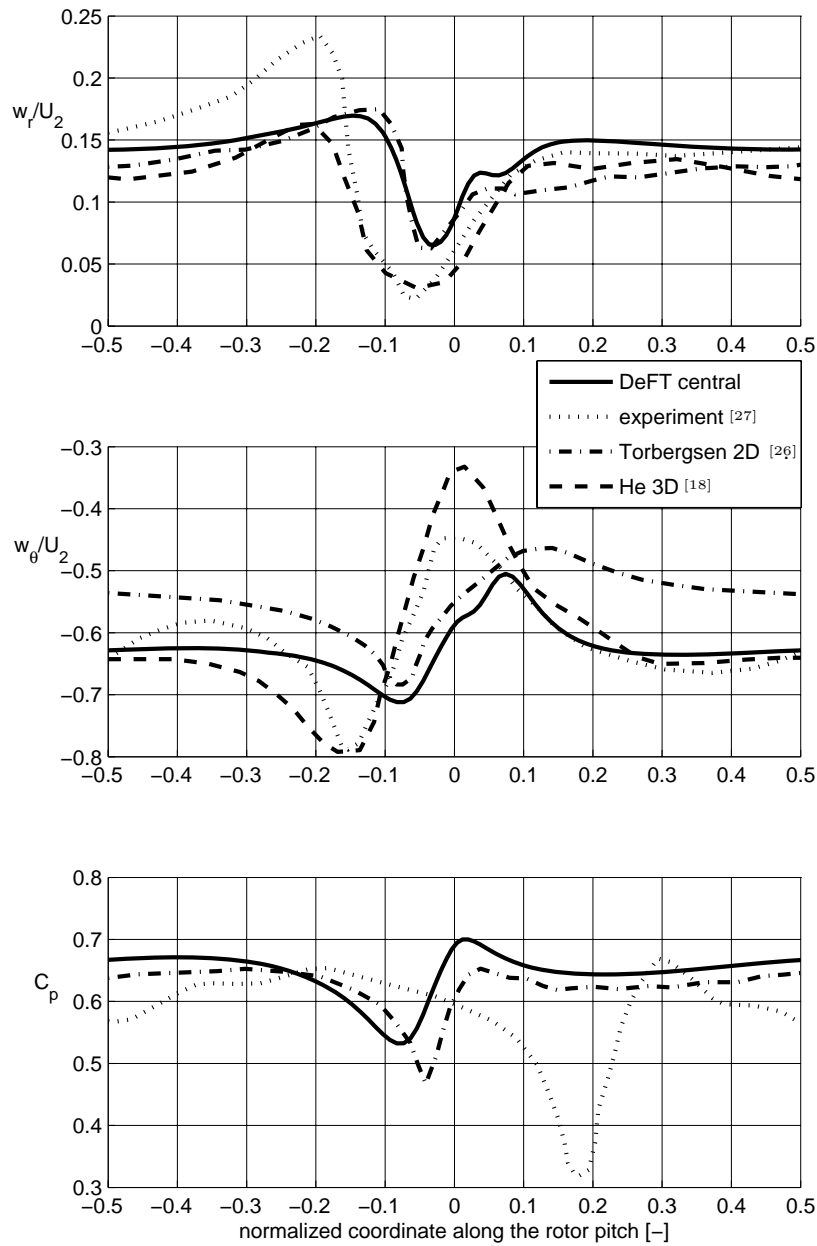


Figure 5.17. Time-averaged radial velocity, relative tangential velocity and pressure coefficient in a rotor channel.

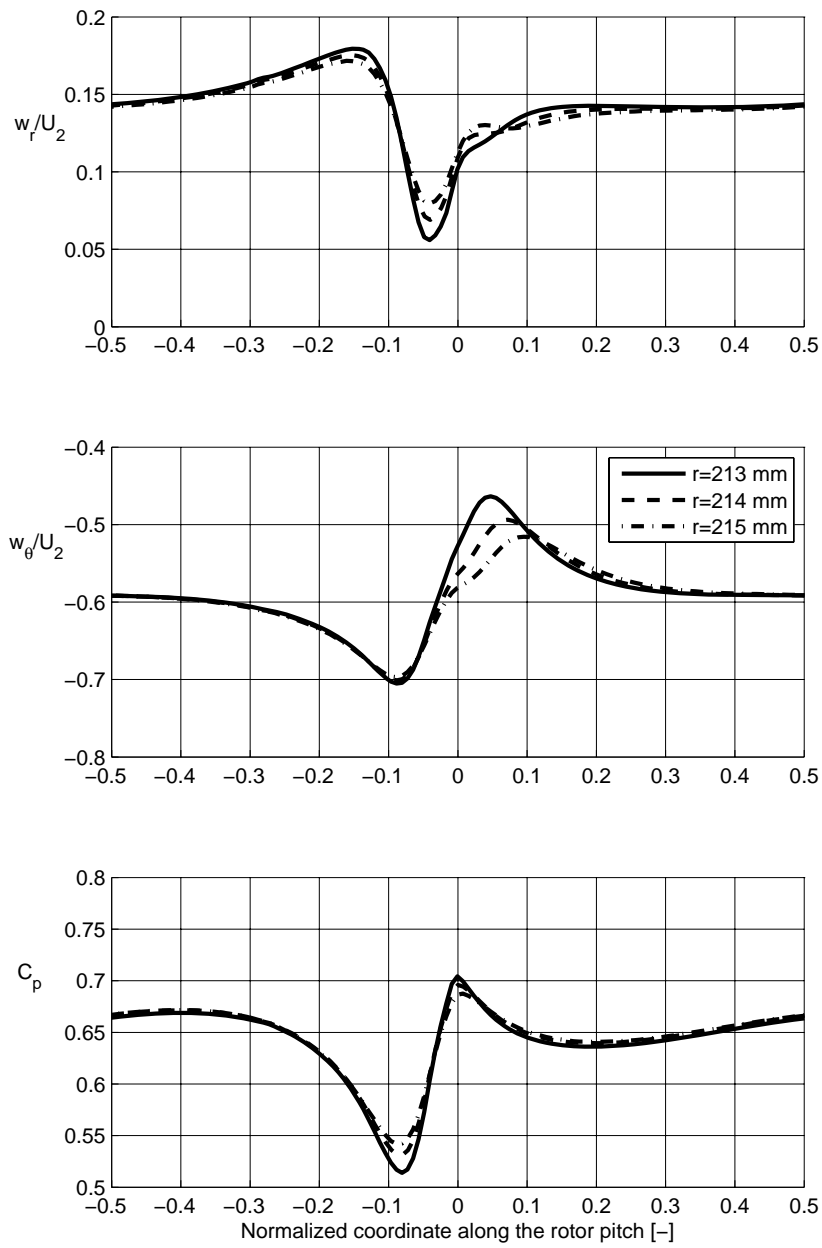


Figure 5.18. Time-averaged radial velocity, relative tangential velocity and pressure coefficient in a rotor channel at 3 different radii.

5.5 Conclusions

When compared with the experimental results, the calculations of [18] are obviously better than the other CFD results. Apparently 3D flow effects are significant. The staggered method of DeFT and the collocated method of Fluent perform equally well in terms of calculation time to obtain equal accuracy. Note that Fluent uses a multi-grid method, which is known to reduce computing time considerably. The large difference in performance between both methods for the simulation of the unsteady channel flow in section 3.1, is not observed for the flow simulation of this pump. Since the current implementation of DeFT can only handle one type of boundary condition at each block face, the total number of blocks in the grid is unnecessarily large, deteriorating the convergence behavior of DeFT. With 203 words per node, computer memory usage for DeFT is large but not significantly larger than for Fluent.

Chapter 6

Conclusions and discussion

6.1 Conclusions

Turbines and pumps are examples of hydraulic turbomachines if the working fluid is incompressible. To optimize these machines it is necessary to analyze the time-dependent flow in detail. Flow simulations using Computational Fluid Dynamics (CFD) can achieve this. The software solves the discretized partial differential equations for mass and momentum conservation on a grid that contains the entire flow domain. Two basic discretization schemes can be distinguished: collocated and staggered. When a collocated scheme is used, the solution suffers from odd-even decoupling. In practice this is suppressed with artificial measures which either decrease the accuracy of the simulation or increase the calculation time for an unsteady incompressible flow. Using a staggered scheme, accurate discretization is more difficult, but odd-even decoupling is avoided. In this thesis the development of the existing staggered CFD package DeFT is continued to make it suitable for the simulation of the flow through a turbomachine.

6.1.1 DeFT

DeFT is a numerical solver that uses boundary-fitted block-structured grids. The time-dependent incompressible Reynolds-Averaged Navier-Stokes equations are discretized on the grid and solved with the $k-\epsilon$ turbulence model. Calculations can be done in the rotating frame of reference. The Coriolis and centrifugal forces that arise in the governing equations in this case, can be modeled by source terms. An alternative method to account for the apparent Coriolis and centrifugal forces, using a conservative formulation, was added to the program. The system of equations is solved with the pressure-correction method. Both the classical and the WesBeek staggered discretization can be used. The WesBeek discretization is suited for non-uniform grids, while the classical discretization is not.

An interpolation procedure for the grid and the primitive variables is implemented to handle non-matching grids for more flexibility in grid generation. The sliding interface between the rotating grid in the impeller and the stationary grid is developed as

well. Usually, the pressure equation is solved for the pressure difference between two time-steps. However, at the sliding interface the pressure difference is discontinuous during the first iteration of the loop over the equations, leading to slow convergence. Therefore, the pressure equation is adapted to solve for the pressure at the new time-level directly. In this way the iteration process should converge faster. All simulations and adaptations of DeFT are done in 2D.

6.1.2 Verification

The performance of DeFT and the collocated CFD program Fluent are compared for an unsteady laminar channel flow. On a grid of 10 blocks and 100,000 grid cells the error in the pressure at the channel inlet is monitored. For equal accuracy, the calculation time needed by Fluent is more than 3 times larger than the calculation time needed by DeFT.

The accuracy of the classical and the WesBeek staggered discretizations in DeFT and the collocated discretization of Fluent is compared for a flow through a vaneless diffuser. The difference between the numerical and the theoretical values of the pressure difference across the diffuser is used to represent the numerical error. Three different grids are used: an equidistant grid, a smooth non-uniform grid with an increasing cell density towards the diffuser inlet, and a rough grid. On the rough grid the collocated and the WesBeek discretizations give good results, while the error using the classical staggered discretization is large, as expected. The same is true for the smooth non-uniform grid. On the equidistant grid, the error using the collocated grid is much larger than the error using both staggered discretizations. This can be the result of an artificial odd-even coupling method which is insufficient.

A turbulent jet flow is simulated in the stationary and the rotating frame of reference. Because the resulting pressure distributions in both frames are approximately equal, it is concluded that the implementation of the turbulence model is correct, also in the rotating frame of reference.

The source term and the conservative formulations of the Coriolis and the centrifugal forces are compared for an axi-symmetric laminar flow. The error and the grid convergence for the pressure and the velocity components are determined using the analytical solution of the flow. Because the errors for both methods are approximately equal, there is no preference for the conservative or the source term formulation.

The flow around a cylinder is used to verify the correct implementation of the sliding interface. The flow is simulated in two ways. The first simulation is with all blocks in the stationary frame of reference. The second simulation is the same, except for the inner region which is calculated in the rotating frame of reference. The pressure distributions resulting from both simulations are close to identical if the pressure equation is directly solved for the pressure at the new time-step while using one pressure-correction iteration. When the pressure equation is solved for the pressure difference between two time-steps, a discontinuity in the pressure across the sliding interface arises when only a few pressure-correction iterations are used. This confirms the anticipated preference to solve the pressure equation directly for the pressure at the new time-level when a sliding interface is used.

6.1.3 Validation

An axial pump is modeled by a cascade of blades. For the inlet angle equal to 70° the turbulent flow through several pumps, each with a different stagger angle, is simulated with DeFT and Fluent. The calculated blade surface pressure is compared with results from experiments and CFD, both available in literature. For most cases there is good agreement between the results. Lift and drag forces are calculated as well. The agreement between results from CFD and experiments is good for an angle of attack between 4° and 10° .

To determine the Best Efficiency Point (BEP) for each pump, additional simulations were done with varying inlet angle. It turned out that for all pumps the BEP corresponds with an angle of attack equal to 6° .

The force on the blade is also decomposed into axial and tangential components, which are a measure for the head and the torque of the pump. These forces are plotted as a function of the deviation of the flow rate from BEP condition. For flow rates from $0.8Q_{bep}$ to $1.4Q_{bep}$ the errors are only a few percent. That is why it is expected that CFD can be used to model the flow through a turbomachine when it operates in this range of flow rates. At lower flow rates the errors are larger, probably due to flow separation.

6.1.4 Unsteady flow in a pump

Using the staggered WesBeek discretization in DeFT, the turbulent flow through a centrifugal pump with a vaned diffuser can be simulated on a rough grid in 2D. The flow in this pump is simulated with a collocated discretization in Fluent as well. For several flow rates the head and the efficiency of the pump are determined. The flow at the best efficiency point has the most smooth approach of the stator vanes. The calculated time-averaged pressure and velocity along the pitch of a rotor channel by DeFT and Fluent show good correspondence. The agreement with values from experiments and other CFD calculations obtained from literature is more qualitative. On a grid of over 110,00 cells, the calculation time needed by DeFT and Fluent is approximately equal, despite the use of a large number of 126 blocks in DeFT and its lack of a convergence enhancing multi-grid method which is used by Fluent.

6.2 Discussion

In this thesis it is shown that a staggered grid method, based on the WesBeek discretization, is suited for calculating the time-dependent flow through a centrifugal pump. The method has advantages over the collocated method, in terms of speed and accuracy. Although this advantage was not shown clearly by the pump simulations of chapter 5, one has to remember that the staggered method was hindered by the large number of grid blocks, slowing down its convergence speed considerably. Moreover, the current version of DeFT lacks the multi-grid method employed by Fluent. The performance of DeFT will enhance greatly, should it be possible to remove the above mentioned drawbacks. To increase the convergence speed, the stability and

the flexibility of DeFT, it is recommended to address the following issues in a future study:

- To increase the convergence rate of DeFT for simulations with a large number of cells, the implementation of a global multi-grid procedure is recommended.
- Reducing the number of blocks in a grid increases the convergence rate as well. Therefore it is recommended to implement the possibility of handling multiple types of boundary condition per block face.
- The implementation of the convergence check of the total system of equations is needed to decide if another iteration loop over these equations is necessary.
- In order to increase the stability of calculations while using a higher order discretization scheme for the convection terms, a higher order upwind scheme should be implemented that is more stable than the present central scheme, but accurate on rough grids as well.
- Often the result of a steady flow calculation is used as initial solution for a transient simulation. Therefore it is recommended to implement a solver for the steady flow equations in DeFT.
- The current method for information exchange between non-matching blocks uses interpolation of the variables in the direction parallel to the multi-block boundary only. The disadvantage of this method is that it poses restrictions on the block-topology. This often leads to extra blocks. To be more flexible with grid generation and to reduce the total number of blocks needed, the implementation of a method that determines the virtual coordinates using extrapolation of the real grid of the same block is recommended. However, the disadvantage of this method is the need for interpolation in the direction normal to the multi-block boundary as well.
- In [32] the current staggered discretization is developed in 3D. Therefore, and to increase the applicability of DeFT, the previous recommendations and the sliding interface should be extended to 3D.

Bibliography

- [1] *User manual of the DeFT incompressible flow solver.*
- [2] Beddhu, M., L. Taylor, and D. Whitfield: 1996, ‘Strong conservative form of the incompressible Navier-Stokes equations in a rotating frame with a solution procedure’. *Journal of computational physics* **128**, 427–437.
- [3] Brakkee, E.: 1996, ‘Domain decomposition for the incompressible Navier-Stokes equations’. Ph.D. thesis, Delft University of Technology, The Netherlands.
- [4] Bulten, N.: 2006, ‘Numerical analysis of a waterjet propulsion system’. Ph.D. thesis, Division of Mechanical Engineering, Eindhoven University of Technology, The Netherlands.
- [5] Chorin, A.: 1967, ‘A numerical method for solving incompressible viscous flow problems’. *J. Comp. Phys.* **2**, 12–26.
- [6] Chu, S., R. Dong, and J. Katz: 1995, ‘Relationship between unsteady flow, pressure fluctuations and noise in a centrifugal pump - Part B: Effects of blade-tongue interactions’. *J. of fluids engineering* **117**, 30–35.
- [7] Combes, J., P. Bert, and J. Kueny: 1997, ‘Numerical investigation of the rotor-stator interaction in a centrifugal pump using a finite element method’. In: *ASME Fluids Engineering Division Summer Meeting.*
- [8] Dick, E.: 1988, ‘A flux-vector splitting method for steady Navier-Stokes equations’. *Int. J. Num. Meth. in Fluids.* **8**, 317–326.
- [9] Dick, E.: 1989, ‘A multigrid method for steady incompressible Navier-Stokes equations based on partial flux splitting’. *Int. J. Num. Meth. in Fluids.* **9**, 113–120.
- [10] Dick, E. and J. Linden: 1992, ‘A multigrid method for steady incompressible Navier-Stokes equations based on flux difference splitting’. *Int. J. Num. Meth. in Fluids.* **14**, 1311–1323.
- [11] Ellison, J., C. Hall, and T. Porsching: 1987, ‘An unconditionally stable convergent finite difference method for Navier-Stokes problems on curved domains’. *SIAM J. Num. Anal.* **24**, 1233–1248.

-
- [12] Emery, J., L. Herrig, J. Erwin, and A. Felix: 1958, 'Systematic two-dimensional cascade tests of NACA 65-series compressor blades at low speeds'. NACA report 1368, Langley Aeronautical Laboratory, Langley Field.
- [13] Fletcher, C.: 1988, *Computational techniques for fluid dynamics, Vols. 1 and 2*. Berlin: Springer-Verlag.
- [14] Frank, J.: 2000, 'Efficient algorithms for the numerical solution of differential equations'. Ph.D. thesis, Delft University of Technology, The Netherlands.
- [15] Fuchs, L. and H. Zhao: 1984, 'Solution of three-dimensional viscous incompressible flows by a multigrid method'. *Int. J. Num. Meth. in Fluids* **4**, 539–555.
- [16] Gu, C.: 1991, 'Computations of flows with large body forces'. *Num. Meth. Lam. Turb. Flow* **7 part 2**, 1568–1578.
- [17] Harlow, F. and J. Welch: 1965, 'Numerical calculation of timedependent viscous flow of fluid with a free surface'. *Phys. Fluids* **8**, 2182–2189.
- [18] He, L. and K. Sato: 2001, 'Numerical solution of incompressible unsteady flows in turbomachinery'. *J. of fluids engineering* **123**, 680–685.
- [19] Hirsch, C.: 1990, *Numerical computation of internal and external flows, Vols. 1 and 2*. Chichester: John Wiley.
- [20] Liew, R.: 2008, *Numerieke simulatie van stroming door een cascade opstelling*. Internship report (in Dutch), Division of Mechanical Engineering, Eindhoven University of Technology, The Netherlands.
- [21] Miller, T. and F. Schmidt: 1988, 'Use of a pressure-weighted interpolation method for the solution of the incompressible Navier-Stokes equations on a non-staggered grid system'. *Num. Heat Transfer* **14**, 213–233.
- [22] Patankar, S.: 1980, *Numerical heat transfer and fluid flow*. Washington–New York–London: Hemisphere publishing corporation.
- [23] Peyret, R. and T. Taylor: 1983, *Computational methods for fluid flow*. Berlin: Springer.
- [24] Rhie, C. and W. Chow: 1983, 'Numerical study of the turbulent flow past an airfoil with trailing edge separation'. *AIAA J.* **21**, 1525–1532.
- [25] Tamamidis, P., G. Zhang, and D. Assanis: 1996, 'Comparison of pressure-based and artificial compressibility methods for solving 3D steady incompressible flows'. *Num. J. Comp. Phys.* **124**, 1–13.
- [26] Torbergsen, E. and M. White: 1997, 'Transient simulation of impeller/diffuser interactions'. In: *ASME Fluids Engineering Division Summer Meeting*.
- [27] Ubaldi, M., P. Zunino, G. Barigozzi, and A. Cattanei: 1996, 'An experimental investigation of stator induced unsteadiness on centrifugal impeller outflow'. *J. Turbomachinery* **118**, 41–54.

-
- [28] van Beek, P., R. van Nooyen, and P. Wesseling: 1995, 'Accurate discretization on non-uniform curvilinear staggered grids'. *Journal of computational physics* **117**, 364–367.
- [29] van der Vorst, H. and C. Vuik: 1994, 'GMRESR: a family of nested GMRES methods'. *Num. Lin. Alg. Appl.* **1**, 369–386.
- [30] Vuik, C.: 1993, 'Solution of the discretized incompressible Navier-Stokes equations with the GMRES method'. *Int. J. Num. Meth. in Fluids* **16**, 507–523.
- [31] Wesseling, P.: 2000, *Principles of computational fluid dynamics*. Berlin–Heidelberg–New York: Springer –Verlag.
- [32] Wesseling, P., A. Segal, and C. Kassels: 1999, 'Computing flows on general three-dimensional nonsmooth staggered grids'. *J. Comp. Phys.* **149**, 333–362.
- [33] Wesseling, P., A. Segal, C. Kassels, and H. Bijl: 1998, 'Computing flows on general two-dimensional staggered grids'. *J. Eng. Math.* **34**, 21–44.
- [34] Wilcox, D.: 1993, *Turbulence modeling for CFD*. La Canada, California: DCW Industries, Inc.
- [35] Zijlema, M.: 1996, 'Computational modeling of turbulent flow in general domains'. Ph.D. thesis, Delft University of Technology, The Netherlands.

Appendix A

Blade surface coordinates

suction side		pressure side	
x	y	x	y
1.00000	0.00000	1.00000	0.00000
0.95029	0.00937	0.94971	0.00327
0.90057	0.01842	0.89943	0.00226
0.85076	0.02729	0.84924	-0.00037
0.80088	0.03577	0.79912	-0.00393
0.75090	0.04372	0.74910	-0.00792
0.70085	0.05099	0.69915	-0.01211
0.65073	0.05741	0.64927	-0.01621
0.60053	0.06288	0.59947	-0.02004
0.55029	0.06720	0.54971	-0.02340
0.50000	0.07018	0.50000	-0.02606
0.44968	0.07153	0.45032	-0.02773
0.39936	0.07138	0.40064	-0.02854
0.34903	0.06983	0.35097	-0.02863
0.29872	0.06702	0.30128	-0.02814
0.24843	0.06290	0.25157	-0.02710
0.19817	0.05731	0.20183	-0.02547
0.14798	0.05006	0.15202	-0.02314
0.09788	0.04067	0.10212	-0.01999
0.07289	0.03487	0.07711	-0.01791
0.04797	0.02800	0.05203	-0.01536
0.02318	0.01935	0.02682	-0.01191
0.01089	0.01372	0.01411	-0.00944
0.00607	0.01061	0.00893	-0.00781
0.00372	0.00861	0.00628	-0.00661
0.00000	0.00000	0.00000	0.00000

Table A.1. The cartesian Naca 65-410 blade coordinates for a chord length of 1. The x and y direction are parallel and perpendicular to the blade chord respectively.

Dankwoord

Dit proefschrift is geschreven naar aanleiding van het onderzoek dat ik gedaan heb in de vakgroep procestechnologie van de faculteit werktuigbouwkunde aan de technische universiteit Eindhoven. Ik heb het daar erg naar mijn zin gehad. Het onderwerp van het onderzoek past precies bij mij. Daarnaast heb ik de samenwerking en de omgang met begeleiders en collega's als heel prettig ervaren. Een aantal mensen hebben hieraan bijgedragen.

Mijn promotor Bert Brouwers is voorzitter van de vakgroep. Zijn enthousiasme voor de aanpak van fundamentele problemen in de stromingsleer is bijzonder. Ook het initiatief om met zijn AIO's te gaan eten wordt altijd zeer gewaardeerd.

Naast initiator van het onderzoek en co-promotor, is Bart van Esch toch vooral mijn dagelijks begeleider geweest. Het met een open houding bespreken van het onderzoek was niet alleen prettig, maar is ook de kwaliteit van het onderzoek ten goede gekomen. Daarnaast was zijn numerieke achtergrond en zijn specialisme op het gebied van pompen erg waardevol. Bovendien heeft zijn vermogen om duidelijk, en met een logische opbouw te schrijven, dit proefschrift een stuk leesbaarder gemaakt.

Veel van deze uitspraken gelden ook voor Hans Kuerten, mijn tweede co-promotor en dagelijks begeleider. Zijn adviezen op vooral numeriek gebied zijn belangrijk geweest in dit project. Daarnaast kwam hij vaak langs om tijdens het drinken van een kop thee even over het onderzoek of andere zaken bij te praten; heel gezellig.

Het onderzoek is gefinancierd door technologiestichting STW. Naast prof.dr.ir. P. Wesseling zaten de volgende bedrijven in de gebruikerscommissie van STW: Bosman Watermanagement, Beli Technics, BuNova Development, Duijvelaar Pompen, Nijhuis Pompen en Wartsila Propulsion Netherlands. Gedurende het project is de gebruikerscommissie een aantal keren bijeen geweest om de voortgang van het onderzoek te bespreken en keuzes te maken betreffende nieuwe stappen. De promotiecommissie bestaat uit de promotor, de co-promotoren, prof.dr.-ing. F.K. Benra, prof.dr.ir. P. Wesseling, prof.dr. E. Dick, en prof.dr.ir. A.A. van Steenhoven.

Joost de Hoogh was twee jaar mijn kamergenoot. We hebben vele discussies met een hoop humor gehad over sport, briljante software en andere relevante onderwerpen. Bovendien heeft hij me op weg geholpen met Linux, Fortran en DeFT. Ook Jan Hasker heeft regelmatig mijn computerproblemen opgelost. Bert Vreman heeft significant bijgedragen aan het onderzoek bij het aan de praat krijgen van DeFT voor de simulatie van de stroming door de centrifugaalpomp. Raoul Liew heeft uitvoerig numeriek onderzoek gedaan met Fluent naar de stroming door de axiaalpompe. Jeroen

van Lipzig is gestart met de simulatie in Fluent van de stroming door de centrifugaalpompe.

Met mijn collega-AIO's heb ik vooral vaak geluncht. Dat was altijd een welkome en gezellige onderbreking van de werkdag. Ook de bereidheid om elkaar te helpen met praktische zaken en de tijd voor persoonlijke dingen, waardeer ik zeer.

Ik ben blij met het optreden van mijn goede vriend Jan-Hendrik van der Goot en mijn broer Cor de Kleine als paranimf. De interesse voor mijn onderzoek en mij als persoon en de soms bijna onvoorwaardelijke steun van mijn vrienden, familie en in het bijzonder mijn ouders, broers en zus zijn hartverwarmend. Bovenal is het prachtig om mijn leven te delen met mijn vrouw Marie-Elise.

Allemaal hartelijk dank voor jullie hulp en betrokkenheid. Gods rijke zegen, die ik zo vaak ervaar, ook in mijn werk, wens ik jullie toe.

David de Kleine

Curriculum vitae

David de Kleine was born in Nijemirdum, on February 8, 1977. From 1989 to 1995 he followed his pre-university education (VWO) at the Bogerman College in Sneek. In 1995 he started to study mechanical engineering at the University of Twente. He specialized in mechanics and fluid dynamics. At the physics department of Moscow State University he did an internship of three months, studying the shear-thickening effect in associating polyelectrolyte solutions. Finally he graduated on the theory of statistical energy analysis for structures in 2003.

Later that year, he started working as a Ph.D. student on mode coupling phenomena in articulated structures at the department of architecture, building and planning at Eindhoven University of Technology. Part of this work is published in: *Thin-Walled Structures*, volume 44, 2006, p. 1240-1249.

In 2005 he switched to a new Ph.D. project at the mechanical engineering department of the same university. There he worked on the numerical simulation of unsteady flow in hydraulic turbomachines. The results of this work are described in this thesis. Parts of this work are presented at the WSEAS conference at Rhodes (Greece, 2008) and the ASME FEDSM conference in Vail, Colorado (USA, 2009).